



National Library  
of Canada

Bibliothèque nationale  
du Canada

Canadian Theses Service

Service des thèses canadiennes

Ottawa, Canada  
K1A 0N4

## NOTICE

The quality of this microform is heavily dependent upon the quality of the original thesis submitted for microfilming. Every effort has been made to ensure the highest quality of reproduction possible.

If pages are missing, contact the university which granted the degree.

Some pages may have indistinct print especially if the original pages were typed with a poor typewriter ribbon or if the university sent us an inferior photocopy.

Reproduction in full or in part of this microform is governed by the Canadian Copyright Act, R.S.C. 1970, c. C-30, and subsequent amendments.

## AVIS

La qualité de cette microforme dépend grandement de la qualité de la thèse soumise au microfilmage. Nous avons tout fait pour assurer une qualité supérieure de reproduction.

S'il manque des pages, veuillez communiquer avec l'université qui a conféré le grade.

La qualité d'impression de certaines pages peut laisser à désirer, surtout si les pages originales ont été dactylographiées à l'aide d'un ruban usé ou si l'université nous a fait parvenir une photocopie de qualité inférieure.

La reproduction, même partielle, de cette microforme est soumise à la Loi canadienne sur le droit d'auteur, SRC 1970, c. C-30, et ses amendements subséquents.



National Library  
of Canada

Bibliothèque nationale  
du Canada

Canadian Theses Service    Service des thèses canadiennes

Ottawa, Canada  
K1A 0N4

The author has granted an irrevocable non-exclusive licence allowing the National Library of Canada to reproduce, loan, distribute or sell copies of his/her thesis by any means and in any form or format, making this thesis available to interested persons.

The author retains ownership of the copyright in his/her thesis. Neither the thesis nor substantial extracts from it may be printed or otherwise reproduced without his/her permission.

L'auteur a accordé une licence irrévocable et non exclusive permettant à la Bibliothèque nationale du Canada de reproduire, prêter, distribuer ou vendre des copies de sa thèse de quelque manière et sous quelque forme que ce soit pour mettre des exemplaires de cette thèse à la disposition des personnes intéressées.

L'auteur conserve la propriété du droit d'auteur qui protège sa thèse. Ni la thèse ni des extraits substantiels de celle-ci ne doivent être imprimés ou autrement reproduits sans son autorisation.

ISBN 0-315-55439-8

Canada

THE UNIVERSITY OF ALBERTA

ZERO DEGREE RADIATIVE CAPTURE OF NEUTRONS BY PROTONS

BY



GEOFFREY WILLIAM ROY EDWARDS

A THESIS

SUBMITTED TO THE FACULTY OF GRADUATE STUDIES AND RESEARCH IN

PARTIAL FULFILMENT OF THE REQUIREMENTS FOR THE DEGREE OF

DOCTOR OF PHILOSOPHY

IN

NUCLEAR PHYSICS

DEPARTMENT OF PHYSICS

EDMONTON, ALBERTA, CANADA

FALL 1989

RELEASE FORM

NAME OF AUTHOR: GEOFFREY W.R. EDWARDS

TITLE OF THESIS: ZERO DEGREE RADIATIVE CAPTURE OF NEUTRONS  
BY PROTONS

DEGREE FOR WHICH THESIS WAS PRESENTED: DOCTOR OF PHILOSOPHY

YEAR THIS DEGREE GRANTED: 1989

Permission is hereby granted to THE UNIVERSITY OF ALBERTA LIBRARY to reproduce single copies of this thesis and to lend or sell such copies for private, scholarly or scientific research purposes only.

The author reserves other publication rights, and neither the thesis nor extensive extracts from it may be printed or otherwise reproduced without the author's written permission.

(Signed) *GWR Edwards*

PERMANENT ADDRESS:

67 RUTHERFORD

DEEP RIVER, ONTARIO, CANADA

K0J 1P0

**THE UNIVERSITY OF ALBERTA**  
**FACULTY OF GRADUATE STUDIES AND RESEARCH**

The undersigned certify that they have read, and recommend to the Faculty of Graduate Studies and Research, for acceptance, a thesis entitled "ZERO DEGREE RADIATIVE CAPTURE OF NEUTRONS BY PROTONS" submitted by GEOFFREY W.R. EDWARDS in partial fulfillment of the requirements for the degree of Doctor of Philosophy in Nuclear Physics.

John Cameron  
SUPERVISOR

D. A. G. G. G.

L. H. Greeniaus

Ronald P. W. L.

B. A. Campbell

Jan. An. Kaji

EXTERNAL EXAMINER

Date: Feb 27/89

## ABSTRACT

Differential cross-section measurements for the radiative capture reaction  $p(n,d)\gamma$  at  $0-3^\circ$  lab angle and neutron energies of 360, 410 and 460 MeV ( photon lab energies of 182.5, 207.7 and 232.5 MeV for the inverse reaction) have been made using the TRIUMF Medium Resolution Spectrometer. These data complement recently measured photo-disintegration differential cross-sections in this energy range and are the first time that the capture cross-section has been investigated above the pion production energy threshold. A comparison is made between the data and three current predictions for the radiative capture cross-section, and it is noted that there is an approximate agreement.

## ACKNOWLEDGEMENTS

This experiment reported in this dissertation was done at the TRIUMF cyclotron, in Vancouver, by a collaboration involving TRIUMF, University of Alberta and University of Manitoba researchers.

I would like to acknowledge the companionship and invaluable help which I have been given as a graduate student at the University of Alberta and as a member of the collaboration which performed this experiment. Without diminishing the importance of my many friends here with who have helped me with informative discussions and technical advice, I would like to single out a few individuals for special thanks.

Dr. David Hutcheon has been instrumental not only to the success of the project, but also to my development as an experimental physicist. Dave co-ordinated all parts of the experiment and advised me on the analysis. His patience, friendship and sense of humour were very much appreciated.

Dr. Gordon Greeniaus helped enormously by always being available to talk about analysis problems, and by proof-reading the text of this dissertation.

Over the space of several years, the many discussions I have had with Dr. Faqir Khanna about the theoretical aspects of deuteron photo-disintegration theory have been a great pleasure as well as instructional.

Dr. Peter Green was extremely helpful over the years by answering programming questions and providing access to computer facilities above and beyond

the call of duty. He'd better be careful, or he'll get a reputation for being nice!

Herb Coombes worked with me to design, build and install the system of thin scintillators inside the  $\text{LH}_2$  target. This gave me one of the few chances I had to actually get some practical shop experience and will remain a fond memory of some of the time spent working on this experiment.

Dr. Ieks van Heerden, who was working on the analysis of a similar experiment provided invaluable feedback and many new ideas which I was able to apply to the analysis of my own experiment.

I would also like to thank the many graduate students with whom I have debated a physics concept, drunk a beer or bounced a basketball. Gerhard Lotz, Richard Tkachuk and Jon Johansson have all been heroic in one or more of these categories.

Finally, I would like to extend my sincere thanks to my supervisor, Dr. John Cameron for his advice and support throughout this project.



## TABLE OF CONTENTS

| <u>CHAPTER</u> |   | <u>PAGE</u> |
|----------------|---|-------------|
| I              | THE DEUTERON IN NUCLEAR PHYSICS                 | 1           |
| II             | REVIEW OF THEORETICAL WORK                      | 11          |
| II.1           | PROBLEMS WITH THE CLASSICAL APPROACH            | 11          |
| II.1.1         | The deuteron D state                            | 11          |
| II.1.2         | Meson exchange currents                         | 12          |
| II.1.3         | Relativistic kinematic corrections              | 18          |
| II.1.4         | Nucleon isobars                                 | 22          |
| II.2           | SUMMARY   | 25          |
| III            | DESCRIPTION OF THE EXPERIMENT                   | 26          |
| III.1          | THE TRIUMF CYCLOTRON                            | 26          |
| III.1.1        | The Medium Resolution Spectrometer              | 28          |
| III.1.2        | The CHARGEEX facility                           | 30          |
| III.2          | PROCEDURAL DETAILS                              | 33          |
| III.2.1        | Nuclear reactions in the LH <sub>2</sub> target | 33          |
| III.2.2        | Background reactions                            | 35          |
| III.2.3        | Event definition                                | 49          |
| III.2.4        | Experimental runs                               | 45          |
| IV             | DATA ANALYSIS (1)                               | 46          |
| IV.1           | PRELIMINARY REMARKS                             | 46          |
| IV.2           | INITIAL EVENT SELECTION                         | 48          |
| IV.3           | SPECTROMETER CHARACTERISTICS                    | 56          |

|                          |  |                    |
|--------------------------|--|--------------------|
| IV.4                     | FINAL EVENT SELECTION  | 61                 |
| IV.4.1                   | MRS acceptance restriction   | 61                 |
| IV.4.2                   | Restriction of MRS angles in the bend plane                        | 62                 |
| IV.4.3                   | MRS track reconstruction   | 62                 |
| IV.4.4                   | Restriction to particles created within the LH <sub>2</sub> target | 64                 |
| V                        | DATA ANALYSIS (2)  | 66                 |
| V.1                      | FITTING THE REACTION PEAKS (THEORY)                                | 66                 |
| V.2                      | BACKGROUNDS UNCONNECTED TO THE NEUTRON TAIL                        | 76                 |
| V.3                      | FITTING THE REACTION PEAKS (PRACTICE)                              | 78                 |
| V.3.1                    | Results at 460 MeV   | 81                 |
| V.3.2                    | Results at 410 MeV   | 89                 |
| V.3.3                    | Results at 360 MeV   | 90                 |
| V.4                      | SUMMARY AND DISCUSSION OF SYSTEMATIC ERRORS                        | 96                 |
| VI                       | SUMMARY AND CONCLUSIONS  | 100                |
| VI.1                     | MODELS OF $d(\gamma,p)n$ ABOVE THE $\pi^0$ PRODUCTION<br>THRESHOLD | 100                |
| VI.2                     | CONCLUSIONS  | 104                |
| VI.2.1                   | Theoretical considerations   | 104                |
| VI.2.2                   | Experimental considerations  | 104                |
|                          | REFERENCES   | 106                |
| <b><u>APPENDICES</u></b> |  | <b><u>PAGE</u></b> |
| A                        | IN SITU TESTING OF THE LH <sub>2</sub> SCINTILLATORS               | 109                |
| B                        | DETERMINATION OF THE MRS ACCEPTANCE                                | 114                |
| C                        | RELATIVISTIC KINEMATICS PROGRAMS                                   | 123                |
| D                        | GLOSSARY OF TERMS  | 127                |

## LIST OF TABLES

| <u>TABLE</u> |   | <u>PAGE</u> |
|--------------|---|-------------|
| 1.1          | Elementary Properties of the Deuteron   | 3           |
| 1.2          | The Predictions of the Hamada-Johnston Nucleon Nucleon Potential<br>for a Few Deuteron Properties | 5           |
| 3.1          | Experimental Dimensions   | 15          |
| 5.1          | Reaction Sums at 460 MeV  | 81          |
| 5.2          | Reaction Sums at 410 MeV  | 89          |
| 5.3          | Reaction Sums at 360 MeV  | 93          |
| A.1          | Results of In Situ Testing of the Scintillators Inside the Liquid<br>Hydrogen Target              | 110         |

## LIST OF FIGURES

| <u>FIGURE</u> |  | <u>PAGE</u> |
|---------------|--|-------------|
| 1.1           | d( $\gamma$ ,p)n Angular Distribution at $E_\gamma = 100$ MeV.     | 8           |
| 1.2           | Deuteron Photo-disintegration Below the Pion Production Threshold  | 9           |
| 2.1           | A few Feynman diagrams for photo-nuclear interactions              | 13          |
| 2.2           | 0° d( $\gamma$ ,p)n With the Inclusion of MEC                      | 15          |
| 2.3           | Effect of MEC Contributions Above the $\pi^0$ Production Threshold | 17          |
| 2.4           | 0° d( $\gamma$ ,p)n With Relativistic Corrections                  | 20          |
| 3.1           | The general plan of the TRIUMF cyclotron                           | 27          |
| 3.2           | The Medium Resolution Spectrometer.                                | 29          |
| 3.3           | The CHARGEEX facility  | 31          |
| 3.4           | Reaction Kinematics  | 34          |
| 3.5           | The Liquid Hydrogen Target   | 37          |
| 3.6           | Target Support Structure Position                                  | 38          |
| 3.7           | $^{12}\text{C}(n,d)\text{X}$ Background Suppression at 360 MeV     | 40          |
| 3.8           | MRS Trigger Logic  | 42          |
| 4.1           | The Spectrum for Particle Identification (SPID)                    | 49          |
| 4.2a          | S1 Energy Spectrum   | 51          |
| 4.2b          | VET Energy Spectrum  | 51          |
| 4.2c          | FES Energy Spectrum  | 51          |
| 4.3a          | S1 Energy Spectrum   | 52          |
| 4.3b          | VET Energy Spectrum  | 52          |
| 4.3c          | FES Energy Spectrum  | 52          |

|       |  |    |
|-------|--|----|
| 4.4a  | S1 Time Spectrum   | 53 |
| 4.4b  | VET Time Spectrum  | 53 |
| 4.4c  | FES Time Spectrum  | 53 |
| 4.5a  | S1 Time Spectrum   | 54 |
| 4.5b  | VET Time Spectrum  | 54 |
| 4.5c  | FES Time Spectrum  | 54 |
| 4.6   | The geometry of the MRS focal plane  | 57 |
| 4.7   | Edge focusing with the MRS dipole magnet                                       | 58 |
| 4.8   | MRS exit angle vs. focal plane position.                                       | 63 |
| 4.9   | The Particle Track Out of the Bend Plane                                       | 65 |
| 4.10a | The Energy Spectrum of the Thin Scintillator Downstream of the LH <sub>2</sub> | 66 |
| 4.10b | The Energy Spectrum of the Thin Scintillator Upstream of the LH <sub>2</sub>   | 66 |
| 5.1   | Neutron Spectrum from the (n,p) Reaction on Li at 450 MeV (n)                  | 69 |
| 5.2   | Neutron Line Shape Model   | 70 |
| 5.3   | p(n,p)n at 360 MeV   | 71 |
| 5.4   | Corrections to the Sum of the Raw Data in a Peak.                              | 74 |
| 5.5   | Subtraction of the Constant Background   | 77 |
| 5.6   | Momentum Spectra at 460 MeV  | 79 |
| 5.7   | An Example of the Fit to the p(n,d) $\pi^0$ Peak                               | 80 |
| 5.8   | The MRS Acceptance Function  | 83 |
| 5.9   | Angular Distribution for d( $\gamma$ ,p)n at E $_{\gamma}$ = 240 MeV           | 85 |
| 5.10  | Momentum Spectra at 410 MeV.   | 87 |
| 5.11  | Angular Distribution for d( $\gamma$ ,p)n at E $_{\gamma}$ = 200 MeV           | 91 |
| 5.12  | Momentum Spectra at 360 MeV  | 92 |
| 5.13  | Angular Distribution for d( $\gamma$ ,p)n at E $_{\gamma}$ = 180 MeV           | 95 |

|      |   |     |
|------|---|-----|
| 5.14 | Direct Measurements of $d(\gamma,p)n$ at $0^\circ$                                  | 98  |
| 5.15 | Uncertainty in the $p(n,p)n$ Cross-section  | 99  |
| 6.1  | $d(\gamma,p)n$ Calculations Above the $\pi^0$ Production Threshold.                 | 102 |
| A.1  | Set-up for Testing of the Scintillators Inside the $LH_2$ Target                    | 110 |
| B.1  | MRS Bend Plane Acceptance for the RHS of the Focal Plane                            | 115 |
| B.2  | MRS Non Bend Plane Acceptance for the RHS of the Focal Plane                        | 116 |
| B.3  | MRS Bend Plane Acceptance for the LHS of the Focal Plane                            | 117 |
| B.4  | MRS Non Bend Plane Acceptance for the LHS of the Focal Plane                        | 118 |
| B.5  | The Focal Plane Flat Acceptance Region  | 120 |
| B.6  | The Effect of Variations in Front End Acceptance on Transmission to the Focal Plane | 122 |

## CHAPTER I THE DEUTERON IN NUCLEAR PHYSICS

The deuteron was discovered in 1932<sup>(1)</sup> with the observation of a faint set of displaced emission lines in the Balmer hydrogen spectrum, which indicated the presence of a hydrogen isotope of approximately double the mass of ordinary hydrogen. With the growth of nuclear physics as an independent discipline, the deuteron, in its role as the simplest non-trivial atomic nucleus, naturally excited considerable interest as a nuclear system in which the detailed characteristics of the inter-nucleon force could be studied in relative isolation from complicating many body effects. Recently there has been a renewed surge of interest in the deuteron stemming in part from the disagreement of measurements of the zero degree photo-disintegration cross-section (hereafter referred to as ZDPD) with established theory. With this impetus, theorists have found that the cross-section at this angle, where the dominant electric dipole mechanism does not contribute, is much more sensitive to small and exotic pieces of the two nucleon wavefunction than had previously been realised. With this in mind, we decided to extend the available cross-section measurements above the energy threshold for pion production in order to provide a test of the revitalised deuteron theories in an energy region where the deuteron description would undoubtedly be much more complicated. The description and analysis of this experiment forms the subject matter for this dissertation.

The deuteron, the only nuclear bound state consisting of exactly one proton and one neutron, is an extremely loosely bound system when compared to other nuclei. The deuteron binding energy of approximately 2.2 MeV (1.1 MeV/nucleon) and typical inter-nucleon separation of 2.8 fm contrast sharply with the binding of  $\sim 8$  MeV/nucleon and separation of 1.2 fm typical for heavier nuclei. The deuteron has a mass of  $1875.628 \text{ MeV}/c^2$ , an electric charge of +1, a spin of 1, a magnetic dipole moment of

0.857393  $\mu_N$  and an electric quadrupole moment of 2.860 mb. These values are small compared to those of other nuclei, but their interest stems from the fact that they exist at all. The magnetic dipole moment is slightly different from the sum of the observed magnetic dipole moments a free neutron and a free proton, and the difference is termed the 'anomalous' magnetic dipole moment. The fact that an anomalous magnetic dipole moment and an electric quadrupole moment exist in the lowest energy nucleon-nucleon state was one of the first indications of an important facet of the strong nuclear force - its non-central character. Table 1.1 lists some of the deuteron's most important (experimentally measurable) properties.

Early models of the deuteron were phenomenological in character. A nucleon-nucleon potential shape was chosen whose characteristics were parameterised. The corresponding Schrödinger equation was then solved to predict the static properties of the deuteron in terms of the parameters of the potential. The most likely shape of the inter-nucleon potential was obtained by adjusting the potential's parameters to fit the experimentally measured properties of the deuteron.

As already stated, the existence of a deuteron electric quadrupole moment and an anomalous magnetic moment were the first indication that the nucleon-nucleon force was not strictly a central one. In a central potential, the various angular momentum states of a system (labelled by  $l$ , the integer number of angular momentum quanta  $\hbar$  possessed by the system) are all non-degenerate in energy, and the system may be expected to radiate energy until falling into the  $l=0$  (S) state. In order to account for the anomalous magnetic moment and the electric quadrupole moment, neither of which would be exhibited in a spherically symmetric S state, the nuclear potential must mix deuteron states of differing orbital angular momentum. The anomalous part of the magnetic dipole moment and the electric quadrupole moment may then be explained via the angular asymmetries associated with higher angular



**Table 1.1 - Elementary Properties of the Deuteron**

|                                   |  |
|-----------------------------------|--|
| <b>Chemistry</b>                  | <b>: <math>{}^2\text{H}_1^+</math></b>   |
| <b>Binding Energy</b>             | <b>: 2.225 MeV</b>                       |
| <b>Mass</b>                       | <b>: 1875.628 MeV/c<sup>2</sup></b>      |
| <b>Charge</b>                     | <b>: +e</b>                              |
| <b>Angular Momentum</b>           | <b>: <math>\hbar c</math></b>            |
| <b>Spin</b>                       | <b>: <math>\hbar c</math></b>            |
| <b>Isospin</b>                    | <b>: 0</b>                               |
| <b>Parity</b>                     | <b>: +</b>                               |
| <b>Magnetic Dipole Moment</b>     | <b>: 0.857393 <math>\mu_N</math></b>     |
| <b>Electric Quadrupole Moment</b> | <b>: 2.860 <math>\pm</math> 0.015 mb</b> |

momentum states. Since two nucleons, each with intrinsic spin 1/2, can produce a maximum combined spin of 1, the only higher angular momentum state which is available, consistent with the observed even parity of the deuteron and a total deuteron spin of 1, is the  $l=2$  (D) state. The general form of the simplest potential which mixes the S and D states, while respecting the principles of time-reversal-invariance, isotopic spin invariance, and parity conservation, is the spin-dependent tensor potential

$$S_{12}(r) = V_T(r) \left\{ \frac{3}{2}(\sigma_1 \cdot \hat{r})(\sigma_2 \cdot \hat{r}) - \frac{1}{2}(\sigma_1 \cdot \sigma_2) \right\}. \quad (I-1)$$

When this potential is added to the two nucleon central potential, the Schrödinger equation may be rearranged to yield two coupled equations for the S and D state pieces of the wave function. These are the the Rarita-Schwinger equations

$$\left[ \frac{d^2}{dr^2} + k^2 - M_d \langle 011 | V | 011 \rangle \right] u_0(r) - M_d \langle 011 | V | 211 \rangle u_2(r) = 0$$

$$\left[ \frac{d^2}{dr^2} + k^2 - \frac{6}{r^2} - M_d \langle 211 | V | 211 \rangle \right] u_2(r) - M_d \langle 211 | V | 011 \rangle u_0(r) = 0$$

$$\Psi_{\text{deuteron}} \equiv \frac{u_2(r)}{r} |211\rangle + \frac{u_0(r)}{r} |011\rangle. \quad (I-2)$$

In the preceding equation the  $|lsj\rangle$  are eigenstates of orbital angular momentum, spin and total angular momentum,  $M_d$  is the deuteron mass, and  $V$  is the inter-nucleon potential. The fact that these equations permit exact solutions (in practice the solutions are approximated to any required accuracy by computer) guarantees that in this system

we can make our first progress towards cutting the Gordian Knot of nuclear physics. This problem may be stated as: "does our nuclear model fail because

- a) our solution of the many body problem is inexact,
- or
- b) our two body physics is inexact?"

When the Rarita-Schwinger equations are solved for realistic NN potentials, the deuteron quadrupole moment, magnetic dipole moment, binding energy, and other static parameters, may be reconciled approximately with low energy experimental observations such as the nucleon-nucleon scattering length and the depth and range of the force necessary for large nuclei. Table 1.2, from Ref. 2, demonstrates the fit to a few of the measured deuteron properties for the Hamada-Johnston potential.

**Table 1.2 - The Predictions of the Hamada-Johnston Nucleon Nucleon Potential for a Few Deuteron Properties**

|                | Binding Energy | Quadrupole Moment     | Effective Range | %D state |
|----------------|----------------|-----------------------|-----------------|----------|
| Hamada-Johnson | 2.226 MeV      | 2.85 mb.              | 1.77 fm.        | 6.97     |
| Experiment     | 2.225 MeV      | $2.860 \pm 0.015$ mb. | $\sim 1.4$ fm.  | 4-7      |

Dynamic predictions involving the deuteron, for example in deuteron photo-disintegration, extend the use of the deuteron potential to describe the two nucleon outgoing state as a sum of spherical partial waves with different phase factors with waves characterised by  $l = j-1$  and  $l = j+1$  being explicitly mixed as before. These

outgoing waves are then linked to the initial state through the use of time-dependent perturbation theory. The expansion of the radiation field into a set of oscillating vector multipoles provides the time-dependent potential perturbation

$$H_{\text{int}} = \int \mathbf{J}_N(\mathbf{r}) \cdot \mathbf{A}^{\text{em}}(\mathbf{r}) d^3r \quad (\text{I-3})$$

where

$$\mathbf{A}^{\text{em}} = \frac{1}{\sqrt{V_N}} \sum_{\omega} \sum_{\nu} \sqrt{\frac{2\pi}{\omega}} [a_{\omega\nu}^{\text{OP}} \hat{\epsilon}_{\nu} e^{i\omega r} - \text{c.c.}] \quad (\text{I-4})$$

$\mathbf{J}_N$  = the nuclear convection and spin currents

$a^{\text{OP}}$  = the photon annihilation operator

$\epsilon_{\nu}$  = the polarisation of the photon.

For calculation, most authors have preferred to expand  $\epsilon_{\nu} e^{i\omega r}$  in terms of vector multipole fields, cutting off the expansion at some arbitrarily determined multipole order. For example, Partovi<sup>(3)</sup> included terms up to the octupole in his analysis.

The classical nuclear current may be written as a sum of magnetisation current and conventional convection current terms

$$\mathbf{J}_N(\mathbf{r}) = e \sum_{\alpha=1}^2 \left\{ \left[ \frac{1+\tau_3(\alpha)}{2i M_N} \right] \frac{1}{2} \delta(\mathbf{r}_{\alpha} - \mathbf{r}) [\vec{\nabla}_{\alpha} - \overleftarrow{\nabla}_{\alpha}] - \delta(\mathbf{r}_{\alpha} - \mathbf{r}) \frac{\mu_{\alpha}}{2M_N} \boldsymbol{\sigma}(\alpha) \times \vec{\nabla} \right\} \quad (\text{I-5})$$

### Fermi's Golden Rule for calculating transition rates

$$\Gamma_{0 \rightarrow \omega} = \lim_{t \rightarrow \infty} \frac{1}{t} \left| \langle \text{scatt.}; \omega | \int_{-t/2}^{t/2} H_{\text{int}}(t') e^{i\omega t'} dt' | \text{deut.}; 0 \rangle \right|^2 \quad (I-6)$$

completes the analysis. The main difficulty is the mathematical sophistication necessary to handle correctly the multitude of possible final states and contributing vector multipoles. The first thorough analysis along these lines was the done by F. Partovi<sup>(3)</sup> (1964), who managed to obtain reasonable fits to the deuteron photo-disintegration data over a fairly wide range of c.m. energies from 10-120 MeV. The analysis by Partovi has long been considered a standard, but its reputed good agreement with photo-disintegration data has suffered in recent years as accurate and consistent measurements of the  $d(\gamma,p)n$  reaction cross-section have been done. Older photo-disintegration experiments appeared to suffer from systematic errors much larger than the statistical errors involved in each measurement. This resulted in a large scatter in the world's data set and gave a fairly wide latitude to theorists trying to describe the reaction. Figure 1.1, showing Partovi's theory versus some recent data from Frascati<sup>(4)</sup>, illustrates the limitations of the theory from a modern standpoint. The angular shape is clearly not well described. However, the impetus for refining the deuteron model was dormant until 1976, when the Mainz collaboration<sup>(5)</sup> made its difficult ground-breaking measurements of the  $0^\circ$  photo-disintegration amplitude below the pion production threshold. Their data was later supported by single points measured at Louvain<sup>(6)</sup> and IUCF<sup>(7)</sup>, and by several recent low energy (10 MeV and less) measurements<sup>(8)(9)</sup>. Partovi's predictions were shown to be in disagreement with the data by approximately 20% (Figure 1.2), an amount which was completely unexpected in a comparatively low, and supposedly well understood, energy range. Since that time, renewed scrutiny of the deuteron nuclear current,  $J_N$ , the only point at which the classical analysis is amenable

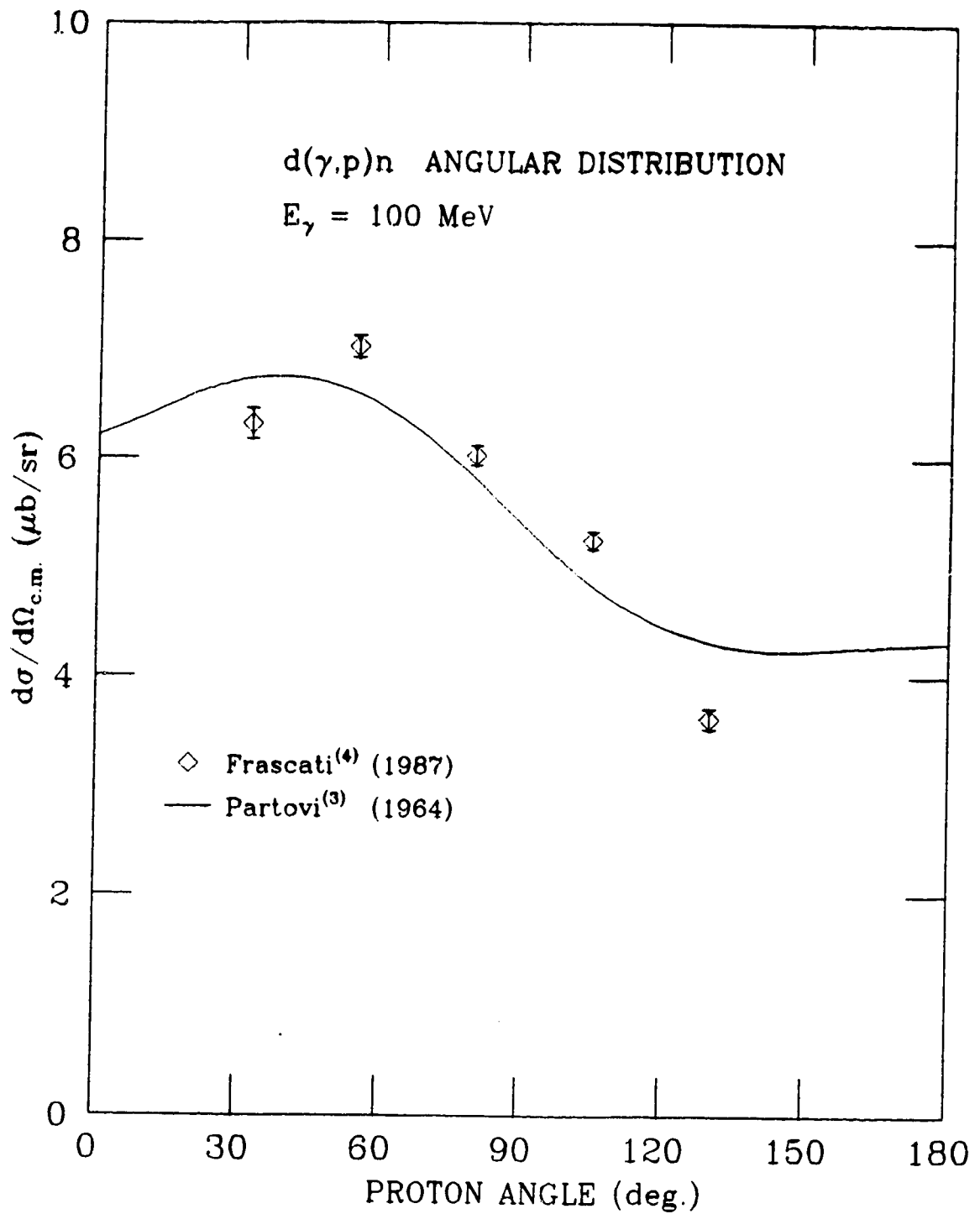


Figure 1.1 : Recent Frascati measurements of  $d(\gamma,p)n$  at 100 MeV are plotted against Partovi's theoretical curve.

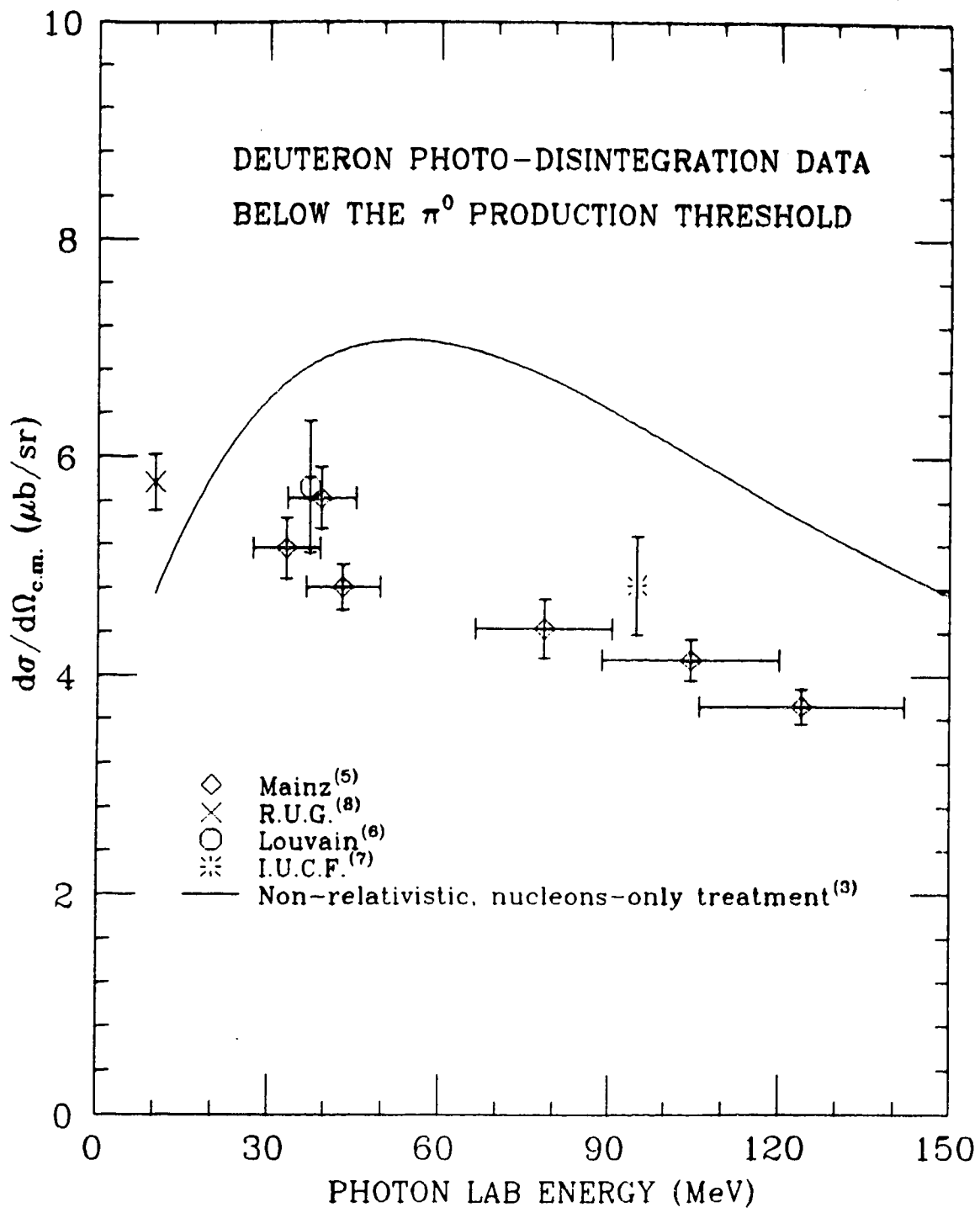


FIG 1.2 : The Mainz data, and confirming points, are in disagreement with pre-1976 treatments of the deuteron.

to change, has turned up a fair number of weaknesses in the theory. Relativistic corrections and meson exchange currents have been among the most intensely studied additions to the classical analysis.

A brief review of current theoretical work in this area will be given in chapter II. Since many of the corrections being considered are expected to increase in importance above the pion production threshold (meson exchange currents are an intuitively obvious example), it is important to obtain zero degree cross-sections in this region in order to test the revitalised theories. Data for the photo-disintegration reaction in this region have recently been measured at Frascati<sup>(10)</sup>. The experiment which is reported in this dissertation measured the radiative capture cross-sections above the pion production threshold in order to provide independent confirmation of the magnitude and variation of the cross-section in this region, and also to confirm the applicability of the detailed balance relation between the disintegration and capture cross-sections.



## CHAPTER II REVIEW OF RECENT THEORETICAL WORK

### II.1 PROBLEMS WITH THE CLASSICAL APPROACH

The failures of the classical approach (as exemplified by Partovi's calculations) to calculate deuteron photo-disintegration properties accurately at high c.m. energies, and at zero degrees, rest on various assumptions which either underlie the analysis or which were introduced in order to make the problem tractable. Some of the more critical assumptions are: that the problem is a two-body problem, that the nucleons are point particles, that nucleon resonances may be ignored, and that the Schrödinger equation correctly describes the motion of the two nucleons. Under the pressure of recent research on the nucleon-nucleon interaction, all of these assumptions, and some others which are not so evident, have been shown to make significant adjustments to calculations of photo-disintegration amplitudes.

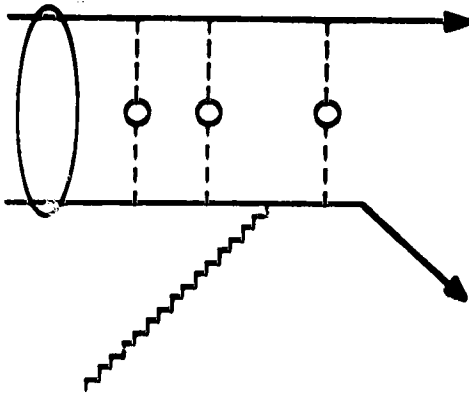
#### II.1.1 The deuteron D state

Because the predominant deuteron S state cannot contribute to an electric dipole (E1) transition at  $0^\circ$ , the largest part of the amplitude at this angle (at low to medium energies) is due to the E1 transition out of the deuteron D state. The zero degree transition amplitude is therefore a sensitive probe of the tensor part of the two nucleon potential. However, although the total cross-section for this transition is roughly proportional to the square of the asymptotic D/S state ratio ( $\eta$ ), theorists have been reluctant to adjust this parameter for fear of disturbing the fit to other well established experimental data (the deuteron quadrupole moment, for instance). It has been suggested recently, though, that deuteron quadrupole measurements have not been measuring the true deuteron D state probability because of the quadrupole moment of the meson field. The recent measurement of  $\eta$  by Rodning et al.<sup>(11)</sup>, using a technique

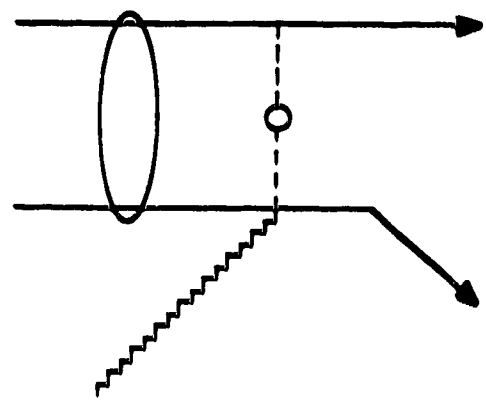
insensitive to MEC effects, gave a value for the asymptotic D/S ratio of  $2.56 \pm 0.04$  - significantly under the value of 2.7 commonly accepted. If a multiplicative correction factor of  $(2.56/2.7)^{**2} \sim 90\%$  is applied to the multipole amplitude part of Friar's calculation<sup>(12)</sup>, for example, a sizeable portion the disagreement between theory and experiment (for the zero degree cross-section below the  $\pi^0$  production threshold) is resolved<sup>(13)</sup>.

### II.1.2 Meson exchange currents

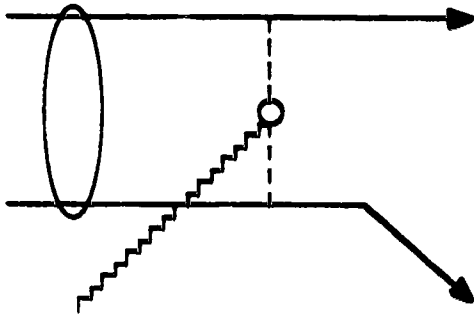
The treatment of the deuteron as two nucleons moving in an effective nuclear potential ignores the fact that real nuclear forces arise via the exchange of intermediate mesons (principally the  $\pi^\pm$  and  $\pi^0$  at long range). The modification of the nuclear multipole moments due to the exchange of non-retarded light charged particles may be dealt with in a consistent manner by the imposition of conventional current conservation for the nucleons (Siegert's Theorem<sup>(14)</sup>), but  $(v/c)^2$  corrections to the theorem in the presence of these currents have been examined in the light of recent events and found to yield a small but significant improvement of the fit to the data<sup>(15)</sup>. Corrections for finite exchange time may only be done within the framework of a relativistic theory and introduce charges and currents which are not directly related to the nucleonic motion. Such contributions are usually calculated diagrammatically via the Feynman prescription for quantum field theory. Some of the most important Feynman diagrams for photo-disintegration are shown in Figure 2.1. The relativistic Lagrangian correction term obtained from each diagram is reduced to an equivalent potential for successive orders of  $p/m$ , the meson's momentum to mass ratio. Theorists have generally disregarded the MEC at low to medium energies, as it cannot compete in importance to the dominant E1 transition. However, in places where the E1 is suppressed, MEC effects may be significant. A notable example of this is the  $\sim 10\%$  effect MEC inclusion has on the magnetic dipole (M1) transition amplitude just above the threshold for the photo-disintegration reaction. The discovery of this explained a



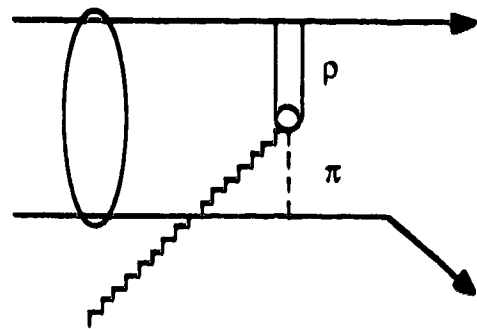
Photon/nucleon interaction with rescattering



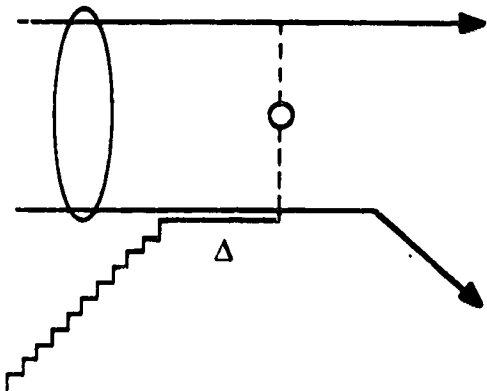
Photon/nucleon/meson interaction



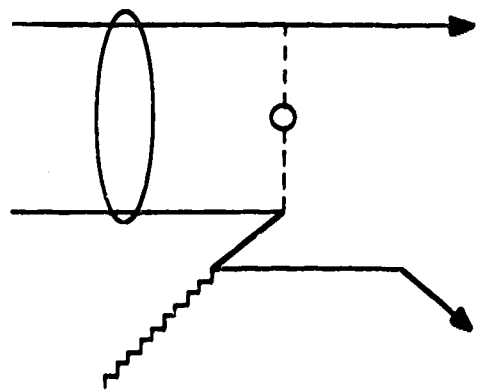
Photon/meson interaction



Photon/meson/meson interaction



Photon/nucleon/delta interaction



Photon/anti-nucleon/nucleon interaction

Figure 2.1 : A few Feynman diagrams for photo-nuclear interactions

serious discrepancy in the predicted capture total cross-section of thermal neutrons, since the M1 transition dominates the reaction at very low energies.

Adding the MEC contribution to the theory presents some difficulties. There are various families of unitarily equivalent transformations corresponding to pion exchange. In a perfect world the form of the wavefunction for the deuteron would dictate the family of MEC which one should use, but in practice the deuteron wavefunction is semi-phenomenological and is not invariant under any of the transformations  $e^{i\epsilon U}$ , where  $U$  is the hermitian pion exchange operator. This is the 'method chosen' problem, and leads to a high degree of model dependence attached to all MEC corrections. Furthermore, the form of the pion-nucleon vertex is a matter of conjecture. Pseudo-scalar (PS) vertex treatments have been common because of the resulting renormalisability of the interaction, but result in quantitatively worse fits to the ZDPD data and are also inconsistent with a number of other measurements, such as  $\pi^0$  photo-production on nuclei. Recently the pseudo-vector (PV) vertex has been popular due to its chiral invariance and also the realisation that the pion/nucleon Lagrangian was an effective one arising from underlying QCD dynamics, and therefore did not need to be renormalisable. The use of a PV interaction results in a small improvement of the fit of theory to experiment. The fact that the nucleons are not free and thus can be 'off-shell' complicates the form of the vertex, but there is no consensus today about how to handle off-shell interactions in a completely consistent manner. Figure 2.2 illustrates the effect of adding MEC to a multipole calculation of the zero degree  $p(n,d)\gamma$  reaction<sup>(12)</sup>. Above the pion creation threshold, the situation becomes even more unclear as the MEC effects grow in importance. However models incorporating MEC effects show a steep rise in cross-section in this region compared to their multipole-only counterparts. Figure 2.3 illustrates the prediction of Lager<sup>(16)</sup> from a diagrammatic expansion of MEC contributions. Clearly the increased sensitivity

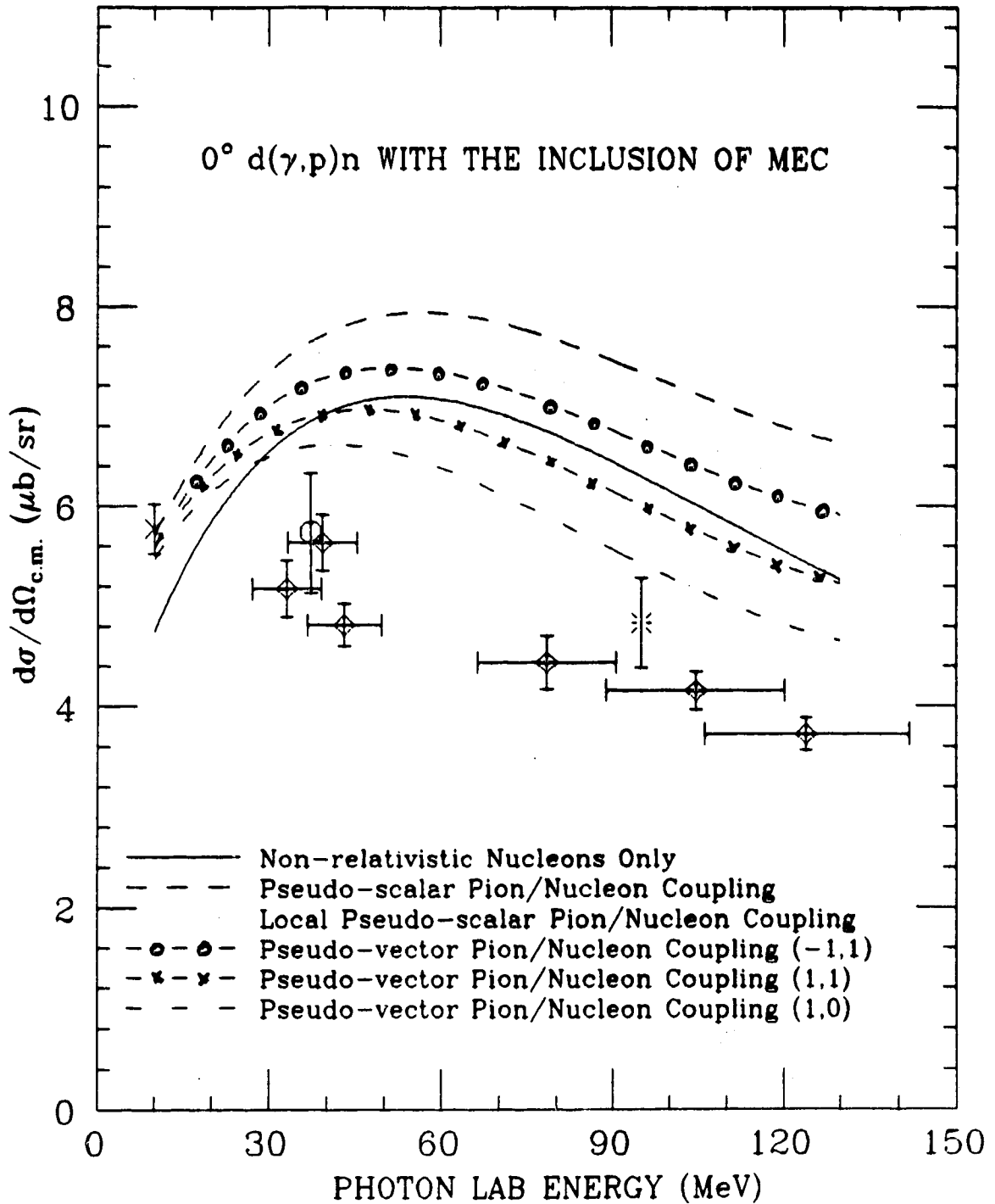


FIG 2.2 : The effect of adding different families of meson exchange currents to a NR deuteron model<sup>(12)</sup>. The numbers in brackets parameterise the different families of MEC.

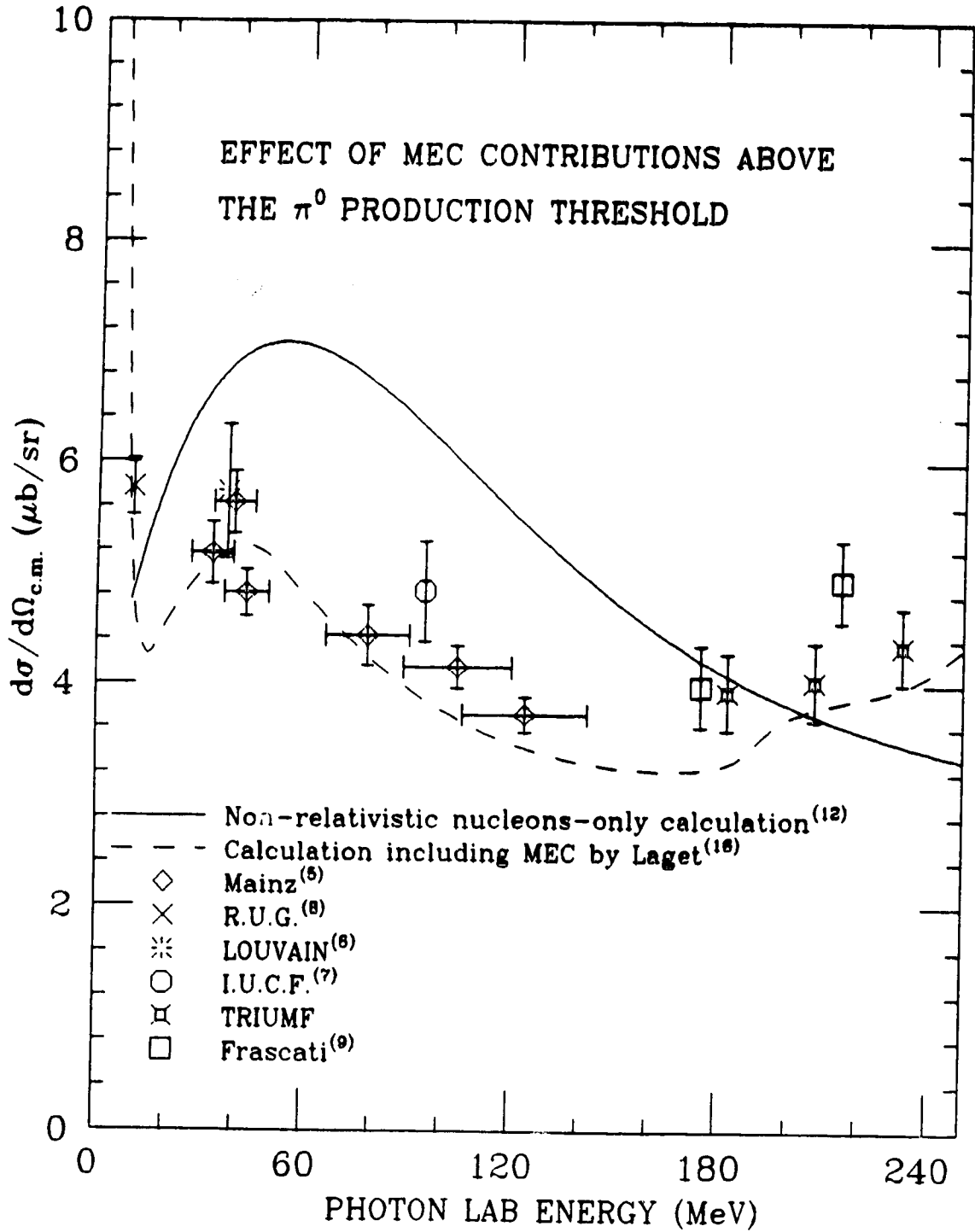


FIG 2.3 :  $d(\gamma,p)n$  calculations which include MEC all rise above the  $\pi^0$  production threshold, while NR models fall.

above pion production threshold of ZDPD predictions to MEC inclusion should permit a better choice between available deuteron and MEC models. A complete description will clearly not be possible until the deuteron wavefunction is calculated entirely from a potential based on inter-nucleon exchange currents (i.e. lacking phenomenological pieces which do not have the correct chiral transformation properties). Various researchers<sup>(17)</sup> are currently working on this difficult problem.

Another consideration is how to phase in meson exchange currents with a phenomenological short range potential process. Clearly, the concept of an exchanged virtual particle becomes ambiguous for inter-nucleon separations which are less than its Compton wavelength. The relativistically invariant way is to use a form factor at the vertex, generally a monopole one of the form

$$\frac{\Lambda^2 - m_\pi^2}{\Lambda^2 - k^2},$$

where  $k$  is the exchanged momentum,  $m_\pi$  is the mass of the exchanged pion and  $\Lambda$  is an experimental parameter known as a cut-off mass. Authors who have compared this form of short range cut-off against a linear cut-off<sup>(18)</sup> report that the difference is small for  $0^\circ$  photo-disintegration, reflecting the relative insensitivity of this reaction to details of the short range interaction. Unfortunately, the experimental situation concerning the size of  $\Lambda$  is quite uncertain<sup>(19)</sup>. Various experimental results are better fit by values of  $\Lambda$  from 850 to 1250 MeV, while exchange model potentials generally use even larger values. In their 1987 paper, Jaus and Woolcock<sup>(19)</sup> found that the choice of  $\Lambda$  was quite significant for photo-disintegration observables from 100 MeV or so upwards.

The need to distinguish between the  $\pi^0$  and  $\pi^\pm$  rest masses when one

constructs models of the NN potential has been pointed out<sup>(18)(19)</sup>. Most models which contain long range potentials calculated from MEC considerations use an effective coupling constant based on the  $\pi^0$  mass which is appropriate to proton-proton scattering but not neutron-proton scattering which has an isospin changing ( $T=1$ ) component. This is a particularly bad situation since the E1 transition is  $T=1$ . The size of this effect is 8% at 40 MeV (c.m.)<sup>(19)</sup>, which is a startling result given that the difference between charged and neutral pion rest masses is only 3%.

The prediction that polarisation observables should be strongly affected by MEC (for instance, in ref.<sup>(20)</sup>) has led to a number of recent experiments along this line. The analysing power data of Hugi et al.<sup>(21)</sup>, and Cameron et al.<sup>(22)</sup>, which together span a region from below to well above the pion production threshold were clearly better described by a two nucleon model including meson exchange currents calculated by Laget<sup>(23)</sup>. An improvement of the correspondence between theory and data by the inclusion of the  $\Delta$ -isobar currents was also noted in regions well below the point at which the  $\Delta$  creation amplitude starts to compete with the E1 amplitude.

### II.1.3 Relativistic kinematic corrections

Because most treatments of the deuteron start with the non-relativistic Schrödinger equation, relativistic effects such as the spin-orbit coupling and the Darwin-Foldy term must be generated by means of a Foldy-Wouthuysen transformation and inserted separately. One such term, the spin-orbit force, has long been a familiar relativistic correction but has not been used in deuteron photo-disintegration calculations because of its small size compared to the electric dipole interaction. The spin-orbit piece of the Hamiltonian has the form<sup>(12)</sup>



$$H_{s.o.} = \frac{1}{4mc^2} \sum_i (2\mu_i - e_i) \sigma_i \times \pi_i \cdot E_{ext.} \quad (II-1)$$

where  $m$  is the nucleon mass,  $\mu_i$  and  $e_i$  are the magnetic moment and charge of the  $i$ 'th nucleon, and  $\sigma_i$  and  $\pi_i$  are the spin and momentum operators for the  $i$ 'th nucleon.  $E_{ext}$  is the external electric field, in this case provided by the photon. The spin-orbit term takes into account the interaction of the deuteron magnetic moment with the magnetic field of the photon. In several recent papers<sup>(12)(13)</sup> it has been pointed out that this term is responsible for perhaps a 20% reduction in the theoretical cross-section.

Another intrinsically relativistic term, the Darwin-Foldy correction, is given by<sup>(25)</sup>

$$H_{D.F.} = \frac{-1}{8m^2} \nabla \cdot E \quad (II-2)$$

This term, one of the relativistic corrections arising from the Foldy-Wouthuysen reduction of a Dirac equation with minimal electromagnetic coupling, vanishes for real photons, but not for virtual ones. This correction points out the need to consider the nucleon form factor contribution to the  $(d, \gamma)$  process - a contribution which may be expected to increase significantly with increasing photon energy. Friar et al.<sup>(12)</sup> have evaluated the contributions of both this and the spin-orbit terms (figure 2.4). As mentioned before, the spin-orbit term is important throughout the photon energy range from 20-140 MeV. The Darwin-Foldy term is initially small, but by 140 MeV has become an important 10% correction. Higher energy data should highlight this growing importance.

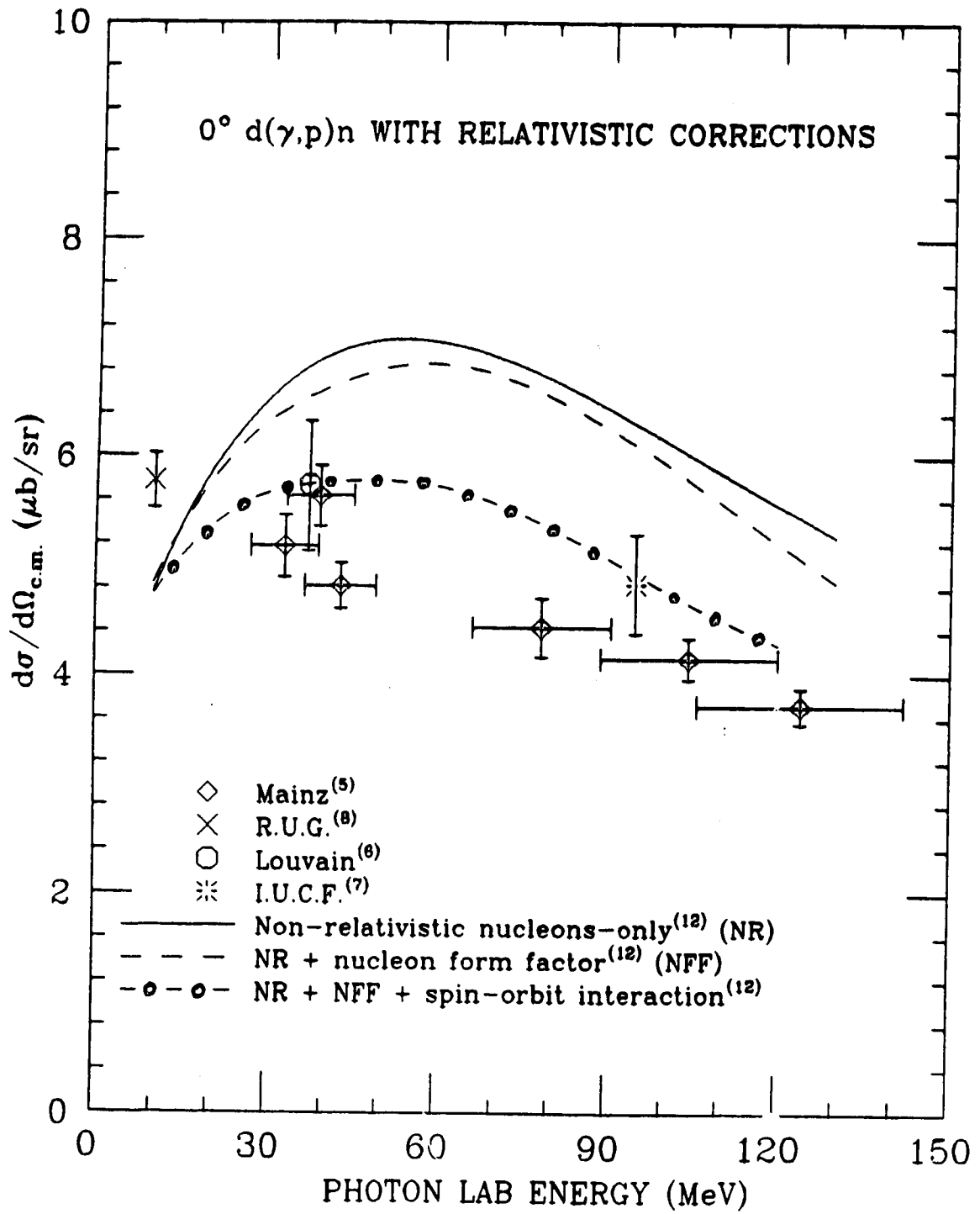


FIG 2.4 : Relativistic corrections to the amplitude for deuteron photo-disintegration at  $0^\circ$  are significant.

The Hamiltonian term

$$H = \frac{i}{8m^2} \sum_{i \neq j} e_i(\mathbf{q} \cdot \mathbf{r})(\mathbf{q} \cdot \mathbf{p}_i) , \quad (\text{II-3})$$

where  $\mathbf{q}$  is the photon momentum, is a third kinematic correction which is necessary to provide a Hamiltonian correct to order  $1/c^2$ . This term encompasses both nucleon recoil and MEC corrections to the wavefunction of a system of moving particles. Cambi et al.<sup>(26)</sup> have evaluated this term for both PS and PV interactions and find that, while the PV treatment results in a small improvement in the theoretical fit to the data, the PS interaction is large and in the opposite direction.

The Galilean transformation properties of the Schrödinger equation also introduce mathematical difficulties when relating quantities in the starting state ( $\gamma + d$ ) to those in the final state ( $n + p$ ). The co-ordinate transformation between the two most convenient co-ordinate systems for defining the incoming and outgoing states, the deuteron rest frame and the  $n + p$  center of mass frame, is properly done by a relativistic boost, not the Galilean transformation usually employed for simplicity. Hwang, Londergan and Walker<sup>(27)</sup> addressed this last problem by constructing a gauge invariant formalism (for nucleons only) in the Breit interaction frame, which treats the deuteron and scattering states symmetrically, and then did a full relativistic transformation into the deuteron rest frame. They found that this treatment generated a significant correction to the classical, non-gauge invariant, theory. Hwang et al. and others<sup>(15)(27)</sup> have pointed out that the factor  $(1 + \omega/2m)$ , where  $\omega$  is the photon energy, in the electric multipole transition amplitudes of Partovi (resulting from his choice of form for the current conservation law) disappears when the current conservation law is *derived* in a relativistic treatment.

The size of these three fundamentally relativistic corrections to ZDPD speaks persuasively for the need to construct a fully relativistic model of the NN interaction in order to properly evaluate them. Our current understanding of the situation may not be as clear as is commonly thought. Jaus and Woolcock<sup>(19)</sup>, for instance, find that if the deuteron photo-disintegration amplitude is divided into non-relativistic amplitude + relativistic kinematic corrections (together labelled IA), and a meson exchange piece (MEC), then no independent variation of the contributions of the IA and MEC parts appears to be able to explain all the data, including total cross-section, differential cross-section and polarisation observables. IA by itself appears to be too low in some instances. Since a good understanding of this piece is fundamental to all nuclear physics calculations above very low energy, this is somewhat distressing.

#### II.1.4 Nucleon isobars

As the delta resonance region, which peaks at around 600 MeV neutron energy, is approached, the incoming  $\gamma$  may excite one of the nucleons into an isobaric state. If a  $\Delta(1232)$  resonance is excited, the vertex function  $f_{\pi NN} f_{\pi N \Delta} f_{\pi N \gamma}$ , corresponding to the photon/nucleon/delta interaction illustrated in figure 2.1, must be established. Experiments tend to indicate that this product of vertex strengths is up to 20% different from the quark model prediction<sup>(19)</sup>.

The proton polarisation for the  $d(\gamma,p)n$  (analysing power for the inverse reaction) has been shown to be theoretically quite sensitive to the inclusion of isobar currents<sup>(23)</sup> in regions well below the threshold for  $\Delta$  creation, as mentioned in the discussion of MEC, section II.1.2. A coupled channels calculation<sup>(29)</sup> has evaluated the influence of the virtual  $\Delta$  creation on the zero degree photo-disintegration amplitude (this calculation will be discussed in more detail in chapter VI) and found that this process lowered the cross-section by approximately a 10% over a wide range of energies, resulting in an improvement of the fit to the data. Related experiments of

these type, hopefully leading to an over-determination of the many parameters involved in any process involving the strong nuclear reaction, give a good example of how experiment and theory must co-operate if our understanding of particle properties is to advance. What is now needed are more, particularly accurate, data in the areas predicted to be sensitive to nuclear structure components such as the  $\Delta$ -isobar.

Another interesting consideration is the possible interaction of the incoming  $\gamma$  with a  $\Delta\Delta$  component of the deuteron wavefunction. Besides allowing the deuteron to be in a G ( $l=4$ ) state, the  $\Delta\Delta$  isospin-1 state has a mixed isosymmetry, permitting many more final states to be coupled to the initial state through the E1 transition mechanism, which changes isospin by one unit. Clearly a good experimental knowledge of the  $\Delta\Delta\gamma$  vertex function (the cut-off mass is unclear here as well), as well as the electromagnetic form factor of the  $\Delta$ , will be necessary in order to investigate the relative size of this contribution to photo-disintegration. A completely relativistic theory of the deuteron is also essential in order to know the  $\Delta\Delta$  state probability.

As a final note to this brief survey of the possible influence of the  $\Delta$  in the deuteron wavefunction, we refer the reader to H.T. Williams important paper<sup>(30)</sup> in 1985 in which it was pointed out that the form of the spin 3/2 propagator in general use was applicable to the  $\Delta$  only when it was on the mass shell. In this paper, the more general form of the  $\Delta$ -propagator (from H. Behrends and C. Fronsdal<sup>(31)</sup>) was given which leads<sup>(19)(30)</sup> to simpler forms for the  $\gamma N\Delta$  and  $\pi N\Delta$  vertex functions and unique predictions for such processes as  $d(\gamma,p)n$ ,  $N(\gamma,p)N$  and  $N(\pi,\pi)N$ <sup>(19)</sup>. In addition, it was pointed out in Williams' paper that the proper treatment of the  $\Delta$  coupling required an associated coupling to an anti- $\Delta$  for which the amplitude was non-negligible. Williams found that the anti- $\Delta$  coupling for the process of nuclear Compton scattering  $N(\gamma,\gamma)N$  was of comparable size to the  $\Delta$  coupling. A re-examination of deuteron photo-

disintegration amplitudes will clearly be necessary when these corrections have been evaluated by theorists working on electromagnetic transitions.

## II.2 SUMMARY

To conclude, a large number of corrections to ZDPD have appeared in the 15 years since the experimental discrepancy first appeared in 1976. Indeed, there are so many separate factors of 5-10% proposed to explain the 20% discrepancy, that it may have been fortunate that the original theory was as far away from the data as it was - alerting the physics community to the need for a re-evaluation of the domains of applicability of the simplifying assumptions commonly used. The situation at present appears to be at somewhat of an impasse. The most recent calculations<sup>(19)</sup>, including the best knowledge of kinematic and MEC corrections are still significantly higher than the data in the region of 10-140 MeV c.m. energy. Hopefully the situation will be clarified by the new data now appearing at higher energies, provided that additional short range effects do not appear in sufficient quantities to further complicate the situation. Alternatively, if the situation at lower energies can be solved independently of the data above the pion production threshold, the new data might be used as a sensitive probe of the aforementioned short range effects (6 quark bags, photon-delta couplings etc.).

## **CHAPTER III - DESCRIPTION OF THE EXPERIMENT**

### **III.1 THE TRIUMF CYCLOTRON**

TRIUMF (for TRI-University Meson Facility) is a medium energy isochronous cyclotron situated in Vancouver, Canada, and jointly managed by four universities: Simon Fraser University, the University of British Columbia, the University of Victoria, and the University of Alberta. It was first operated in 1974, providing intense proton beams suitable for generating secondary meson beams for experiments. It has also supported a large group of experimenters researching proton and neutron induced reactions using a second extracted beam of protons. Figure 3.1 shows the general plan of the TRIUMF cyclotron building, including the cyclotron, the meson experimental hall and the proton experimental hall.

An Ehlers ion source, well removed from the cyclotron vault, provides  $H^-$  ions to the cyclotron, which is constructed from 6 large magnets in a pinwheel-like formation with RF acceleration cavities. Careful shaping of the magnets ensures that the particle bunches arrive at the RF cavities after a constant flight time interval - allowing the continuous acceleration of particle bunches inside the cyclotron and a potential 100% duty factor. The actual duty factor may be varied between 0.1 and 100.0% by modulating the output of the ion source. Because  $H^-$  ions are accelerated, easy extraction of the beam is achieved by lowering thin foils into the path of the ions in the cyclotron tank in order to strip off their electrons. The resulting proton beam is then directed out of the cyclotron and into the experimental beamlines by the cyclotron's magnetic field. Current in the experimental beamlines may be adjusted by raising or lowering the stripping foils to intercept a smaller or larger fraction of the accelerated beam. Two different foils, at different radii on opposite sides of the





cyclotron tank, permit the simultaneous extraction of two beams at different energies. Some of the beam is lost due to breakup of the  $H^-$  ions in the electric fields seen by the relativistic protons moving through the cyclotron's magnetic field, and also via collisions with gas molecules. This is kept to 5-10% by maintaining a hard vacuum ( $5 \times 10^{-8}$  Torr) in the cyclotron, by the use of large, low field bending magnets, and by operating the RF at 23.06 MHz - 5 times the  $H^-$  ion rotational frequency. The end result is a reliable extracted beam of up to 150  $\mu A$ , and with an energy which is variable continuously from 180 to 520 MeV. An energy resolution of up to 0.5 MeV is obtained by stripper foil placement in the cyclotron tank with 'one turn' accuracy, although for experiments where the beam resolution is not critical the cyclotron is usually operated in a mode where an energy spread of 1.0 MeV is typical. The time structure of the beam is a series of 3 ns bunches at 43 ns intervals.

### III.1.1 The Medium Resolution Spectrometer

The Medium Resolution Spectrometer (MRS) is located on beamline 4B, in the proton experimental hall. This spectrometer is capable of momentum analysing particles of up to 1.4 GeV/c with a resolution ( $\Delta p/p$ ) of  $2 \times 10^{-4}$ . Protons extracted from the cyclotron are transported by a series of dipole, quadrupole and solenoid magnets designed to control the beam direction, size, momentum spread, and (if required) polarisation direction at the entrance to the MRS, where the primary target is located. Figure 3.2 shows a scale picture of the MRS along with a schematic of the various wire chamber and scintillator positions relevant to this experiment. Charged particles from a reaction in the primary target first pass through two multi-wire gas proportional chambers (the Front End Chambers, or FECs), with wires at 5 mm intervals in both directions perpendicular to the beam, and which allow one to trace the scattered particle back to the target. The reaction products then enter a quadrupole/dipole combination with a vertical bend plane. Two more proportional counters (the Vertical Drift

## THE MEDIUM RESOLUTION SPECTROMETER

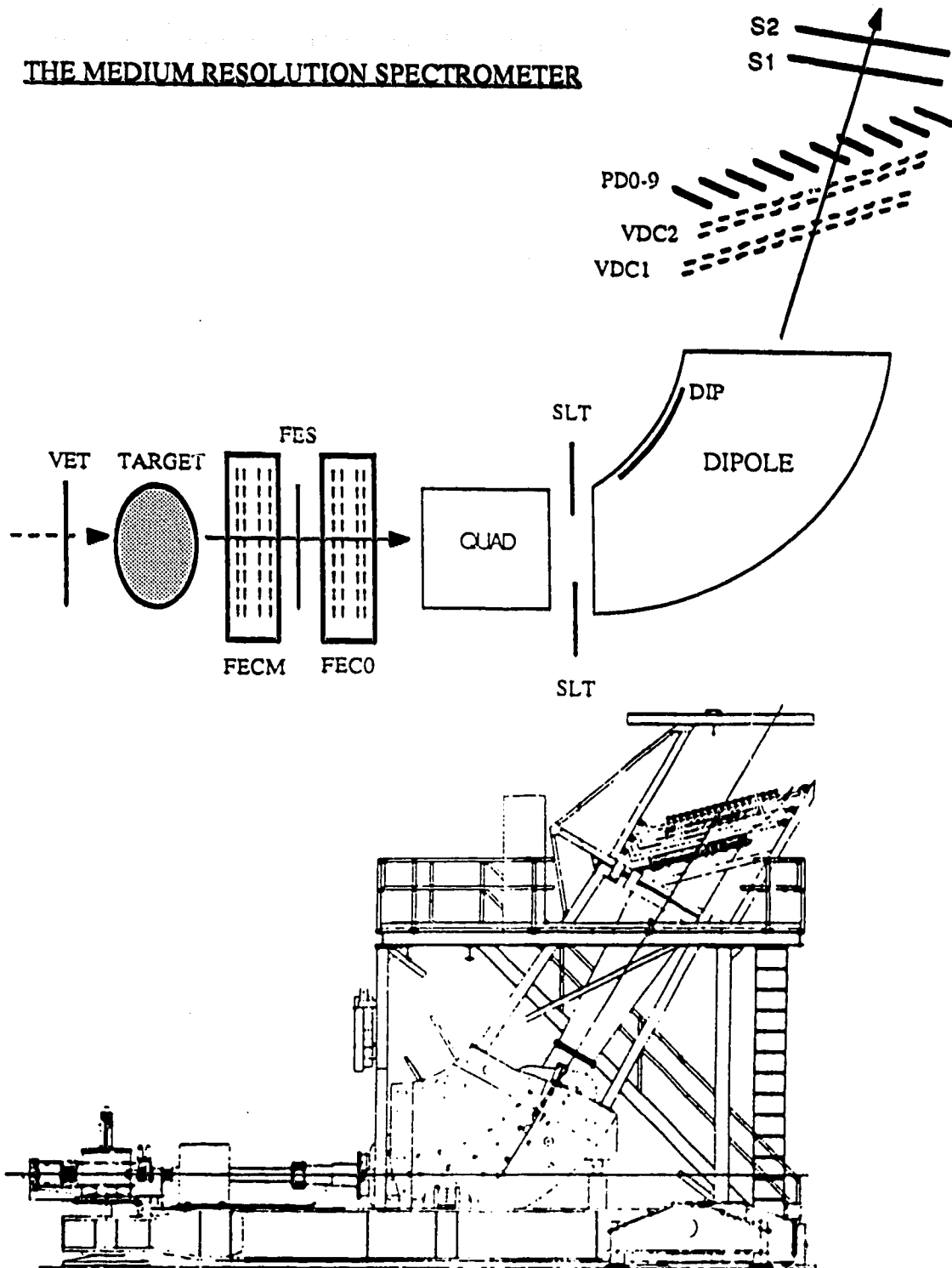


Figure 3.2 : The top is a schematic diagram of the MRS when running a CHARGEX experiment. The bottom is a scale picture of the MRS showing support structure.

Chambers, or VDCs) are located at the exit of the dipole. Each VDC contains two wire planes, the x and u planes, which have wires oriented at  $30^\circ$  to one another and whose normals are at  $45^\circ$  to the beam direction in order to obtain a maximum resolution of  $50 \mu\text{m}$ . The particle track reconstructed by the VDCs permits the computation of the focal plane crossing point, and hence of the particle's momentum. Plastic scintillation counters at the top and bottom of the MRS provide both  $\Delta E$  and time-of-flight information. The characteristics of the MRS have been well measured<sup>(32)</sup>, and it was an obvious choice for measurements of the  $p(n,d)\gamma$  reaction.

### III.1.1 The CHARGEEX Facility

The CHARGEEX facility is situated just in front of the normal MRS target location. Figure 3.3 schematically illustrates the position of various elements in this system, and table 3.1 gives actual experimental dimensions. The CHARGEEX facility consists principally of a lithium target situated inside a dipole magnet. Neutrons produced from the reaction  ${}^7\text{Li}(p,n){}^7\text{Be}$  continue in a straight line through the magnet and onto a secondary target, which in our case was a liquid hydrogen ( $\text{LH}_2$ ) target located near the pivot point of the spectrometer. For this experiment at  $0^\circ$ , a flux of approximately  $2.8 \times 10^6$  neutrons per second was incident on the  $\text{LH}_2$  target for every 100 nA of initial proton beam. Proton beam current varied between 200 and 500 nA.

Table 3.1 - Experimental Dimensions

|                              |    |                             |   |         |
|------------------------------|----|-----------------------------|---|---------|
| ${}^7\text{Li}$ (p,n) target | -> | MRS pivot point             | = | 92 cm   |
| MRS pivot point              | -> | $\text{LH}_2$ target center | = | 11.3 cm |
| $\text{LH}_2$ target center  | -> | First wire chamber          | = | 25.7 cm |
| First wire chamber           | -> | Second wire chamber         | = | 26.6 cm |
| MRS pivot                    | -> | Focal plane                 | = | 11 m    |

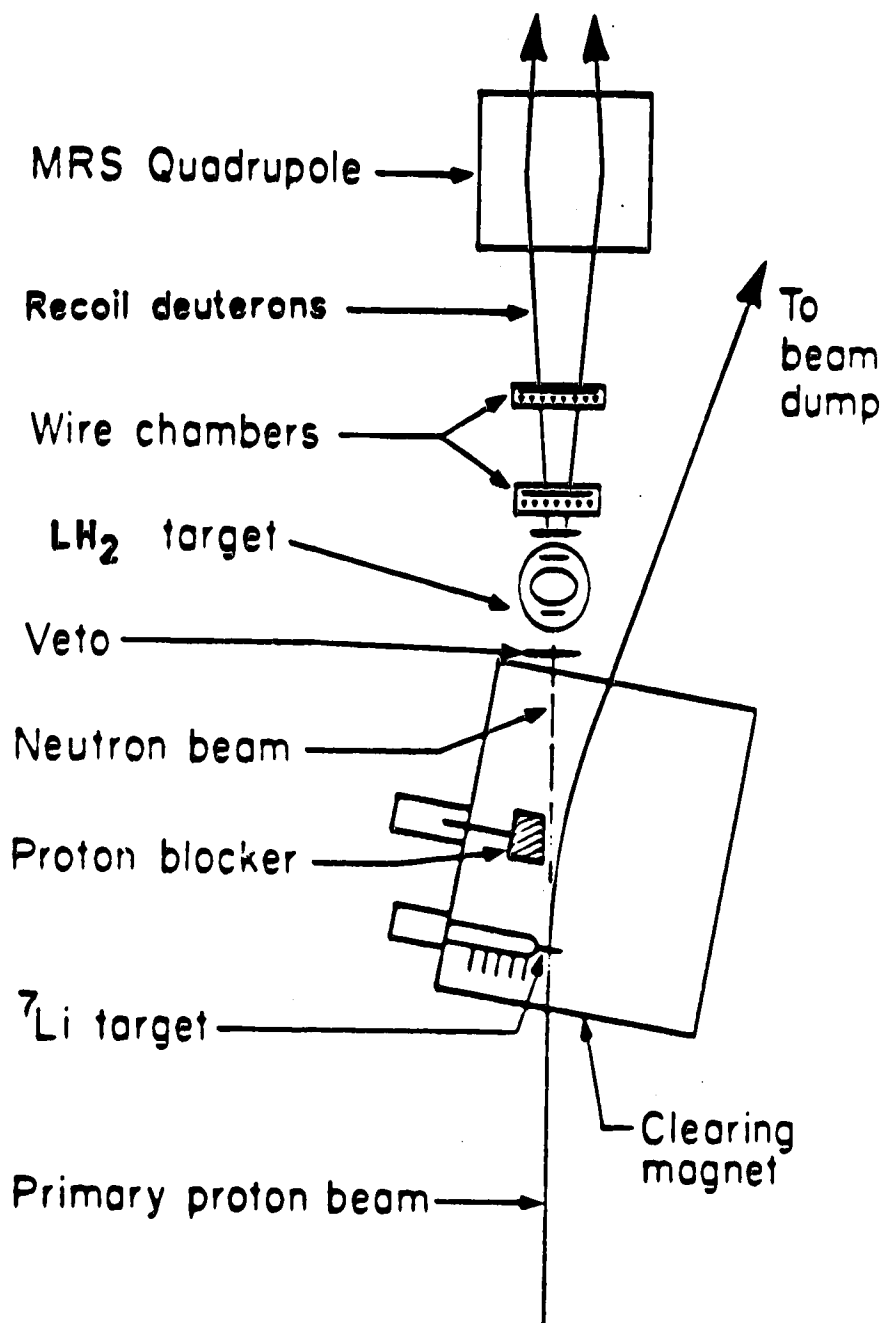


Figure 3.3 : The CHARGEEX Facility

After interaction with the lithium, the remaining proton beam is deflected  $20^\circ$  by the sweeping magnet into a Faraday cage and beam dump near the proton hall wall. Protons which scatter from the lithium at an angle which would permit them to be bent by the clearing magnet back into the neutron beamline are stopped by a movable beam blocker inside the magnet.

At the exit of the CHARGEEX sweeping magnet, two different particle groups impinge on the  $\text{LH}_2$  target: neutrons from the (n,p) reaction on lithium, and neutral hydrogen produced by electron capture in the lithium. The neutral hydrogen beam (which quickly reverts to a proton beam after passing through the exit window of the clearing magnet) provides, after correction for the effects of the fringing fields of the CHARGEEX magnet, an excellent indication of the true zero degree angle in the system. Because of the low electron density in lithium, a short run using a lead target was used to provide a neutral hydrogen beam of sufficient current for a determination of the true zero. After passage through the magnet exit window, protons from the stripped hydrogen, as well as any protons not stopped by the beam blocker, are vetoed by means of a 1/16" plastic scintillator placed directly in front of the  $\text{LH}_2$  target. The remaining beam, now identified as neutrons only, then interacts with the  $\text{LH}_2$  target.

## III.2 PROCEDURAL DETAILS

### III.2.1 Nuclear reactions in the LH<sub>2</sub> target

As previously discussed, protons from the cyclotron were incident on a <sup>7</sup>Li target in the CHARGEEX facility, producing a neutron beam which passed through a charged particle veto scintillator and onto a liquid hydrogen target while the remaining proton beam was swept aside into a beam dump. After an interaction with the hydrogen in the target cell, the reaction products entered the MRS to be momentum analysed. Three of the possible reactions were especially important because of their rate and because charged particles were produced with similar momenta:

- a)  $p(n,d)\gamma$  Deuteron production with gamma emission
- b)  $p(n,d)\pi^0$  Deuteron production with neutral pion creation
- c)  $p(n,p)n$  Elastic nucleon-nucleon scattering

The reaction products from a, b, and c above have different momenta according to their various relativistic kinematics. In figure 3.4 the kinematic loci are illustrated.  $p(n,p)n$  dominates the total cross-section for neutron interactions at low to medium energies. It has a cross-section of approximately 10 mb/sr (at 0° c.m.), and our 6 cm thick LH<sub>2</sub> target provided on the order of 50 protons/s into the acceptance of the spectrometer for every 100 nA of current incident on 220 mg/cm<sup>2</sup> of <sup>7</sup>Li. In order to minimise the number of magnetic tapes, which would otherwise have rapidly filled with elastic scattering data, the number of fully processed elastically scattered proton events was reduced by means of a hardware decision based on time-of-flight through the spectrometer. This also had the beneficial effect of reducing the computer deadtime

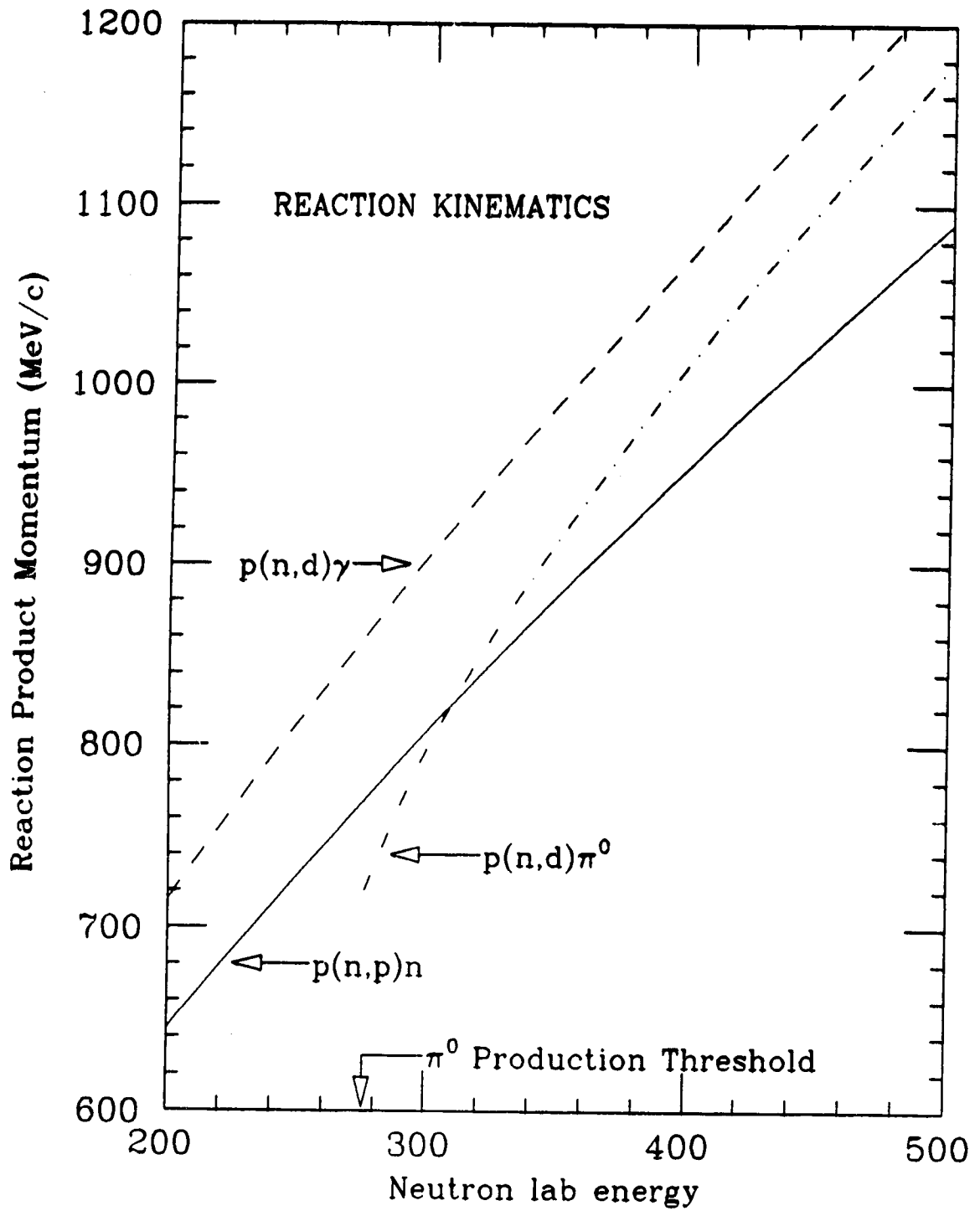


FIG 3.4 : The kinematic loci of the charged product of three neutron induced reactions at  $0^\circ$  in hydrogen.



in our system

Reaction b) has a cross-section which rises rapidly from the threshold energy for pion creation at an incoming neutron energy of  $\sim 275$  MeV to a peak in the  $\Delta$  resonance region. In the energy range of this study (360 - 460 MeV) deuterons from  $p(n,d)\pi^0$  are produced at rates of between 50 to 150 times greater than that of the  $p(n,d)\gamma$  reaction of interest. It is therefore important to be able to identify the  $p(n,d)\gamma$  deuterons unambiguously, which we achieve by momentum analysing the two deuteron groups using the MRS spectrometer. At the highest energy, where the relative separation of the two groups is smallest, the momentum difference was 4.5% with a momentum resolution of approximately 1%. This resolution is somewhat worse than the optimum resolution of the spectrometer system for two reasons: large energy straggling in our 6 cm  $\text{LH}_2$  target, and operating of the beam in the achromatic, or non-dispersed mode. Better resolution can be attained in the dispersed mode, where the beam momentum varies with its offset at the target, but this was not necessary for our purposes.

### III.2.2 Background reactions

Test runs in the neutron area in 1986, using neutrons produced by knock-on reactions in  $\text{LD}_2$  at 9° lab, indicated that neutron induced deuteron creation on the carbon present in scintillators and wrappings,  $^{12}\text{C}(n,d)\text{X}$ , was a major source of background for  $p(n,d)\gamma$ . The size of this background depends on the amount of material in the beam's path, of course. For our experimental set-up on the MRS there was approximately 0.1" of material (mostly CH) made up from target walls, wrappings, and the trailing edges of scintillators. This amount of material yielded event rates from  $\text{C}(n,d)\text{X}$  at a rate comparable to that of the  $p(n,d)\gamma$  reactions occurring in the 6 cm of liquid hydrogen. We were therefore faced with the prospect of either making an

empirical subtraction of this background from the  $p(n,d)\gamma$  peak, or of finding some way to reduce the background substantially. The first method would have necessitated much longer counting times. For instance, a 1:1 ratio of good events to background events would mean that run time must be increased by a factor of almost 6 times compared to the no-background case in order to achieve the same statistics in the peak-background calculation. With this in mind, a new  $LH_2$  target was developed by the TRIUMF Cryogenic Targets Group (see fig. 3.5) in which it was possible to insert two 4 cm x 6 cm x 0.025 cm plastic scintillators inside the region of cold  $H_2$  gas close to the target cell itself. The signals from these two scintillators were used in the offline analysis. A signal from the scintillator downstream of the target, coupled with a lack of signal in the upstream one, allowed us to infer that a charged particle had been created inside the  $LH_2$  cell by a neutron induced reaction. Particles interacting with the support structure to either side were excluded by position and angle cuts at the target which will be discussed in more detail in the next chapter and in appendix B. The scintillators inside the cold gas also eliminated these events because they were only 4 cm wide while the distance between the support walls was approximately 10 cm and the thickness of the  $LH_2$  along the beam direction was 6 cm. Particles scattering from the support wall which then passed through the downstream scintillator would therefore have had a scattering angle of at least  $30^\circ$  in the horizontal plane. This angle is well outside the nominal  $3^\circ$  acceptance of the MRS. Figure 3.6 shows the approximate position of the target support material, the area covered by the thin scintillators, and the maximum offset positions from which events were accepted in the offline analysis (for 360 MeV).

The observation of the light signals from the 0.01" scintillators presented some difficulties. As usual, the light was channeled to a phototube, but the position of the scintillators in the target region meant that lightpipes leading into the phototubes could not be attached directly to the thin edges of the scintillators. Further, the very high length to thickness ratio of these scintillators (200:1) would mean that only a very

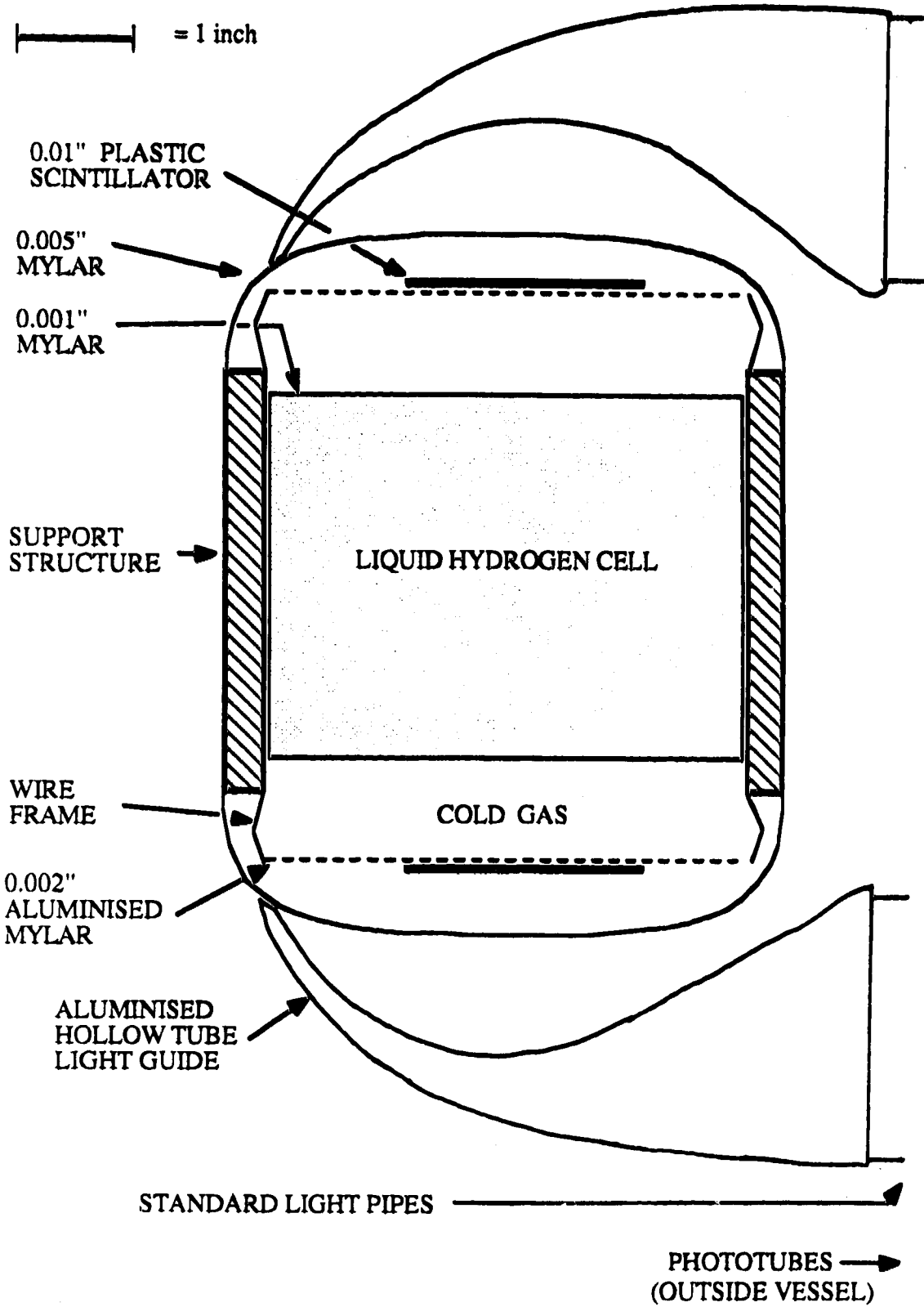


Figure 3.5 : The Liquid Hydrogen Target

## TARGET SUPPORT STRUCTURE POSITION

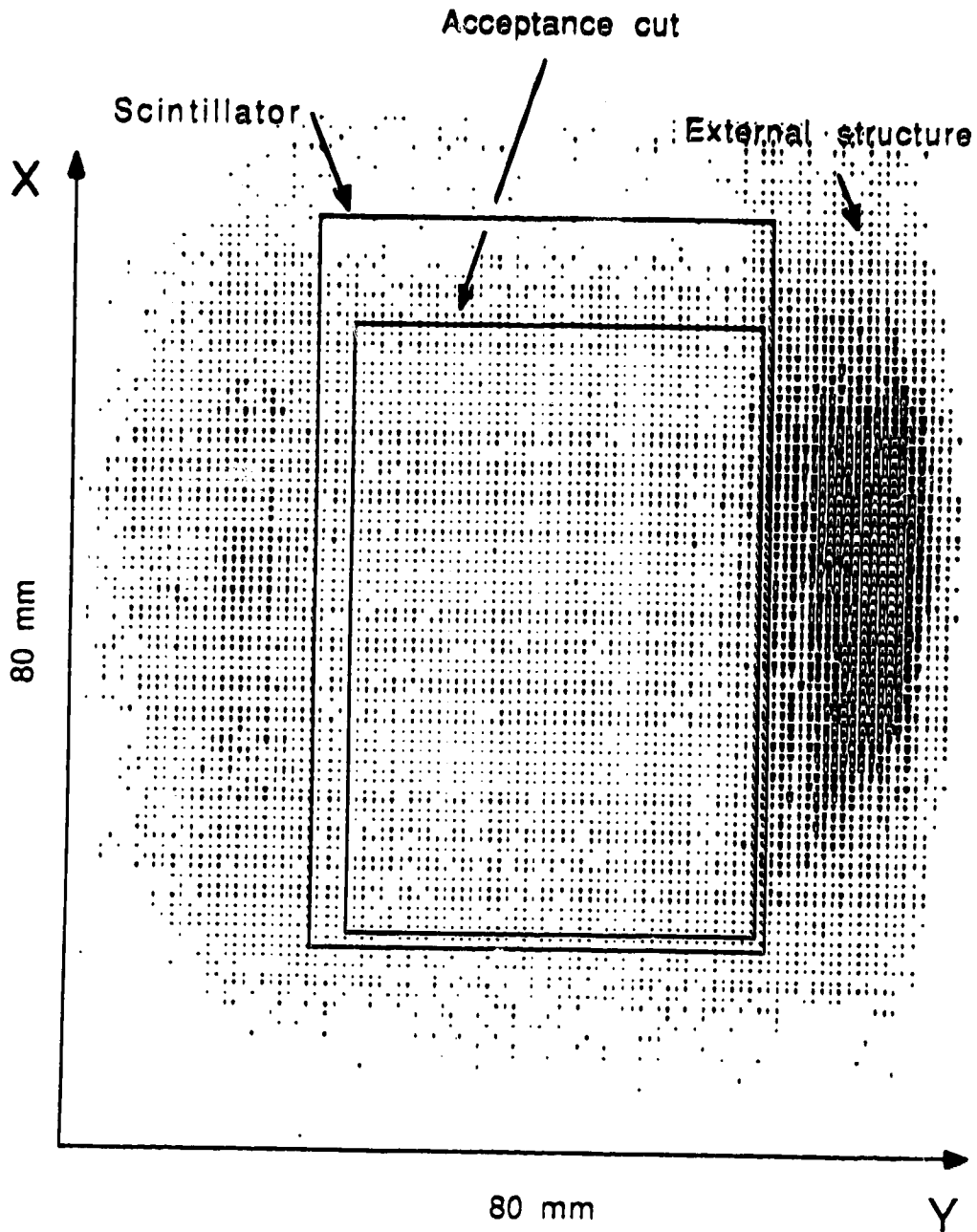


Figure 3.6 : This figure, with x being the bend plane target position and y being the non-bend plane target position, shows the approximate areas covered by the scintillator, and the offline acceptance cut, relative to the target support structure.

small amount of the available light would be transmitted to the end because of the small amount of available phase space and the many internal reflections which would be necessary. Accordingly, the light which exited the broad side of the scintillator was observed. After passing out of the cold gas region the light was collected by a channel constructed of aluminised mylar surfaces and directed into a conventional lightpipe which passed through a vacuum seal and into a phototube outside (as shown in figure 3.5).

A well known law of optics relating to lightguides is that when light is to be transmitted from a region with cross-section  $A_1$  to a region with cross-section  $A_2$ , then the maximum possible efficiency of transmission,  $\eta$  is given by

$$\eta = \frac{A_1}{A_2} \quad (A_2 \geq A_1). \quad (\text{III-1})$$

Since the phototubes were 1.625" in diameter, and light was being collected from from the entire area of the thin scintillator, an area of approximately 3.72 sq. in., a straightforward calculation indicates that the maximum light transmission would collect 56% of the available light. This necessitated a careful design of the periscope shape in order to ensure that enough light was collected to ensure a clean identification of the passage of a charged particle. The shape of our design is illustrated approximately in figure 3.5. In order to further increase the available light, the sides of the scintillators which faced the target were lightly sanded in order to create a specularly reflective surface. The object of this was to scatter photons which were emitted inside the scintillator at an angle greater than the critical angle for total internal reflection and would therefore be otherwise destined never to escape the scintillator sides. Appendix A gives a short description of an in situ test of this light collection system. The results were excellent, resulting in a clear and significant reduction of the deuteron background

when the information from these two scintillators was used. Figure 3.7 shows a focal plane spectrum with and without the cuts placed on the scintillators' energy spectra.

### III.2.3 Event definition

The electronics for this experiment were much the same as those used for most CHARGEEX experiments and form part of the 'standard' MRS facility. Differences included those counters associated with our liquid hydrogen target, and the fact that we included two FECs for track reconstruction at the entrance to the MRS. More detail on the MRS/ CHARGEEX electronics may be found in Ref. 32 and in the introductory paper on the CHARGEEX facility by R. Helmer<sup>(33)</sup>.

Electronics used with the MRS are mostly LeCroy CAMAC and NIM modules. Time to digital converters (TDCs), for arrival time, and analog to digital converters (ADCs), for pulse height, were used to interpret electric pulses from the phototubes attached to scintillators along the particle's flight path. Each scintillator signal was routed to a discriminator, which produced a logic pulse which was used to stop a corresponding TDC. All TDCs were started by the pulse from scintillator S1, assuming the MRS trigger condition (to be described shortly) was satisfied. Most of the TDCs were set on 100 ns full scale ranges which, with 11 bit resolution, theoretically provided 0.05 ns per TDC channel. This made the scintillator resolution of 1 ns or better, depending on thickness, the main component of our timing resolution. The distinguishing of protons from deuterons, a critical measurement, was straightforward since they had flight times through the spectrometer (about 11 m) which differed by 5-7 ns, depending on the energy.

The trigger logic is shown in fig. 3.8. Signals from the ADCs were shaped by discriminators and the resulting logic signals were analysed by NIM logic units. A combination of signals which corresponded to a 'good' event generated a pulse to start

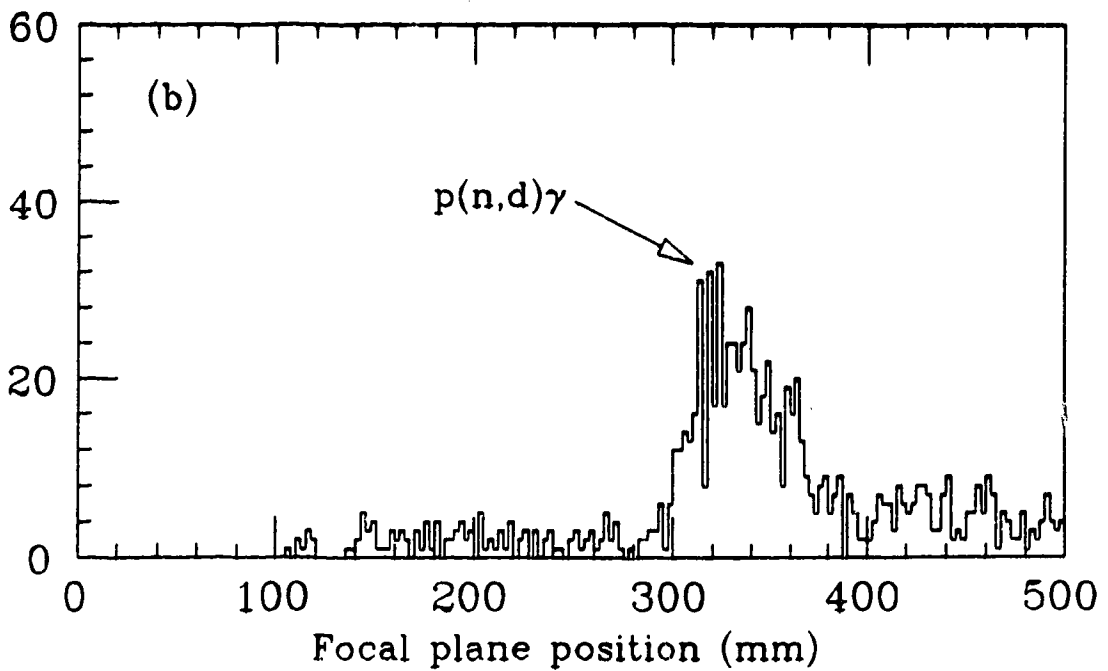
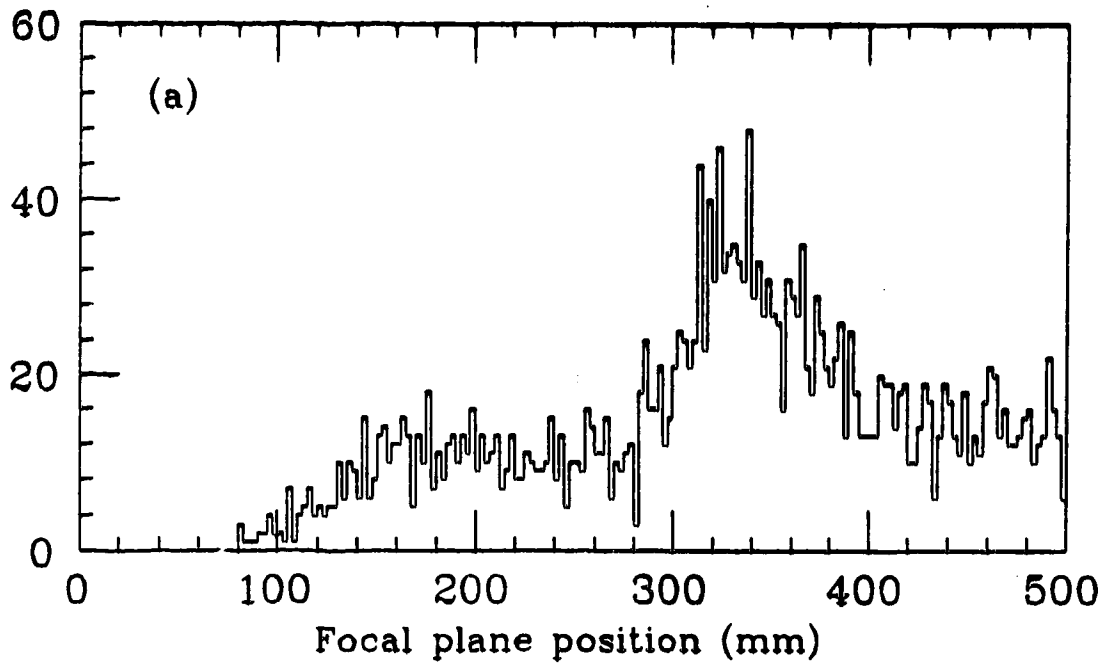


Figure 3.7 :  $^{12}\text{C}(n,d)\text{X}$  Background Suppression at 360 MeV.  
a) shows focal plane position before the information from the scintillators surrounding the  $\text{LH}_2$  was used, and b) shows the focal plane after cuts were applied to the energy spectra.

the corresponding TDCs (the stop signal, initiated by the passage of the charged particle, arrived later) and gate the ADC. After the CAMAC electronics had read an event, the ECLIPSE computer was notified by means of a CAMAC flag and the event was read, analysed in order to produce some online spectra, and written to magnetic tape at 1600 bpi. The trigger which was used as the definition of an event was

$$\text{PADDLES} \cdot \text{X1TR} \cdot \text{X0} \cdot \text{FPP1 (true)}$$

where

$$\text{PADDLES} = \text{PD0} + \text{PD1} + \text{PD2} + \text{PD3} + \text{PD4} + \text{PD5} + \text{PD6} + \text{PD7} + \text{PD8} + \text{PD9}$$

PD(0-9) = A signal above threshold in one of the large scintillator paddles located at the top end of the MRS.

X1TR = A good signal from the x plane of the first VDC at the exit of the MRS.

X0 = A good signal in the the x plane of FEC0 at the entrance to the MRS.

FPP1 = A timing signal from scintillator S1 of the MRS focal plane polarimeter.

• ≡ Logical AND

+ ≡ Logical OR

The MRS permits additional elements in its trigger which were not necessary for this experiment. The one exception is the front end scintillator (FES), which was occasionally included to make the trigger cleaner (more selective) by demanding an additional charged particle signal in the coincidence.





The ADCs and TDCs for each scintillator, as well as the TDCs attached to each wire of the VDCs and FECs, were read out via a CAMAC control system using a Data General ECLIPSE computer system running the data acquisition program DACS<sup>(34)</sup>. When the trigger condition was satisfied a latch was set blocking further ADC and TDC signals from arriving while the computer read and processed the information in the CAMAC modules. A quick hardware rejection of the event, by resetting this latch, was available based on time-of-flight through the spectrometer. Events arriving while the computer was busy processing an earlier event were ignored, and this was our main source of dead time. Dead time from this source was calculated as:  $1 - \text{PROCESSED} / (\text{TRIGGER} - \text{FC})$ , where PROCESSED and TRIGGER refer to the number of events written to tape and which satisfied the MRS trigger logic, respectively. FC is the number of events which were rejected by the hardware time-of-flight cut. TRIGGER, PROCESSED, and FC were all obtained by scalers attached to the logic units shown in figure 3.8. Dead times of 5 to 20% were typical, varying with beam current and energy.

Integrated beam charge was measured using the beam line polarimeter of the MRS. Scalers attached to polarimeter scintillators allowed us to calculate

$$Q_{\text{eff}} = N(E) \times [R + L - R_{\text{acc}} - L_{\text{acc}}]. \quad (\text{III-2})$$

$N(E)$  is the empirically known energy-dependent normalisation.  $R$ ,  $L$ ,  $R_{\text{acc}}$  and  $L_{\text{acc}}$  are the number of scatterings right and left together with the corresponding accidentals.

Off-line analysis was done on a VAX-780 using LISA. LISA is an interactive data analysis program particularly suited to reading data tapes produced by

DACS, and which has built-in subroutines for decoding MRS wire-chamber information. Details on the use of LISA as an analysis program may be found in the LISA documentation<sup>(35)</sup>.

### III.2.4 Experimental runs

Two different runs were made at each energy. During the first run, the MRS dipole and quadrupole fields were adjusted so that the  $p(n,d)\pi^0$  and  $p(n,d)\gamma$  deuterons were present together on the focal plane. In the second run the fields were adjusted so that the deuterons from the  $p(n,d)\pi^0$  reaction and protons from the  $p(n,p)n$  reaction were present simultaneously. This procedure allowed the double normalisation of  $p(n,d)\gamma$  to  $p(n,d)\pi^0$ , followed by  $p(n,d)\pi^0$  to  $p(n,p)n$  for calculation of the true  $p(n,d)\gamma$  cross-section using the formula

$$\frac{d\sigma}{d\Omega} [p(n,d)\gamma] = \frac{R[p(n,d)\gamma]}{R[p(n,d)\pi^0]_1} * \frac{R[p(n,d)\pi^0]_2}{R[p(n,p)n]} * \frac{d\sigma}{d\Omega} [p(n,d)n] . \quad (\text{III-3})$$

$R[\text{reaction}]$  = the observed rate of that reaction

This was done because the elastic scattering cross-section is well known from extensive phase shift analysis, and this procedure avoided some systematic errors associated with incomplete knowledge of the absolute efficiency of the spectrometer for protons and deuterons and each angle. Further, our cross-section results may be easily modified in the future, should any improvement in our knowledge of the np scattering cross-section become available.

Approximately 20% of our time was spent taking data with the target empty of liquid hydrogen in order to identify sources of background which could not be eliminated with the  $\text{LH}_2$  target scintillators discussed in section III.2.2 and appendix A.

## CHAPTER IV - DATA ANALYSIS (1)

### IV.1 PRELIMINARY REMARKS

As briefly mentioned in chapter III, the  $p(n,d)\gamma$  cross-sections were measured as follows. The spectrometer magnetic fields were first adjusted so that the momenta of deuterons from the reactions  $p(n,d)\gamma$  and  $p(n,d)\pi^0$  were both in the momentum range accepted by the spectrometer and the ratio of counts for the two peaks appearing on the focal plane was measured. The spectrometer fields were then lowered so that the protons from  $p(n,p)n$  were detected in the focal plane, and the  $p(n,d)\pi^0$  to  $p(n,p)n$  count ratio was measured. By this means the  $p(n,d)\gamma$  count rate was related to the relatively well known elastic scattering count rate and the need for precise absolute determination of the spectrometer acceptance, neutron beam intensity, and target characteristics was eliminated. The steps associated with such an analysis are these:

- 1) Analyse the time and energy spectra of the scintillators along the path through the spectrometer to select events which have the characteristics of either protons or deuterons.
- 2) Eliminate events with bad tracks through the spectrometer and check to ensure that the particle track originated within the  $LH_2$ , and not in the support structure or within upstream or downstream scintillator material.
- 3) For each region of the target, find the solid angle within which scattered particles were transmitted through the spectrometer to all regions of the focal plane with uniform probability. This acceptance will be discussed in detail in appendix B.
- 4) Correct the particle momenta for the spectrometer characteristics, then correct the momentum for the kinematic change due to scattering at a

finite angle (up to  $3^\circ$ ) instead of the ideal  $0^\circ$ .

- 5) Numerical calculations based on fitting the momentum peaks produced by steps 1 through 5 to produce the final cross-section numbers. This involved: a) fitting the peaks to analytic functions, b) estimating corrections to the number of events in each peak using the fits, and c) putting in the various kinematic elements of the cross-section.

Steps 1 through 4 will be reviewed in this chapter. Step 5 will be done in chapter V.

## IV.2 INITIAL EVENT SELECTION

In experiments where more than one distinct particle type is present, one usually distinguishes among particle groups by measuring for each particle any two of the following parameters:  $E$ , the total energy,  $\Delta E$ , the fractional amount of energy deposited in a thin scintillator, and TOF, the flight time over a known distance. In this experiment, particle identification was made by measuring the energy deposited in the scintillator paddles (PD0 to PD9) and also the TOF between these paddles and the front end scintillator (FES) at the entrance to the MRS. The TOF measurement is clearly a function of the the velocity of the particle only. The energy loss measurement is less clear but an examination of the Bethe-Bloch equation<sup>(36)</sup> for the rate of energy loss of a charged particle passing through matter shows that, in a good approximation,

$$\frac{dE}{dx} \propto \frac{z^2}{v^2}. \quad (\text{IV-1})$$

$z$  is the charge of the particle and  $v$  is its velocity. Clearly  $dE/dx$  is also, in this approximation, a function of velocity only. A 2-dimensional plot of  $\Delta E$  vs. TOF, called SPID, will have different particles lying at different points along the parabola  $\Delta E = z^2 \text{TOF}^2$  depending on their velocity. Because of the spatial restrictions set by the MRS magnets, particles moving along a circular arc must all undergo approximately the same degree of bending so that the MRS trigger, a correlated signal of scintillators at the top and bottom of the MRS, defines a fairly narrow window in momentum. This means that accepted protons will have significantly different velocities than accepted deuterons, which have twice the mass, and a clean separation of these two particle groups is possible. Figure 4.1 is an example of this at 360 MeV neutron energy,

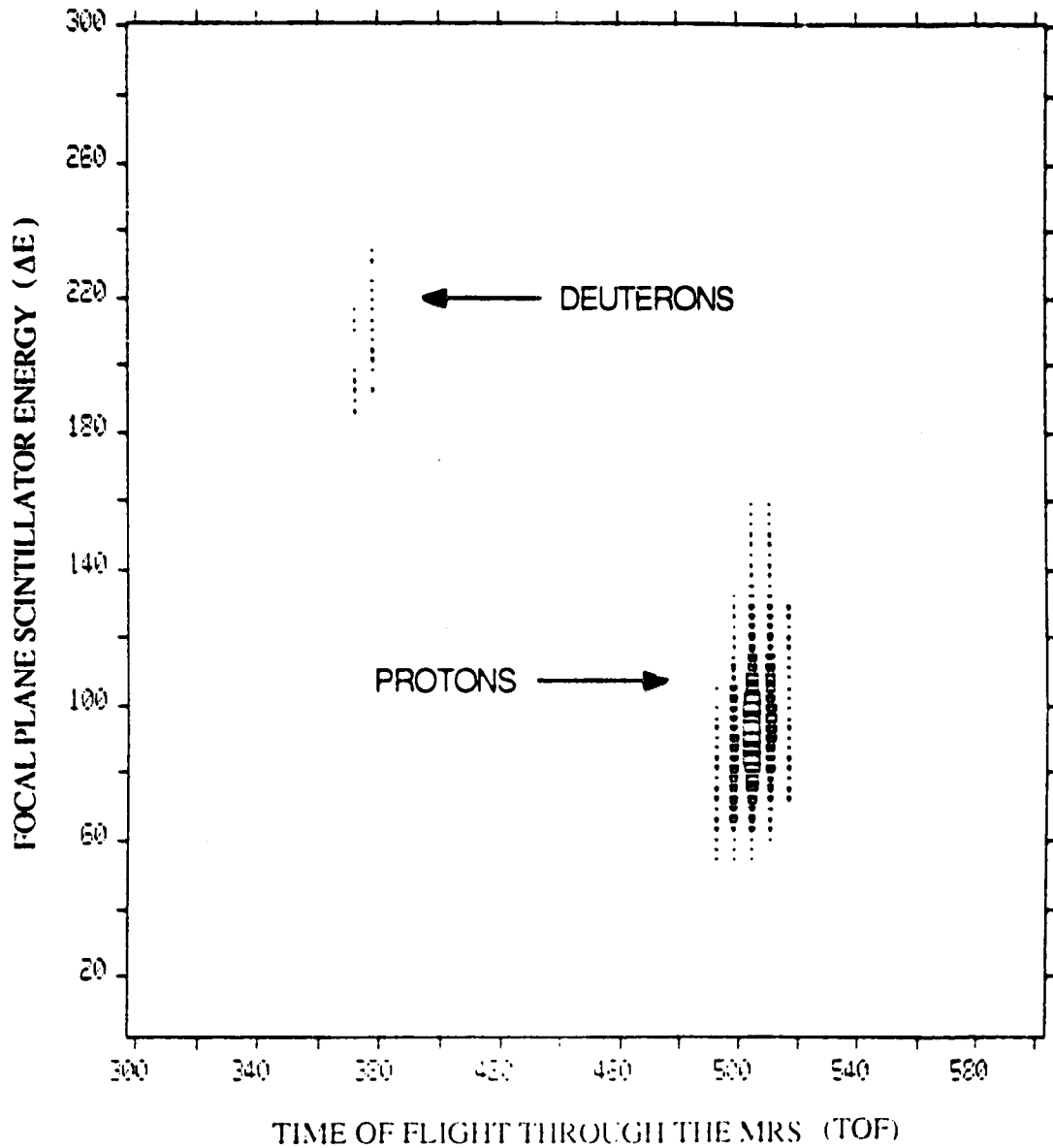


Figure 4.1 : The Spectrum for Particle Identification (SPID). This spectrum is used for the initial cut separating protons from deuterons.

showing the position of the protons from  $p(n,p)n$  and the deuterons from the  $p(n,d)\gamma$  and  $p(n,d)\pi^0$ , which are too closely spaced in momentum to be separated here. In practice, the TOF provided a clean separation between deuterons and protons, while  $\Delta E$  was useful for identifying events which were the result of the accidental pairing of a proton or deuteron triggering the start scintillator, but which did not pass through the spectrometer, with the later arrival at the MRS paddles of a low energy particle from the room background.

After initial skimming to select events which fell within a generously defined region of the  $\Delta E$ /TOF plane associated with deuterons (high deposited energy, long time-of-flight) or protons (low deposited energy, short time-of-flight), the information from various scintillators along the particle's track was examined to ensure that the event exhibited characteristics consistent with the choice of particle group. Scintillators on the particle's trajectory through the spectrometer were required to show deposited energies consistent with the particle in question. A 'pedestal' reading was required of scintillators which should not have been along the particle's track. The pedestal channel of an ADC is the one corresponding to the integration of the adjustable bias voltage on the ADC and the photo-multiplier tube 'dark current', which are the only signals present if no particle passes through the scintillator. In all, in order to pass this section of tests, events were required to have appropriate energies in: the scintillator at the entrance to the MRS (FES), scintillators S1 and S2 at the exit the to the MRS, at least one of the focal plane paddles (PD0 to PD9), pedestals in the initial veto scintillator (VET) and in each of two scintillators defining the entrance of the MRS magnet (DIP and SLT). The relative positions of these scintillators in the MRS are illustrated in figure 3.2 of the previous chapter. The energy spectra from S1, FES and VET for the raw data and as they appear after cuts on scintillator times and energies, are shown in figures 4.2a to 4.2c (deuterons) and 4.3a to 4.3c (protons).



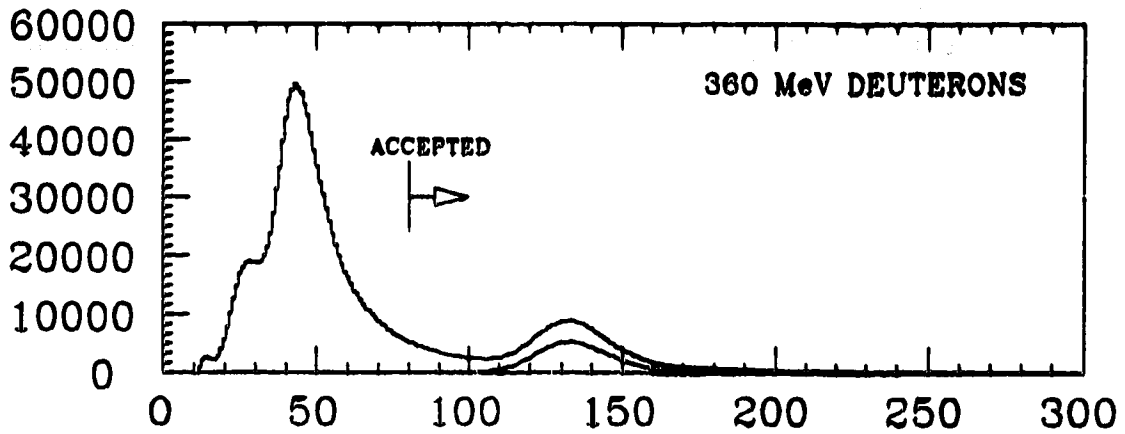


Fig. 4.2a : S1 Energy Spectrum. The top spectrum is the raw data. The bottom shows the effect of the time/energy cuts.

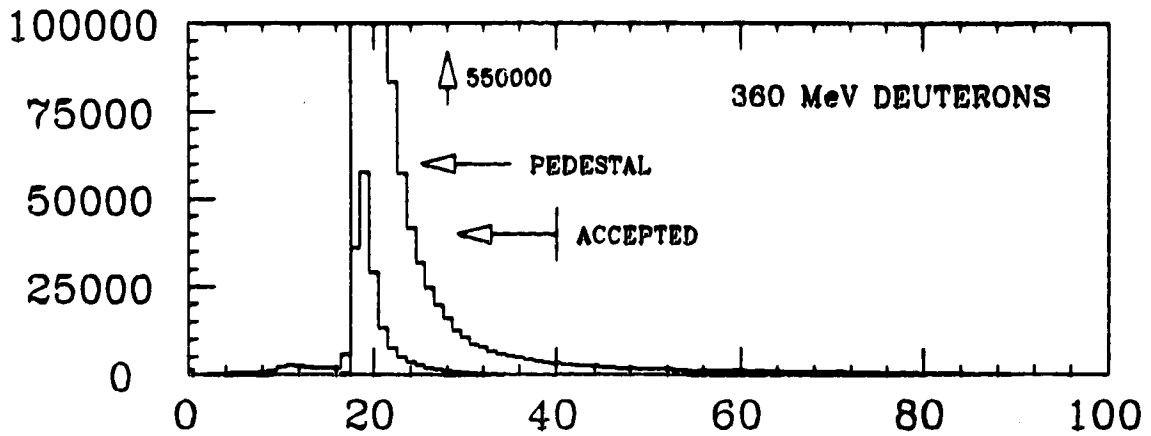


Fig. 4.2b : VET Energy Spectrum. The top spectrum is the raw data. The bottom shows the effect of the time/energy cuts.

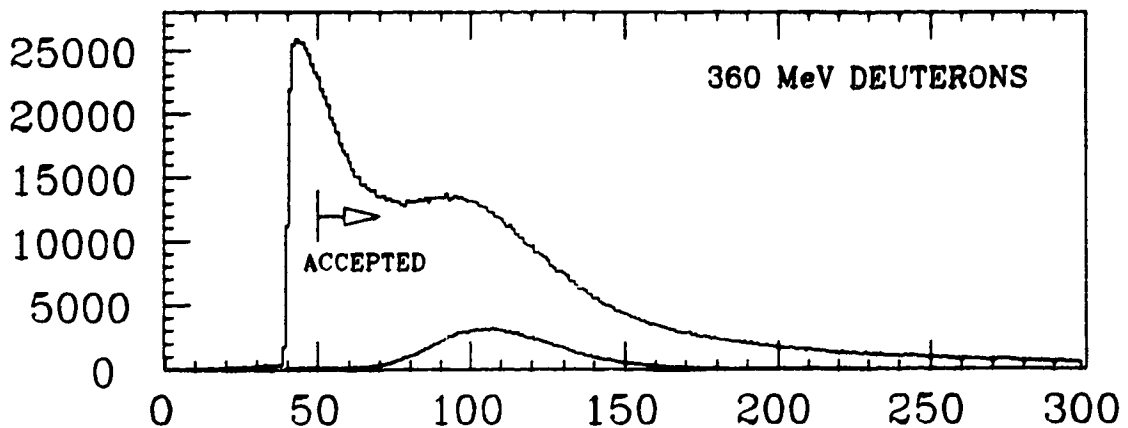


Fig. 4.2c : FES Energy Spectrum. The top spectrum is the raw data. The bottom shows the effect of the time/energy cuts.

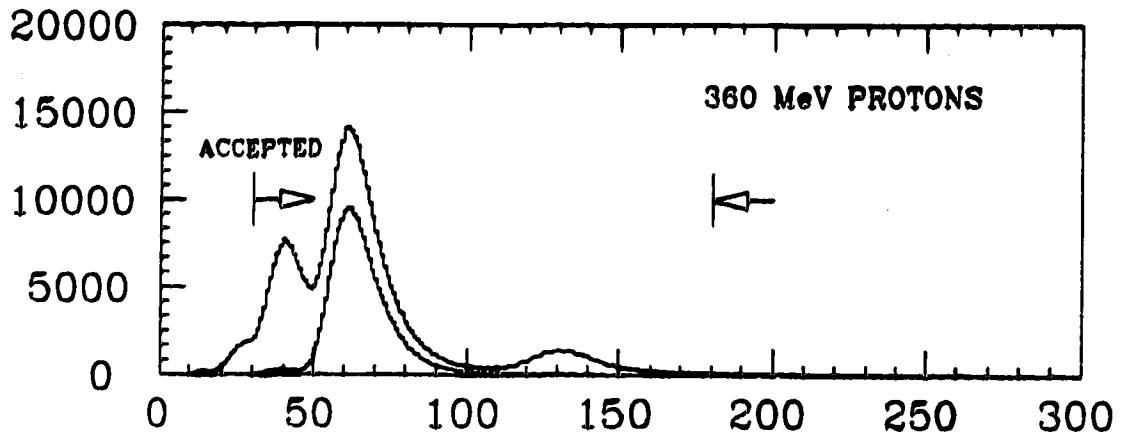


Fig. 4.3a : S1 Energy Spectrum. The top spectrum is the raw data. The bottom shows the effect of the time/energy cuts.

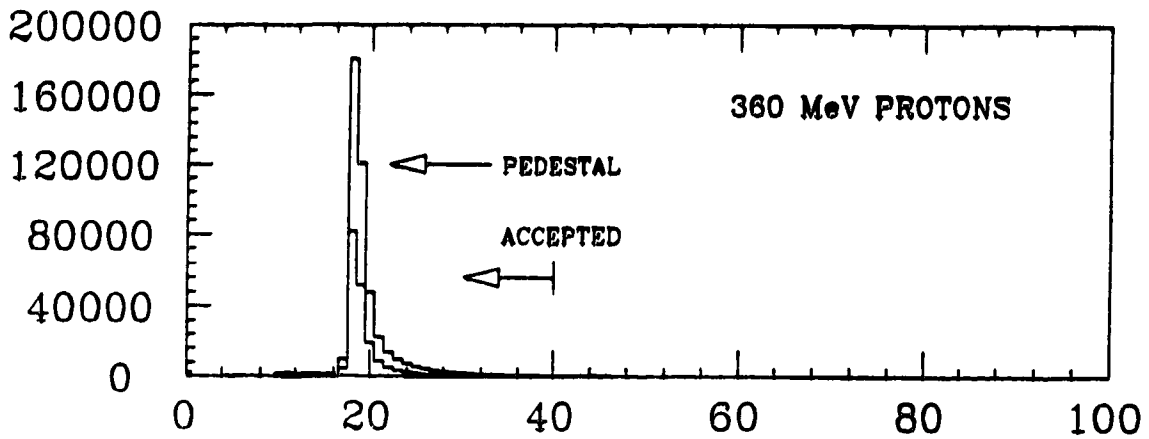


Fig. 4.3b : VET Energy Spectrum. The top spectrum is the raw data. The bottom shows the effect of the time/energy cuts.

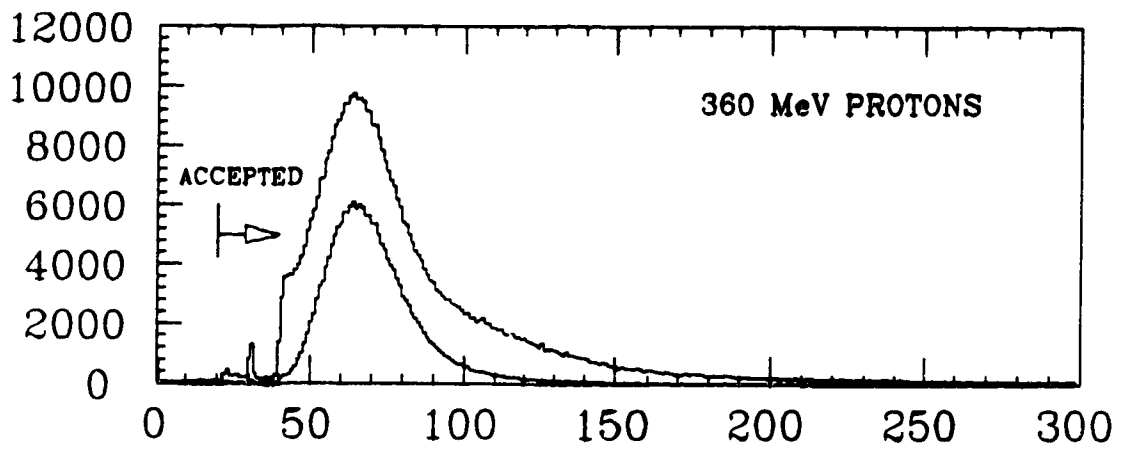


Fig. 4.3c : FES Energy Spectrum. The top spectrum is the raw data. The bottom shows the effect of the time/energy cuts.

Good time information was also required from the FES, scintillator S1 and from the veto scintillator VET. For this last scintillator a good time signal meant the presence of a time-out in its associated TDC, since a time signal was necessarily absent for a good event (note the gap in the scintillator time spectra 4.4b and 4.5b). However, since a typical flight time through the spectrometer ( $\sim 30$  ns) was much shorter than the 500 ns full scale range of the TDC for this scintillator, the time spectrum showed a periodic structure associated with the 43 ns beam burst interval. Accidental coincidences associated with later beam bursts were permitted to pass the cut along with the time-outs. Events where there was associated an early signal in the veto scintillator were thrown out. Figures 4.4a to 4.4c and figures 4.5a to 4.5c show the time signals from the S1, FES and VET corresponding to the energy spectra in figures 4.2 and 4.3.

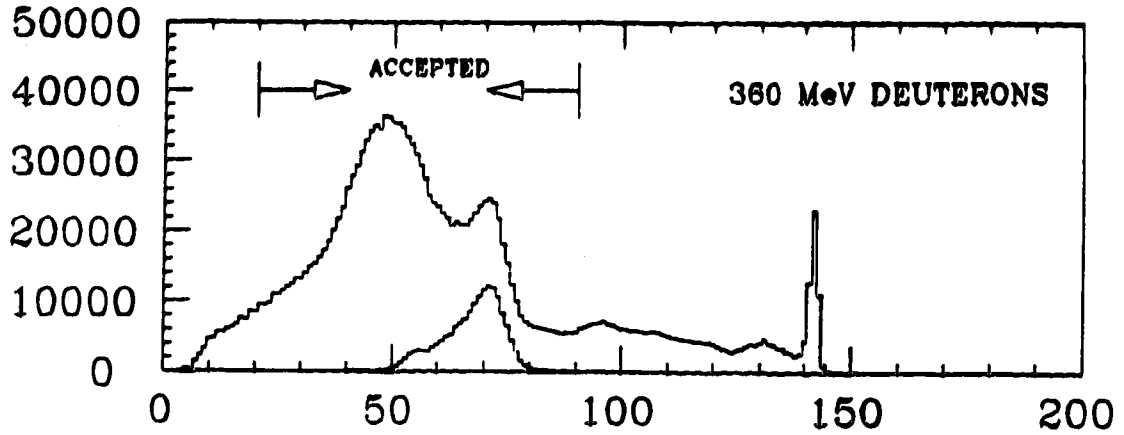


Fig. 4.4a : S1 Time Spectrum. The top spectrum is the raw data. The bottom shows the effect of the time/energy cuts.

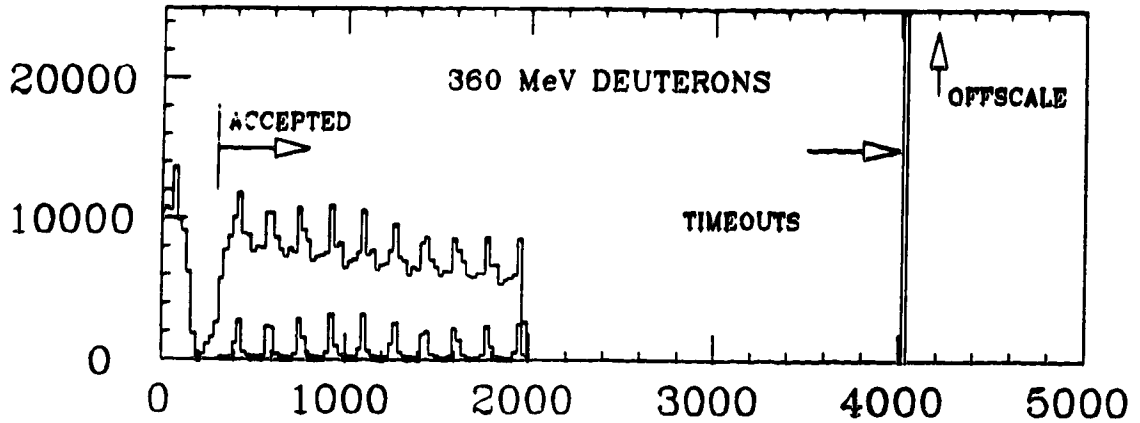


Fig. 4.4b : VET Time Spectrum. The top spectrum is the raw data. The bottom shows the effect of the time/energy cuts.

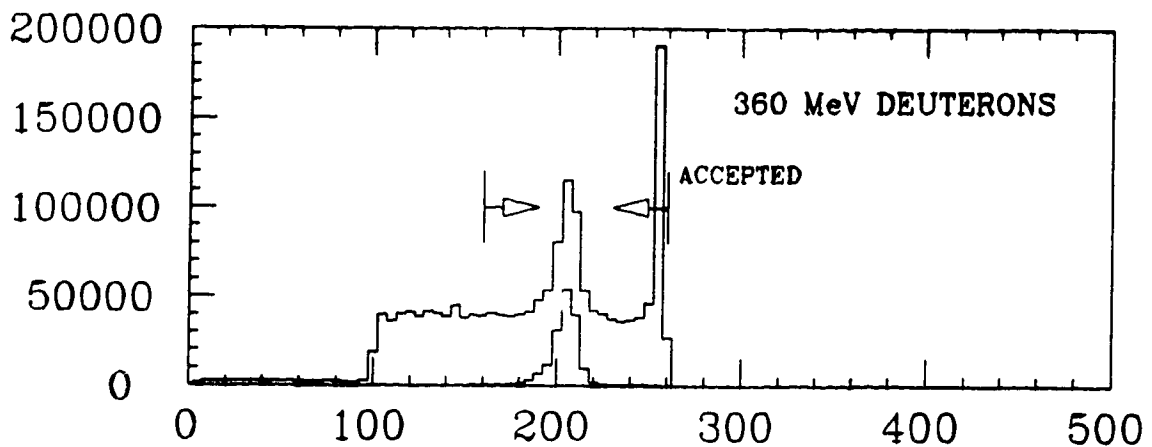


Fig. 4.4c : FES Time Spectrum. The top spectrum is the raw data. The bottom shows the effect of the time/energy cuts.

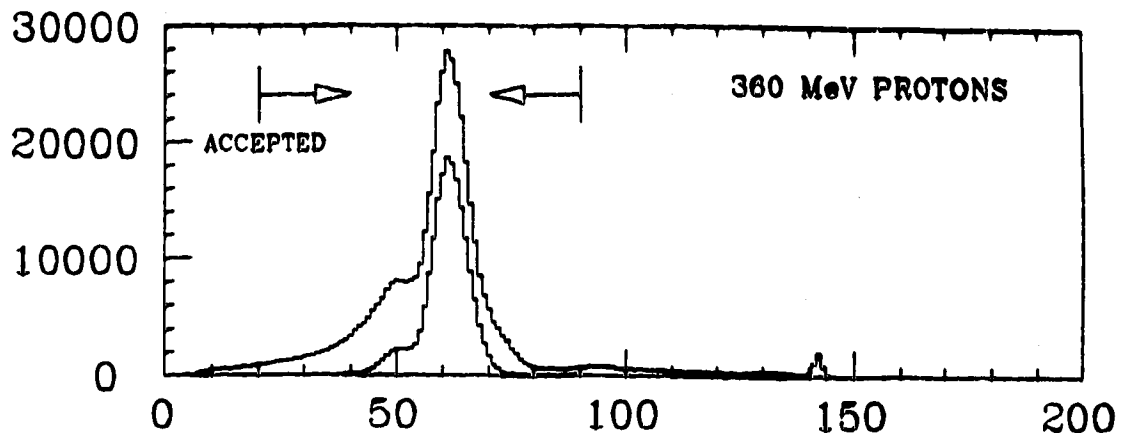


Fig. 4.5a : S1 Time Spectrum. The top spectrum is the raw data. The bottom shows the effect of the time/energy cuts.

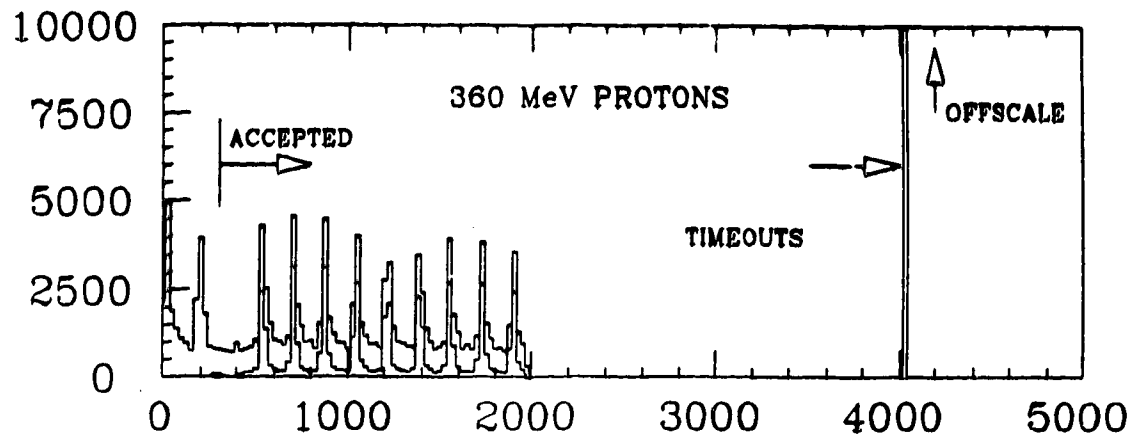


Fig. 4.5b : VET Time Spectrum. The top spectrum is the raw data. The bottom shows the effect of the time/energy cuts.

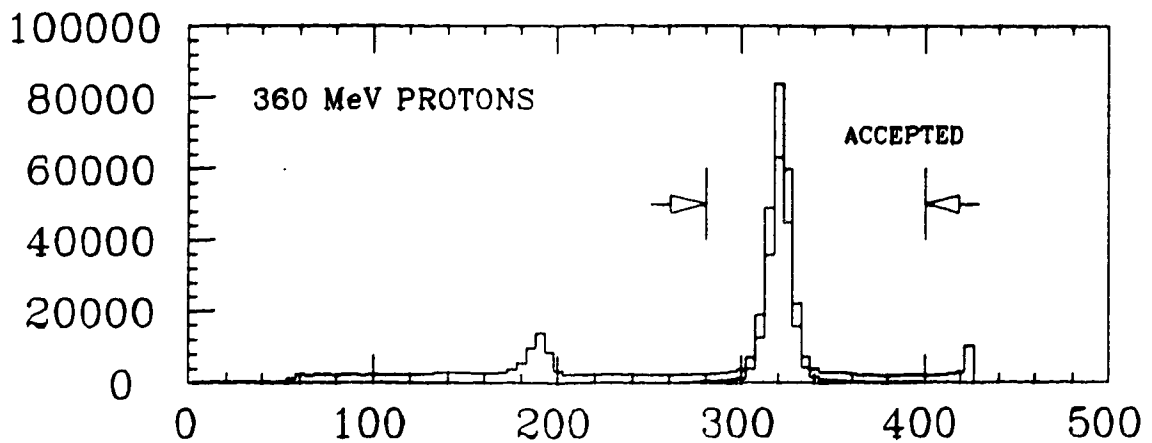


Fig. 4.5c : FES Time Spectrum. The top spectrum is the raw data. The bottom shows the effect of the time/energy cuts.

### IV.3 SPECTROMETER CHARACTERISTICS

The characteristics of the spectrometer system cause a variation of focal plane position amongst a group of particles with identical momenta but different spectrometer entrance parameters. Besides imperfections and non-linearities in the magnet optics, variations in the focal plane position for the MRS/CHARGEEX system appear in two principle ways:

- 1) as a variation in focal plane position ( $XF$ ) with  $\theta_{pc}$ , the angle, in the bend plane, of the particle track with respect to the VDCs at the exit of the MRS, and
- 2) as a variation in focal plane position with  $XI$ , the vertical displacement of the particle track at the liquid hydrogen target.

The first source of focal plane variations has its source in a displacement of the true focal plane from its estimated position along the beam path. Focal plane position is calculated as (see fig. 4.6)

$$XF = \frac{[G(X1+H) - F(X1+H-X2)]}{[G - (X1+H-X2)\tan\delta]} \quad (IV-2)$$

$\delta$  is quite small and may be neglected.  $\theta_{pc} \equiv (X1+H-X2)/G$  for small deviations from  $45^\circ$ .  $F$  is a constant which defines the MRS focal plane position relative to the wire planes in the two VDCs. Errors in  $F$  show up as a variation in the calculated position  $XF$  with  $\theta_{pc}$  via the relation  $\Delta XF = \Delta F \theta_{pc}$ .

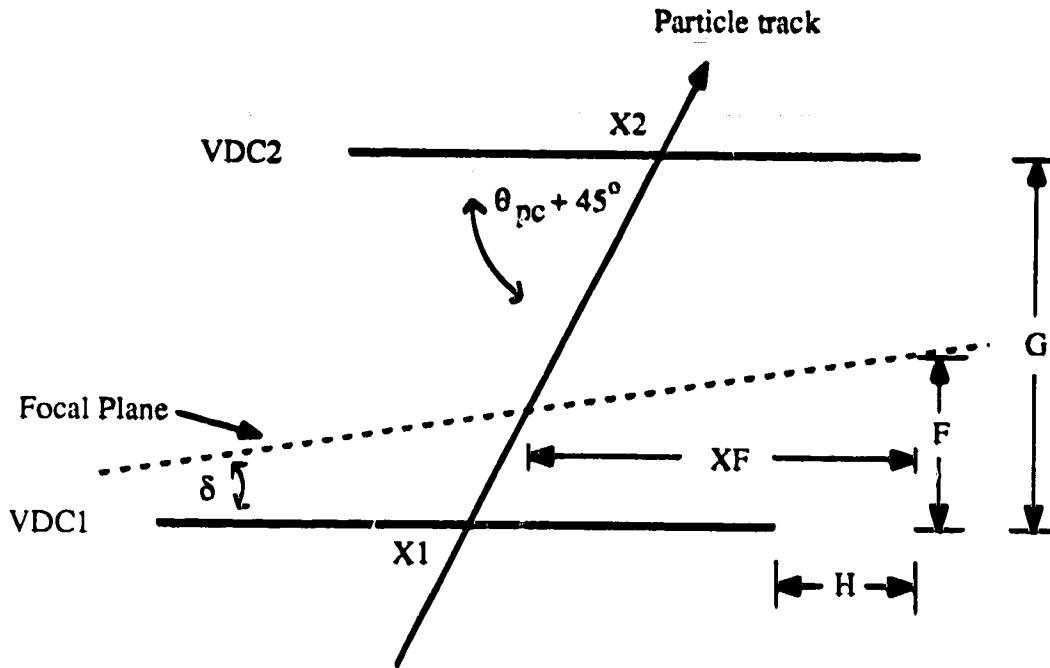


Figure 4.6 : The Geometry of the MRS Focal Plane

The optical properties of the MRS dipole/quadrupole combination give rise to the second source of variation of focal plane position for particles of equal momenta. The MRS quadrupole acts only to focus the rays diverging in the non-bend plane into the dipole magnet gap (while actually causing the bend plane rays to diverge), but the dipole focuses in the bend plane by means of a technique known as 'edge focusing'. Edge focusing is achieved by angling the exit and exit edges of the dipole magnets to create different path lengths, and therefore different degrees of bending, for particles entering the dipole at different points (see fig. 3.7). This lens action of the dipole gives the system an overall magnification, or variation of  $XF$  with  $XI$  (bend plane offset at the  $LH_2$  target), of 0.5.

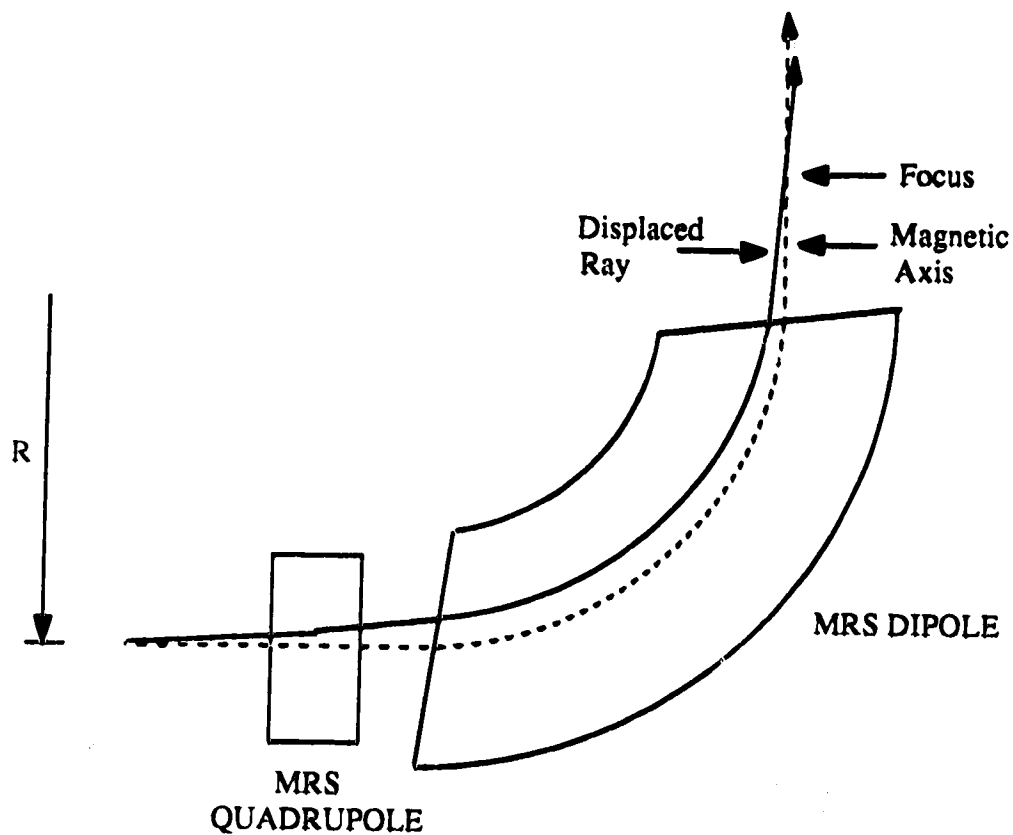


Figure 4.7 : Edge Focusing with the MRS Dipole Magnet. The MRS dipole magnet acts as a simple lens in the bend plane with a magnification of  $-0.5$ .

Both effects were corrected empirically by plotting 2D histograms,  $\theta_{pc}$  vs.  $X_F$  and  $X_I$  vs.  $X_F$ , and adjusting the observed focal plane position in such a way that the corrected  $X_F$  ( called  $X_{FK}$ ) was independent of  $\theta_{pc}$  and  $X_I$ . Linear and quadratic corrections were made, although the quadratic corrections were relatively small.

No significant variation of focal plane position with the non-bend plane coordinate,  $Y_I$ , was observed when  $Y_I$  was plotted versus  $X_{FK}$ .

The final corrections made to particle momentum, as defined by the focal plane position, were kinematic ones. Since the component of momentum which is



perpendicular to the bend plane is not measured, non-zero scattering angles within the LH<sub>2</sub> target lead to a certain amount of kinematic spreading of the peaks. Correcting for this effect has the effect of better defining the reaction peaks, so that subsequent peak fitting, and background subtraction, is more accurate. The momentum difference between a particle scattered at 0° relative to the MRS entrance, and one scattered at an angle PFEC perpendicular to the bend plane is

$$\Delta P = \left[ \left\{ \frac{1}{\cos(\text{PFEC})} - 1 \right\} P + \Delta P_{\text{REACT}} \right] \quad (\text{IV-3})$$

$\Delta P_{\text{REACT}}$  is the real momentum difference of the particle due to its non-zero scattering angle within the LH<sub>2</sub>, and the first term represents the apparent momentum change of the particle because of the existence of an unmeasured component of its momentum. A change in the focal plane position is linear in the quantity  $\Delta P/P$ , with the constant of proportionality being a function of the dipole/quadrupole field strength

$$d(\text{XFK}) = \frac{dP}{P} C(\text{B}). \quad (\text{IV-4})$$

We can integrate IV-5 to produce an expression for XFK.

$$\text{XFK} = C(\text{B}) \ln(P) + \text{XFK}_0(\text{B}). \quad (\text{IV-5})$$

IV-5 may be inverted in order to extract the true momentum, P. The correction  $\Delta P$  may then be added to correct for the normal momentum dispersion which was due to finite scattering angles.

$$P = \exp\left[\frac{(XFK - XFK_0)}{C}\right] + \Delta P. \quad (\text{IV-6})$$

Calculation of the kinematics of the  $p(n,d)\gamma$ ,  $p(n,d)\pi^0$ , and  $p(n,p)n$  reactions were encoded as FORTRAN subroutines and called from the main analysis program. The code is included in this dissertation in appendix C

## IV.4 FINAL EVENT SELECTION

Four final criteria were applied to the data set in order to define good events. These were:

- 1) A requirement that the event's MRS entrance co-ordinates (target X and Y offset at the target position and the MRS entrance angles in the XZ plane and XY plane) fall within a specific region of the MRS acceptance.
- 2) The rejection of events with large MRS exit angles ( $\theta_{pc}$ ) relative to the MRS magnetic (optic) axis.
- 3) The rejection of events whose Y co-ordinate at the exit of the MRS is not correctly related to their initial Y position and YZ entrance angle.
- 4) The imposition of cuts on the energy spectra of the scintillators inside the LH<sub>2</sub> target in order to include only those particles which were created inside the LH<sub>2</sub> target.

We discuss each of these in a separate section below.

### IV.4.1 MRS acceptance restriction

Since normalisation between reactions with different final state momenta was carried out, the allowed co-ordinates of particles entering the MRS (horizontal and vertical displacements and angles) were restricted during the offline analysis to a subset which had equal probability of passing through the spectrometer regardless of initial momentum. The determination of this acceptance 4-volume is detailed in appendix B. This restriction removed particles near the edges of the MRS acceptance which were subject to fringe magnetic fields and to scattering from pieces of experimental apparatus. This restriction to a central region of the MRS acceptance was necessary in

order to be confident about the relative normalisation of peaks produced at different points on the MRS focal plane.

#### IV.4.2 Restriction of MRS exit angles in the bend plane

Events with large exit angles relative to the magnetic axis tend to leave the MRS dipole magnet in a region of fringing fields, and are therefore subject to less bending than central particles. This effect creates a high momentum tail which is correlated with large absolute exit angles. (see figure 4.8). The range of allowed  $\theta_{pc}$  angles was therefore restricted offline. This cut was made after the MRS acceptance at the front end had been restricted. In order to reduce or eliminate the possibility of creating a bias for one side of the focal plane,  $\theta_{pc}$  was adjusted so that it was momentum independent.

$$\theta_{pc} \rightarrow \alpha XF + \theta_{pc}. \quad (\text{IV-7})$$

#### IV.4.3 MRS track reconstruction

At the focal plane, the particle's position in the co-ordinate perpendicular to the MRS bend plane (YF) should be a function of the particle's initial co-ordinates YI, PFEC (the angle perpendicular to the bend plane), and the particle's initial momentum. Assuming an approximately linear response of the quadrupole to changes in YI and PFEC, we can write

$$YF = \alpha(p) YI + \beta(p) PFEC + YF_{\text{offset}}. \quad (\text{IV-8})$$

The coefficients  $\alpha$  and  $\beta$  can be found for a particular momentum by plotting YI vs. YF and PFEC vs. YF. The focal plane position YF may then be reconstructed for

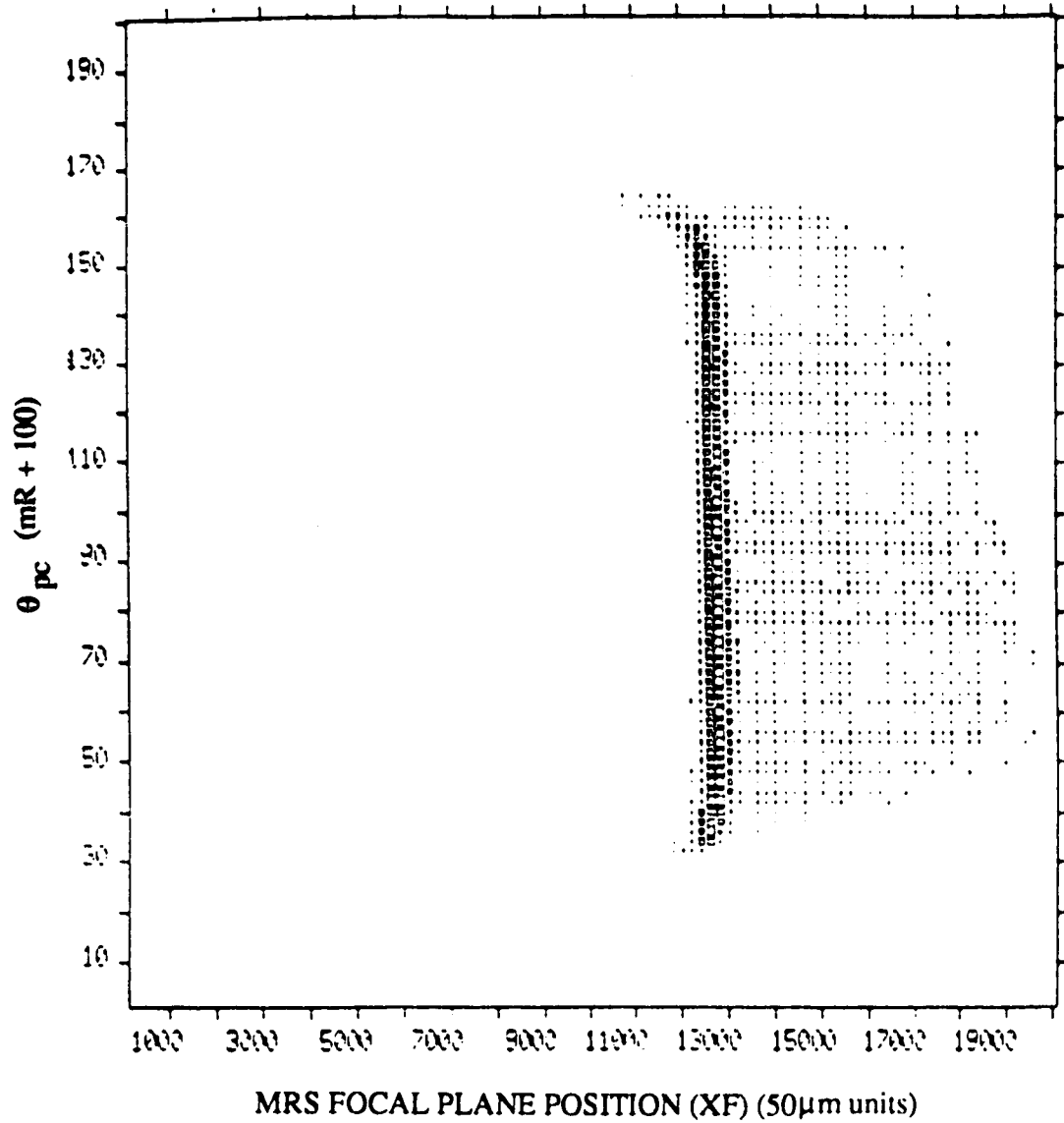


Figure 4.8 : Focal Plane Position vs. MRS Exit Angle. A linear and quadratic change was made to the focal plane position in order to make XF independent of  $\theta_{pc}$ . This figure shows the plot after the correction was made to focal plane position.

individual events, and the difference  $\Delta Y$  between the predicted and actual focal plane position computed

$$\Delta Y = YF - \alpha(p)YI - \beta(p)PFEC - YF_{\text{offset}}. \quad (\text{IV-9})$$

A restriction on the allowed variation of  $\Delta Y$  suppresses events which undergo scattering inside the MRS. Figure 4.9 shows a typical  $\Delta Y$  spectrum. Our cuts were quite generous here, since the number of events involved was relatively small.

#### IV.4.4 Restriction to particles created within the LH<sub>2</sub> target

As explained in detail in chapter III, two thin scintillators were placed in the vacuum vessel surrounding the LH<sub>2</sub> target. One was placed just upstream, the other just downstream of the liquid hydrogen. By requiring a charged particle signal in the downstream scintillator after the target in conjunction with the absence of such a signal in the upstream scintillator, events which produced charged particles by means of neutron interactions in the material surrounding the target cell could largely be eliminated. This was quite important for suppressing the relatively flat background around the p(n,d) $\gamma$  peak, as shown in figure 3.7. Typically 20% of all p(n,d) $\gamma$  events were rejected via this cut after all other cuts had been applied (figure 3.7). Figure 4.10 shows the spectra of these scintillators for events passing all the other restrictions detailed in this chapter. The information from these two scintillators was not used for the p(n,p)n vs. p(n,d) $\pi^0$  normalisation run because the low deposited energy of the protons made a clean cut impossible.

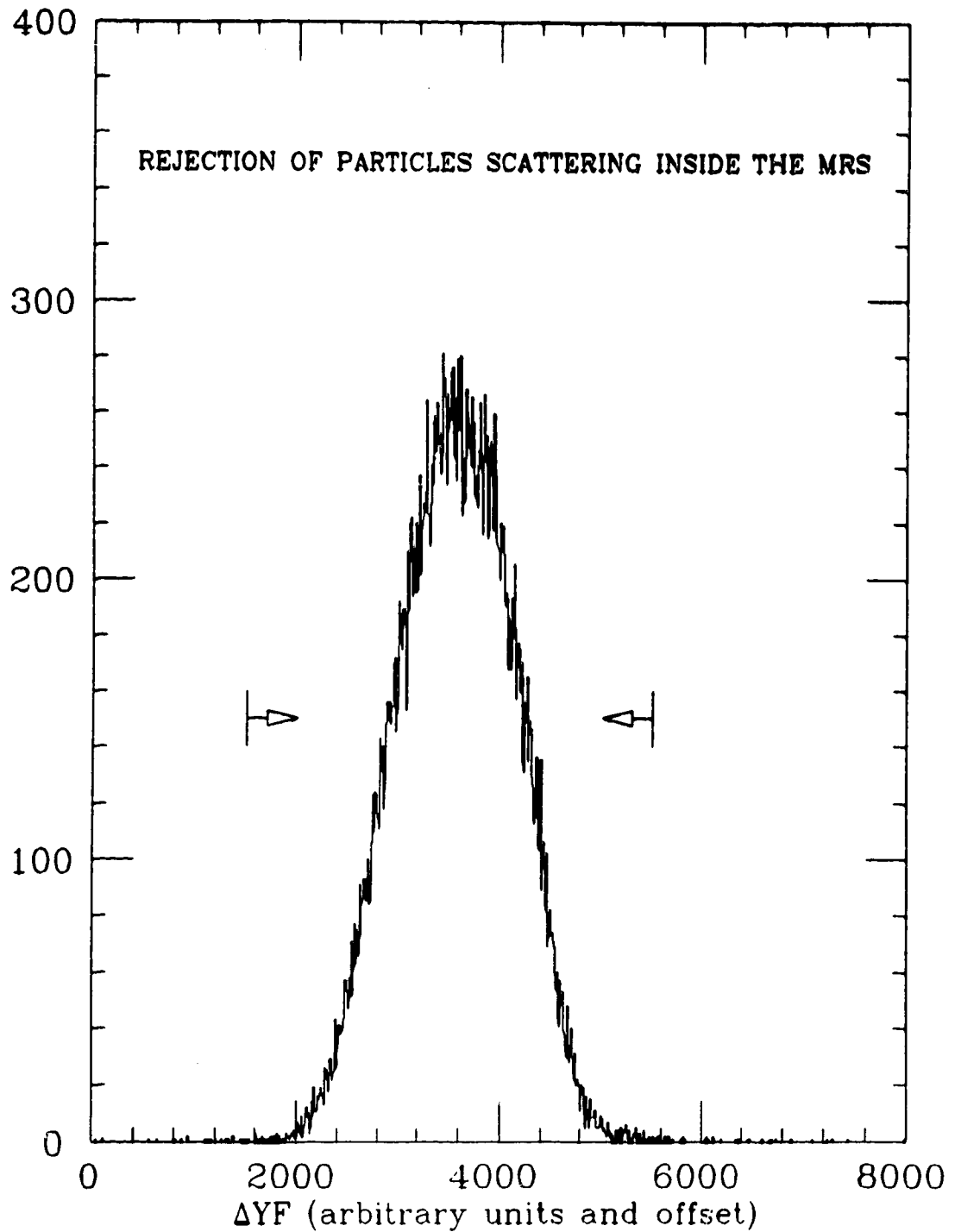


FIG 4.9 : The difference between the actual and projected non-bend plane position at the focal plane. The indicated limits suppress events which have undergone scattering inside the MRS magnets.

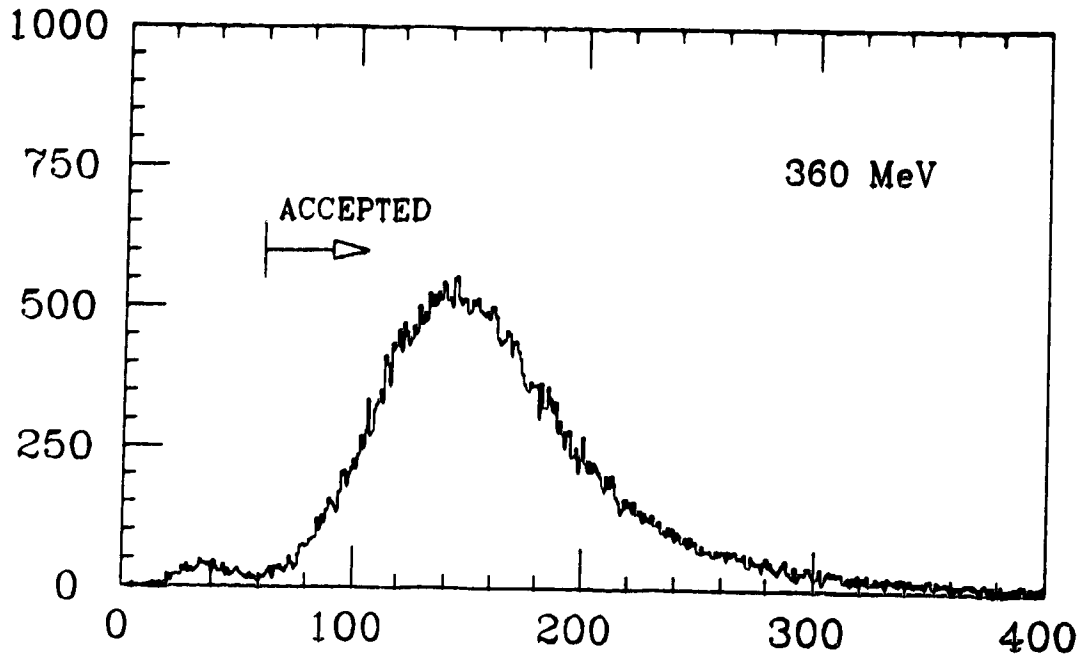


Figure 4.10a : The Energy Spectrum of the Thin Scintillator Downstream of the LH<sub>2</sub>. The indicated cut reduced the level of background under the p(n,d) $\gamma$  peak.

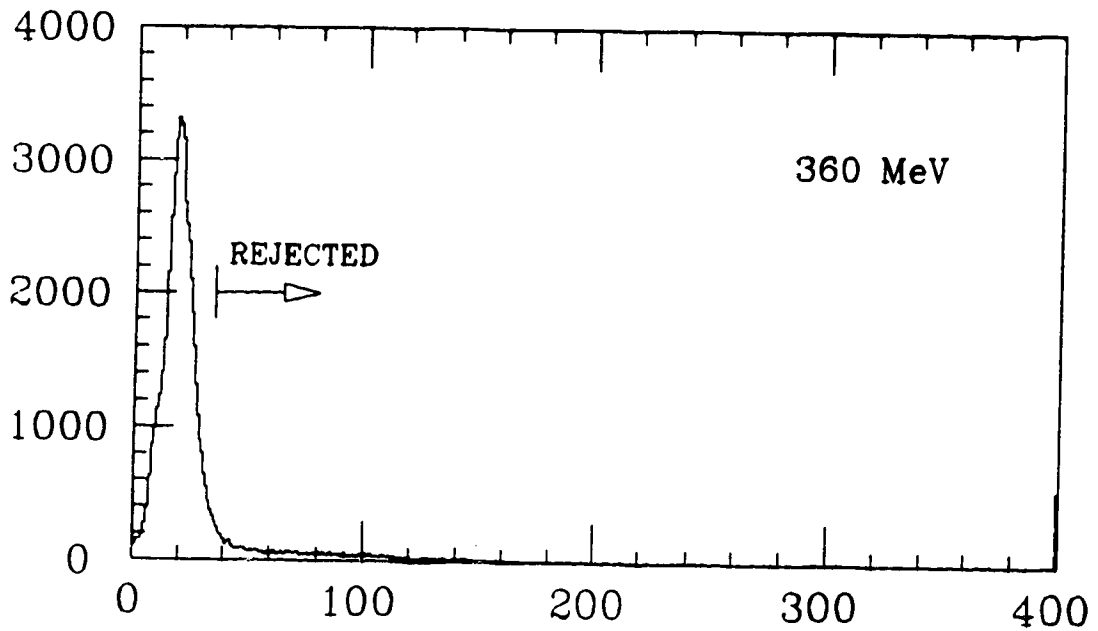


Figure 4.10b : The Energy Spectrum of the Thin Scintillator Upstream of the LH<sub>2</sub>. The indicated cut reduced the level of background under the p(n,d) $\gamma$  peak.



## CHAPTER V DATA ANALYSIS (2)

### V.1 FITTING THE REACTION PEAKS (THEORY)

The final stage of the analysis concerns the extraction of relative reaction rates from the  $p(n,d)\gamma$ ,  $p(n,d)\pi^0$  and  $p(n,p)n$  momentum peaks. The first step of this procedure was to fit the various reaction peaks to analytic functions. A model of the neutron energy distribution was necessary for this procedure because of the existence of a long low energy tail. The range of energy loss in the LH<sub>2</sub>, depending on the interaction point, meant that protons and deuterons produced by neutrons in the high energy edge of this tail interacting downstream could have the same momentum as protons or deuterons produced on the upstream side of the LH<sub>2</sub> by the main neutron peak. The differing size of this effect for protons and deuterons was effectively accommodated by deconvoluting the rectangular energy-loss distribution and the intrinsic spectrometer response function, which is defined as the lineshape produced by a neutron delta function peak in the absence of any energy losses for the reaction products. Because of the mathematical difficulties and uncertainties of doing this directly, an approximate deconvolution was done by the procedure to be outlined below. The result of the deconvolution gave us the neutron energy spectrum, and the parameters of the deconvolution defined the response function  $MRS(\Delta p)$ , which is defined as the combination of the LH<sub>2</sub> energy loss and the intrinsic spectrometer response. The convolution of the low energy neutron tail with  $MRS(\Delta p)$  then provided the number of events underlying the main peak.

In practice,  $MRS(\Delta p)$  is not a single peaked function, since a secondary peak due to (n,p) or (n,d) reactions appears at a Q value of approximately -12.5 MeV. It was found most convenient, however, for purposes of analysis, to assume that  $MRS(\Delta p)$  had

only one peak and to include the secondary peak by assuming that the underlying neutron spectrum had a second delta function approximately 12 MeV below the delta function corresponding to the  ${}^7\text{Li}(n,p){}^7\text{Be}$  reaction. This treatment assumes that the Q value for both the  ${}^{12}\text{C}(n,d){}^{11}\text{B}$  ( $Q = -13.7$ ) and  ${}^{12}\text{C}(n,p){}^{12}\text{B}$  ( $Q = -12.6$ ) reactions are equal, and that the ratio of the  ${}^{12}\text{C}(n,d){}^{11}\text{B}$  and  ${}^{12}\text{C}(n,p){}^{12}\text{B}$  cross-sections are approximately the same as those of the free  $p(n,p)n$  and  $p(n,d)\pi^0$ .

The deconvolution was done by an iterative procedure. The kinetic energy spectrum  $N(K_n)$  was first estimated from the neutron energy distribution observed in other CHARGEEX experiments by placement of a thin  $\text{CH}_2$  scatterer in the neutron beam produced by the  ${}^7\text{Li}(p,n){}^7\text{Be}$  reaction (figure 5.1). Our model consisted of a delta function response for the  ${}^7\text{Li}(p,n){}^7\text{Be}$  reaction, and a second delta function representing a broad excited state of  ${}^7\text{Be}$  situated approximately 10 MeV lower in energy. Because this peak was broad, we allowed its position to move small amounts in order to best fit our data. A long, nearly flat, neutron tail from lithium breakup reactions exists at energies below the one corresponding to the  ${}^7\text{Be}$  excited state. Above this energy the neutron tail declines linearly to a second flat region approximately 2 MeV from the main peak. This distribution is shown in figure 5.2. The relative heights of the main and secondary peak ( $H_1/H_2$ ), the secondary peak to the constant background ( $H_2/B_2$ ), the position of the secondary peak ( $\Delta E$ ), and the energy at which the linear decrease ended ( $\Delta E_2$ ), were all taken as parameters of the neutron energy shape.

The momentum dispersion of protons due to energy losses was much smaller than that for deuterons, therefore the neutron lineshape at a particular energy was first estimated by first obtaining the approximate MRS response function by fitting the principle (n,p) momentum peak to a triple gaussian of the form

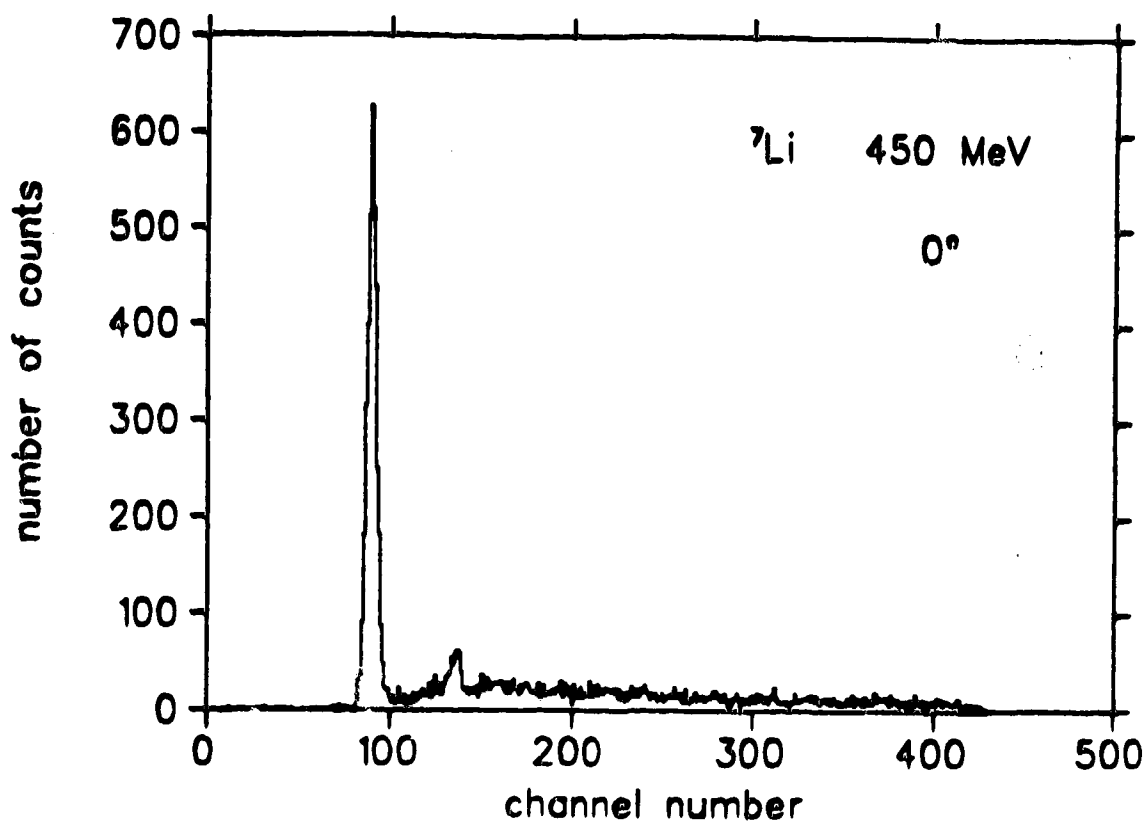


Figure 5.1 : Neutron Spectrum from the (n,p) Reaction on Li at 450 MeV. The energy of the neutrons is measured by momentum analysing the recoil protons from a CH<sub>2</sub> target. The secondary peak is from the (n,p) reaction on the carbon in this target and is approximately 12.5 MeV lower in energy than the main peak.

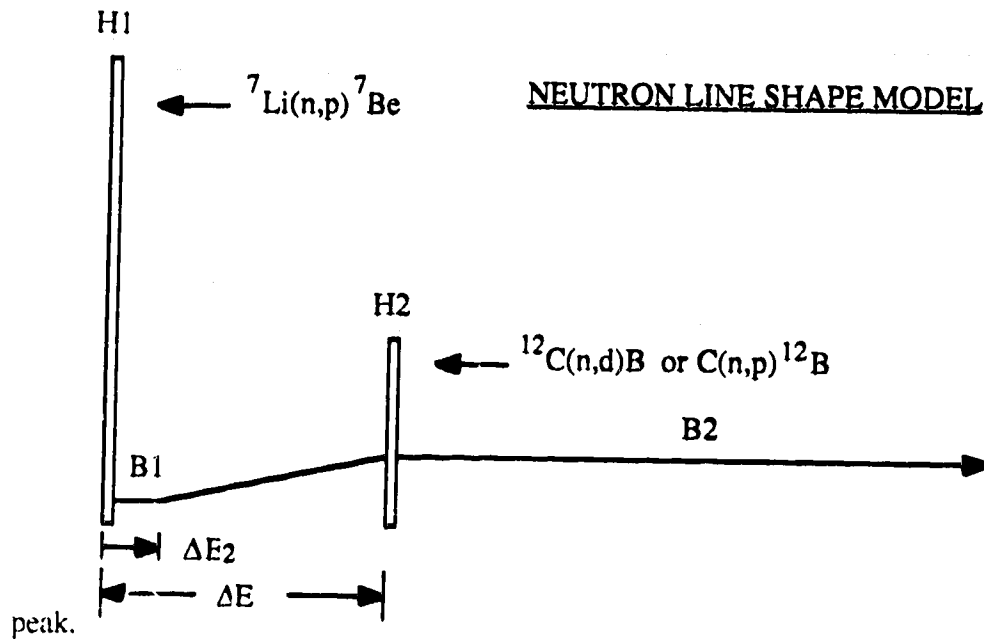


Figure 5.2: This picture shows the model used for the neutron energy distribution of the MRS CHARGEEX system,  $N(K_n)$ . Adjustable parameters were  $H1/H2$ ,  $H2/B2$ ,  $H2/B1$ ,  $\Delta E$  and  $\Delta E_2$ .

$$y = A(e^{-(p - P_0 - W)^2/2S^2} + e^{-(p - P_0)^2/2S^2} + e^{-(p - P_0 + W)^2/2S^2}). \quad (V-1)$$

$y$  represents the counts at momentum  $p$ ,  $P_0$  is the center of the peak,  $S$  is the nominal standard deviation of the intrinsic spectrometer response, and  $W$  is a parameter introduced to mimic the spreading of the normal gaussian shape due to energy losses in the LH<sub>2</sub>. Figure 5.3 shows the  $p(n,p)n$  spectrum at 360 MeV and the region of the spectrum which was used to find the parameters of the triple gaussian in V-1. This fit was done using the computer program OPDATA (see the TRIUMF documentation<sup>(37)</sup> for details on this program). The function  $MRS(\Delta p)$  could now be provisionally defined in terms of the parameters  $W$  and  $S$  as

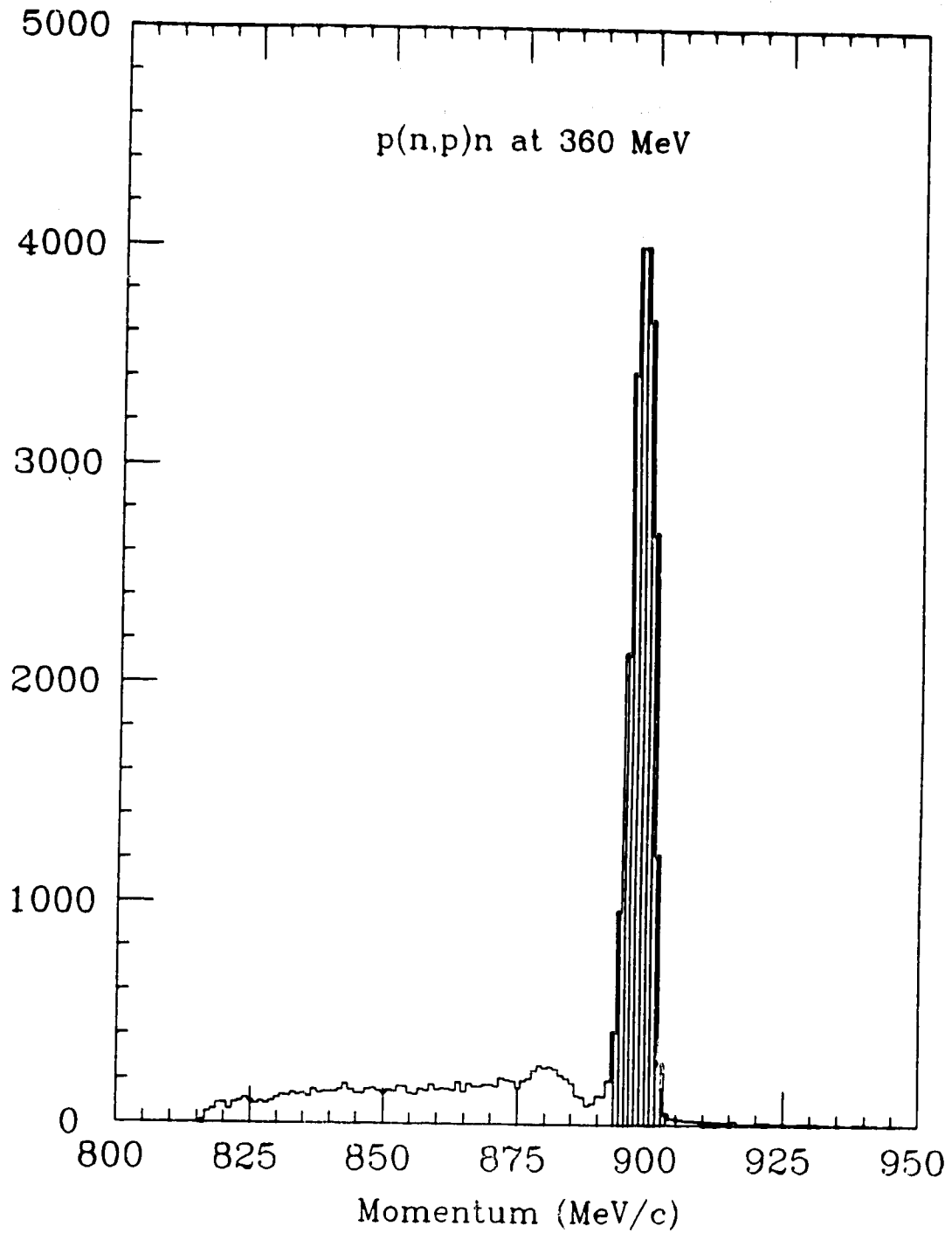


Figure 5.3 : p(n,p)n at 360 MeV. The high energy side of the elastic scattering peak, indicated here by the shading, was used to provide an approximation to the MRS response function at each energy.

$$\text{MRS}(\Delta p) = \frac{1}{3\sqrt{\pi} S} (e^{-(\Delta p - w)^2/2S^2} + e^{-\Delta p^2/2S^2} + e^{-(\Delta p + w)^2/2S^2}). \quad (\text{V-2})$$

The convolution integral

$$C(p) = \int_{K_n} \text{MRS}(p - P(K_n)) N(K_n) \sigma(K_n) P'(K_n) dK_n \quad (\text{V-3})$$

could now be performed. In V-3,  $K_n$  is the neutron kinetic energy,  $N(K_n)$  and  $C(p)$  are the neutron energy distributions and predicted momentum distributions respectively, and  $P(K_n)$ , and its derivative  $P'(K_n)$ , contain the relativistic kinematics for calculating the reaction product momentum from the neutron kinetic energy.  $\sigma(K_n)$  is an approximation to the energy dependence of the cross-section for the reaction being studied. For elastic scattering we used the energy dependence predicted by the phase shift analysis (Arndt 1988) program SAID (for Scattering Analysis Interactive Dial-in), and for pion creation we used the data from ref.<sup>(38)</sup>. The neutron energy distribution parameters were now adjusted by hand to achieve a good fit between  $C(p)$  and the raw data in the main peak and the lower energy region immediately beside it. If a good fit could not be obtained the entire procedure was iterated by subtracting the fitted neutron tail, which was defined as the convolution of the entire neutron spectrum except for the first delta function, from the experimental data, and then refitting the new main peak shape thus obtained using OPDATA. In practice the first iteration was usually quite good, since the proton peak was well defined and overlapped the protons created by the neutron tail by only a small amount.

After the parameters of the neutron energy distribution had been adjusted to provide a good fit to the (n,p) momentum peak, they were then held fixed for the rest of the analysis at each energy. Once a fit had been made to a given peak, points on each

side of the peak,  $P_L$  and  $P_R$ , were chosen and the number of events between them summed. Corrections were made for the loss of good events on the low energy side of the summation region, and for the inclusion of events produced by the background from the neutron tail. The number of events in the peak was then defined as

$$R[\text{reaction}] = \sum_{P_L}^{P_R} \text{Raw data} - \int_{P_L}^{P_R} C_T(p) dp + \int_{-\infty}^{P_L} C_p(p) dp. \quad (\text{V-4})$$

The functions  $C_p(p)$  and  $C_T(p)$  are the convolutions of the neutron energy main peak and tail distributions respectively, as given by V-5.

$$C_\alpha(p) = \int_{\alpha} \text{MRS}(p - P(K_n)) N(K_n) \alpha(K_n) P'(K_n) dK_n. \quad (\text{V-5})$$

Figure 5.4 illustrates the two corrections to the sum of the data in equation V-4.

Once each peak had been summed, the overall ratio

$$R = \frac{R[p(n,d)\gamma]}{R[p(n,d)\pi^0]} * \frac{R[p(n,d)\pi^0]}{R[p(n,p)n]}, \quad (\text{V-6})$$

then supplies the relative  $p(n,d)\gamma$  and  $p(n,p)n$  reaction rates. The statistical error in  $R$  is calculated assuming that the errors in the terms making up each  $R[\text{reaction}]$  are distributed according to a Poisson distribution, so that the square of the standard deviation of  $R[\text{reaction}]$  is the sum of the squares of the numbers involved. If  $R_1$  through  $R_4$  represent the median values for the four reactions in V-6, then to first order,

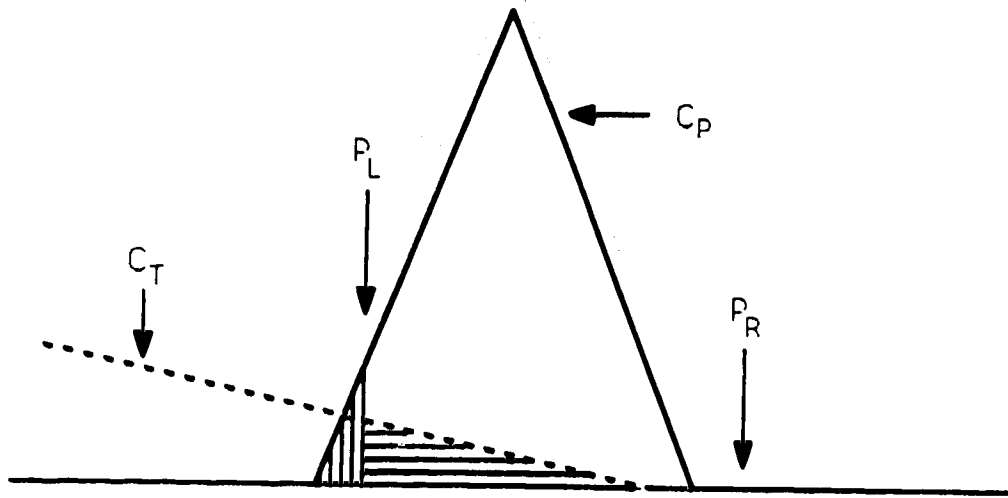


Figure 5.4: Corrections to the Sum of the Raw Data in a Peak. The area outlined in horizontal lines is the contribution of the leading edge of the neutron tail, and must be subtracted. The area outlined in vertical lines is the extension of the peak past the point to which data was summed, and is added.

$$\Delta R = \sqrt{\sum_i \left\{ \frac{\partial R}{\partial R_i} \right\}^2 \delta^2 R_i}. \quad (V-7)$$

$\delta R_i$  is the standard error in the number of counts in peak  $i$  and is equal to the square root of  $R_i$  for a Poisson process. The elimination of second order terms is justified in the limit of good statistics in the peaks,  $\delta R_i/R_i \ll 1$ . Since the ratio of the standard deviation to the mean for the  $p(n,d)\gamma$  reaction, which had the poorest statistics, was less than 0.1 in all cases, second order effects must be on the order of 0.01, and were therefore negligible.

Putting this altogether, the relative rate of the  $p(n,d)\gamma$  and  $p(n,p)n$  reactions, with its statistical error, may be written in our case as



$$R \pm \Delta R = \frac{R_1 R_3}{R_2 R_4} \left\{ 1 \pm \sqrt{\sum_{i=1}^4 \frac{1}{R_i}} \right\}. \quad (\text{V-8})$$

## V.2 BACKGROUNDS UNCONNECTED TO THE NEUTRON TAIL

Underlying all the peaks was a relatively constant background which could not be eliminated by any of the cuts mentioned in chapter IV. The source of these events was certainly (n,d) and (n,p) reactions occurring in non-target material which were not eliminated by the scintillators inside the LH<sub>2</sub> vacuum vessel, as discussed in detail in chapters III and IV, as well as undetected scattering within the MRS. This background was very small relative to the rates from the p(n,d)π<sup>0</sup> and p(n,p)n reactions, but was non-negligible (about 5-10%, depending on energy) compared to the p(n,d)γ reaction. Accordingly, the number of background events per channel per unit of beam charge was estimated by observing the reaction rate on the high energy side of the p(n,d)γ peak, as shown in figure 5.5. The projection of this background underneath the p(n,d)γ peak was subtracted from the number of counts in V-4 in section V.1. This procedure assumes a flat background. This assumption was tested at each energy by subtracting the neutron tail and p(n,d)γ tail (events belonging to the main peak) contributions from the raw data on the low energy side of the peak, and checking that, within standard statistical error, the remaining level was the same as that on the high energy side.

Once the number of background events per unit charge had been established in the preceding manner, it was used to correct equation V-4 for all the peaks involving deuterons. This correction was significant, on the order of 10%, for the p(n,d)γ peak but provided a negligible correction to the p(n,d)π<sup>0</sup> peaks, because of the much larger event rate (compared to the background) although this correction was quite small for all peaks except the p(n,d)γ peak. No background correction was done for the p(n,p)n peak for this reason.

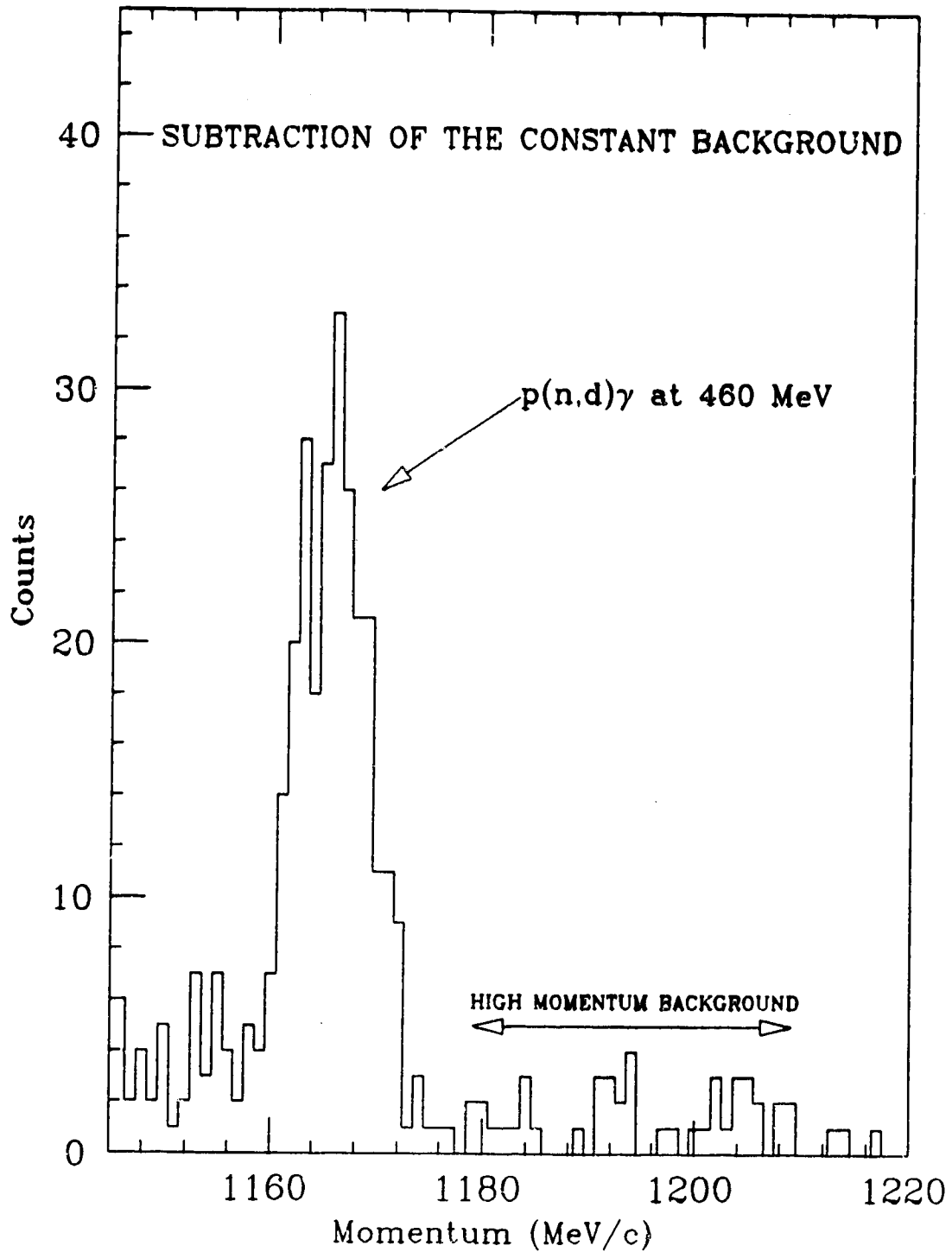


Figure 5.5 : The background on the high momentum side was averaged and then projected underneath the p(n,d)γ peak.

### V.3 FITTING THE REACTION PEAKS (PRACTICE)

#### V.3.1 Results at 460 MeV

Figure 5.6 shows the final momentum spectra for the  $p(n,d)\gamma / p(n,d)\pi^0$  run and the  $p(n,d)\pi^0 / p(n,p)n$  normalising run at 460 MeV. We found that the best fit to the data was achieved with neutron energy spectra parameters (see fig 5.2):  $\Delta E = 10$  MeV,  $\Delta E_2 = 2$  MeV,  $H1/H2 = 28.57$ ,  $H2/B2 = 2.8$ ,  $H2/B1 = 13$ . The corresponding MRS response functions were given by the parameters (refer to V-1):  $S = 1.28$  MeV/c,  $\Delta C = 1.35$  MeV/c for protons and  $S=2.5$  MeV/c,  $\Delta C = 3.27$  MeV/c for deuterons. Figure 5.7, showing the fit to the  $d\pi^0$  peak is appended as an example of the fit at this energy. This fit was tested by checking that the sum in equation V-4 was independent of the choice of  $P_L$ , the point at which the fit was abandoned and the experimental data summed. No correlation between  $R[p(n,d)\pi^0]$  and  $P_L$  above standard statistical uncertainty was observed for small variations in  $P_L$ . The results are displayed in table 5.1. A constant background of  $5.71 \times 10^{-2}$  counts/(MeV/c)/mC was observed to the high energy side of the  $d\gamma$  peak, and this was subtracted from all the deuteron peaks. The correction was 7.5% for the  $d\gamma$  peak, but negligible for the two  $d\pi^0$  peaks. We checked the assumption that this background was constant by subtracting the neutron tail contribution from the low energy side of the  $p(n,d)\gamma$  peak and comparing the remaining number of counts to the background on the high energy side. The sum of the raw data over a 16 MeV/c interval (1140 to 1155, inclusive) on the low energy side of the  $p(n,d)\gamma$  peak gave 67 counts, while the integral of the fitting curve predicted 63.6 counts - clearly well within statistical error.

After this background subtraction, the  $p(n,d)\gamma$  to  $p(n,p)n$  ratio, using V-4 and V-10, yielded

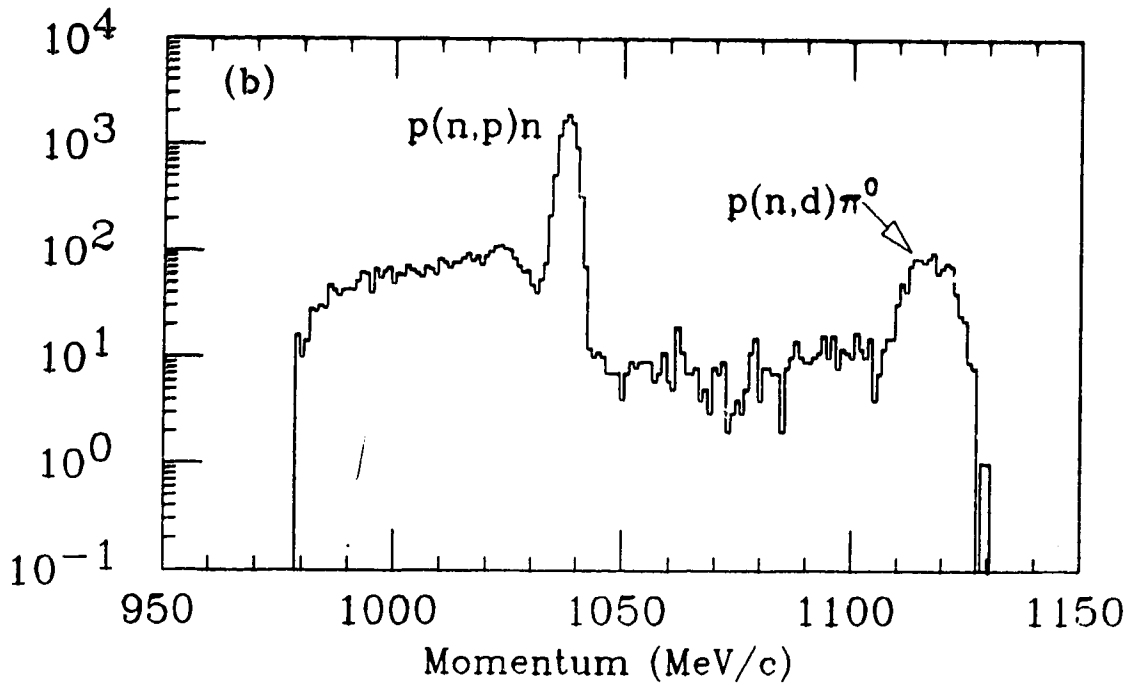
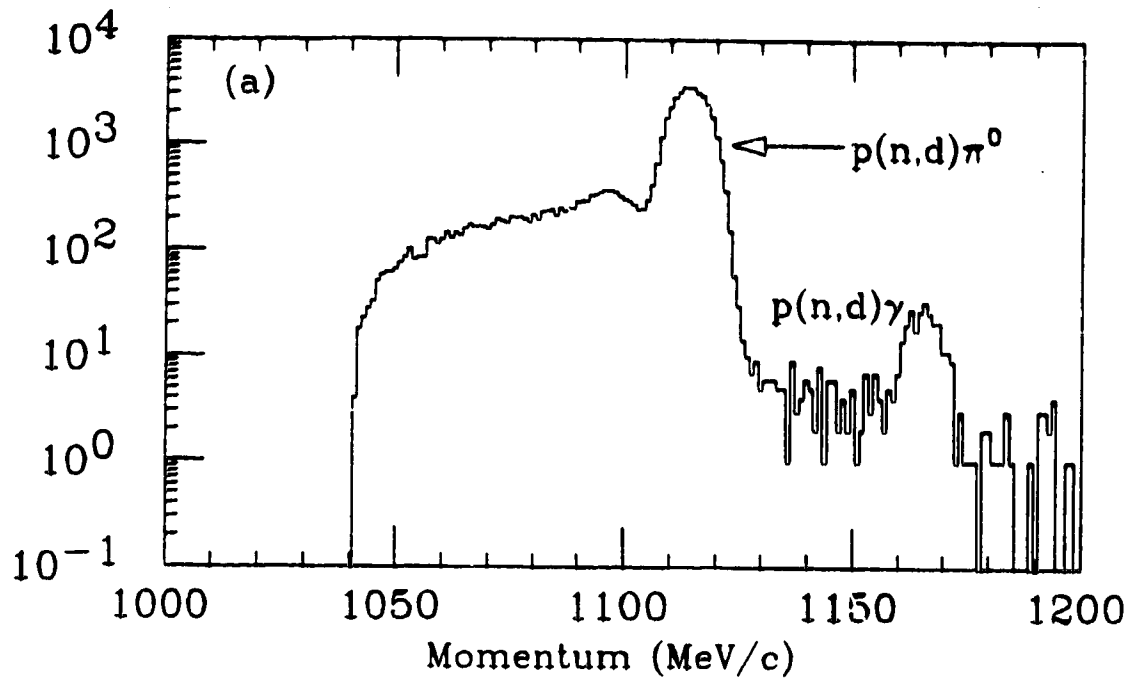


Figure 5.6 : Momentum Spectra at 460 MeV. Spectrum a) shows  $p(n,d)\gamma$  vs.  $p(n,d)\pi^0$ , while spectrum b) shows  $p(n,d)\pi^0$  vs.  $p(n,p)n$ .

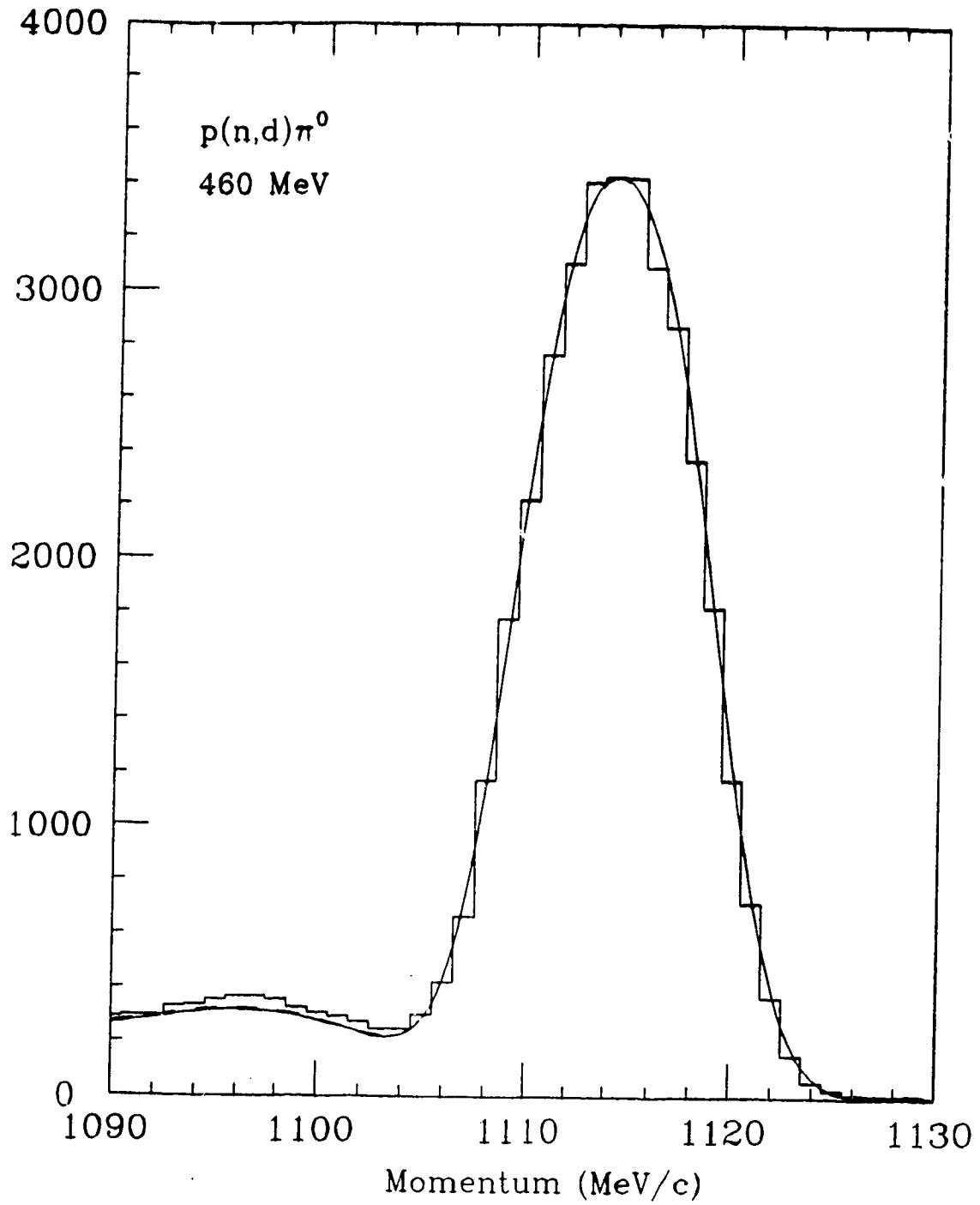


Figure 5.7 : An Example of the Fit to the  $p(n,d)\pi^0$  Peak. The convolution of the model of the neutron spectrum with the MRS response function provides the solid line.

Table 5.1: Reaction Sums at 460 MeV. *Events in Tail* refers to the analytic continuation of the peak outside the summation limits, *Events due to L.E. Neutrons* is the projection of the neutron tail underneath the peak.

FIRST RUN (23.30 mC @ 87% livetime)

| <i>Reaction</i> | <i>Raw Data</i> | <i>Events in Tail</i> | <i>Events due to</i> |              |
|-----------------|-----------------|-----------------------|----------------------|--------------|
|                 |                 |                       | <i>L.E. Neutrons</i> | <i>Total</i> |
| p(n,d) $\gamma$ | 246             | 24.01                 | 3.22                 | 257          |
| p(n,d) $\pi^0$  | 33940           | 1101.15               | 492.29               | 34549        |

SECOND RUN (0.53 mC @ 77% livetime)

| <i>Reaction</i> | <i>Raw Data</i> | <i>Events in Tail</i> | <i>Events due to</i> |              |
|-----------------|-----------------|-----------------------|----------------------|--------------|
|                 |                 |                       | <i>L.E. Neutrons</i> | <i>Total</i> |
| p(n,d) $\pi^0$  | 978             | 29.95                 | 13.38                | 995          |
| p(n,p)n         | 8353            | 68.59                 | 32.95                | 8389         |

$$R_{460} = (8.5478 \pm 0.6584) \times 10^{-4}.$$

In order to convert this relative rate in the lab to a relative rate in the center of mass, we first calculated the lab MRS physical acceptance versus angle function,  $A(\theta)$  (plotted in figure 5.8), by taking the observed number of counts versus angle for the  $p(n,p)n$  reaction and unfolding the  $p(n,p)n$  angular distribution of the cross-section obtained using the computer program SAID. For 460 MeV neutrons, this theoretical c.m. cross-section was

$$\begin{aligned} \frac{d\sigma}{d\Omega} [p(n,p)n] = & 10.787 - 5.714 \times 10^{-2} \theta^2 + 2.646 \times 10^{-4} \theta^4 \\ & - 6.240 \times 10^{-7} \theta^6 + 5.696 \times 10^{-10} \theta^8 \end{aligned} \quad (V-9)$$

where  $\theta$  is in degrees.

$A(\theta)$  thus contained both phase space considerations and the physical limitations of the MRS. For computational convenience, it was normalised to unity. The ratio of  $p(n,p)n$  to  $p(n,d)\gamma$  Jacobians was then calculated as

$$\frac{\int_{\text{lab angle}} \frac{d\Omega_{\text{c.m.}}^{\text{protons}}}{d\Omega_{\text{lab}}} A(\theta)}{\int_{\text{lab angle}} \frac{d\Omega_{\text{c.m.}}^{\text{deutrons}}}{d\Omega_{\text{lab}}} A(\theta)} \quad (V-10)$$

This integral was made necessary by the different angular dependence of the  $p(n,p)n$  and  $p(n,p)\gamma$  Jacobians, but this consideration was only important at the 0.5% level. The ratio of available c.m. phase space from V-10 was 4.98/31.6. The average  $p(n,p)n$  cross-section over the available phase space was then calculated using



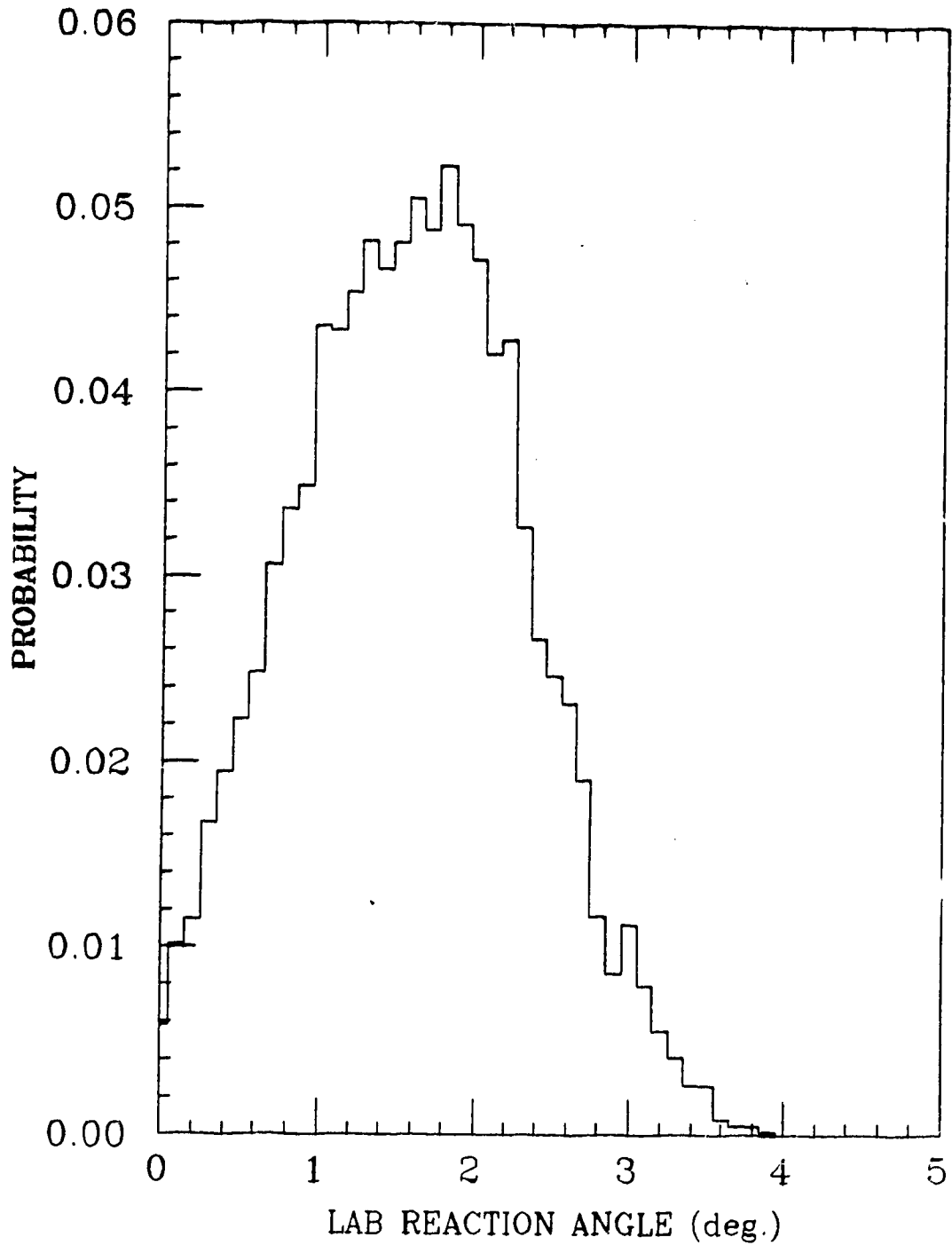


Figure 5.8 : The MRS Acceptance Function. This function is the average probability of an event being observed by the MRS for a given scattering angle at the MRS target position. The above function models the quadrupole\_on configuration.

$$\overline{\frac{d\sigma}{d\Omega}}(\text{c.m.}) = \int_{\text{lab angle}} \frac{d\sigma}{d\Omega}(\text{c.m.}) A(\theta). \quad (\text{V-11})$$

This was 9.98 mb/sr at 460 MeV. The p(n,d) $\gamma$  c.m. cross-section could now be calculated by multiplying the proton to deuteron relative rate,  $R_{460}$ , by the ratio of Jacobians and the average p(n,p)n cross-section as follows:

$$\frac{d\sigma}{d\Omega} [p(n,d)\gamma] = R_{460} \frac{4.98}{31.6} 9.98 \times 10^3 \mu\text{b/sr}. \quad (\text{V-12})$$

This is  $1.32 \mu\text{b/sr} \pm 0.10 \mu\text{b/sr}$ . As yet this is still averaged over the reaction angle spectrum, which peaks at  $10^\circ$ – $12^\circ$  c.m. for deuterons. This was converted this to an equivalent photo-disintegration cross-section, for ease of comparison to the world data set and theoretical predictions, by means of detailed balance. The prediction of detailed balance for p(n,d) $\gamma$ , in the center of mass,

$$\frac{d\sigma[d(\gamma,p)n]}{d\sigma[p(n,d)\gamma]} = \frac{2}{3} \frac{p_n^2}{p_\gamma^2}. \quad (\text{V-13})$$

At 460 MeV neutron energy, this factor is 3.33, giving us an equivalent photo-disintegration cross-section of

$$\frac{d\sigma}{d\Omega} [d(\gamma,p)n] = 4.39 \pm 0.35 \mu\text{b/sr}$$

at an equivalent lab gamma energy of 232.5 MeV. Figure 5.9 plots this value against some 240 MeV differential cross-section data at various angles from Frascati<sup>(4)</sup>, along with their Legendre polynomial fit. This fit is done with Legendre polynomials to order

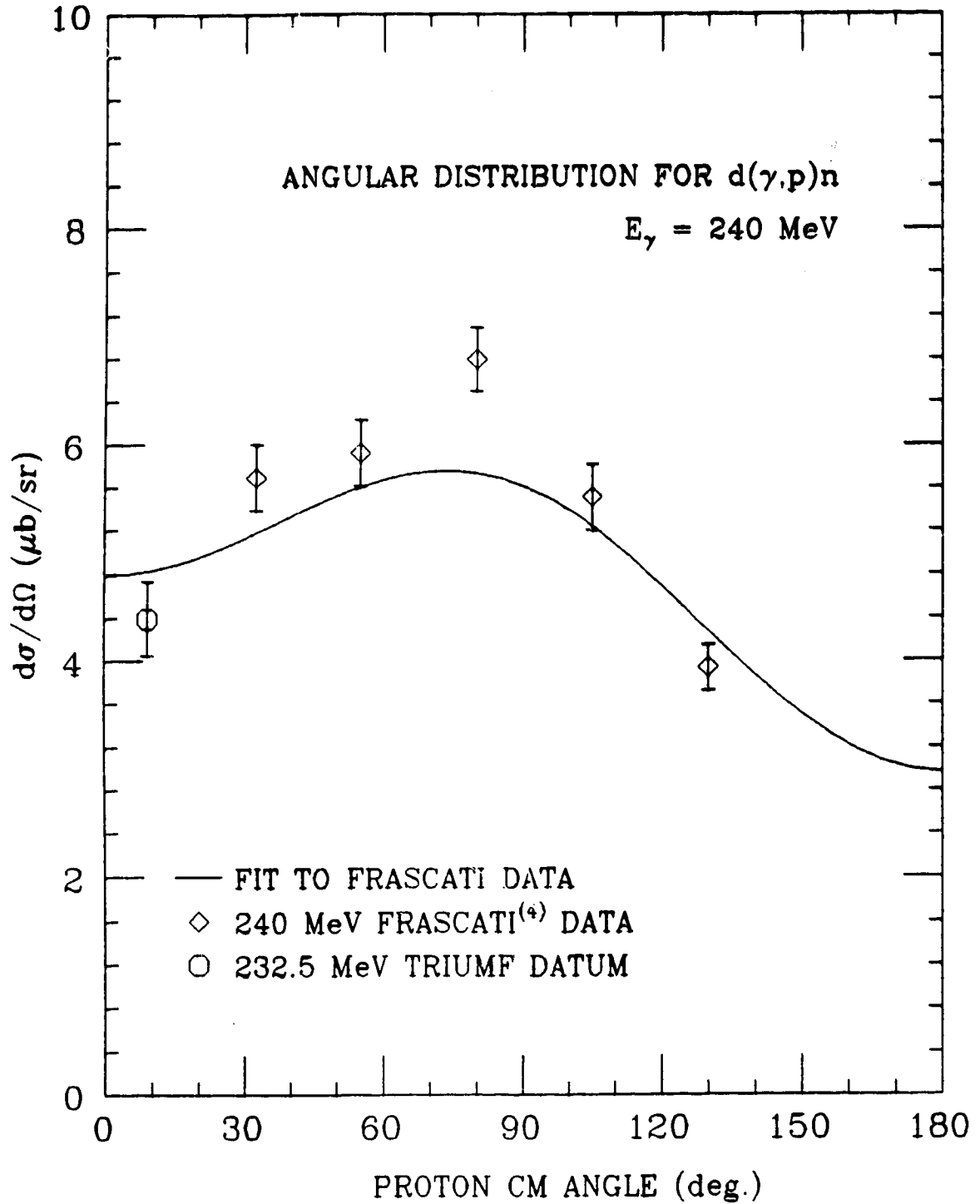


Figure 5.9: A zero degree cross-section prediction was obtained from this experiment's 232.5 MeV datum by extrapolating along the Frascati 240 MeV fit.

3 and included the data from Arends et al.<sup>(39)</sup> and Baba et al.<sup>(40)</sup> (which is the reason that the fit does not run particularly close to the Frascati data set). Our point was plotted at the average reaction angle accepted by the MRS ( $\theta$  averaged over  $A(\theta)$ ). In order to facilitate comparison with theory, we projected our result to a zero degree result by projecting along this fit. The fit was used to find an average cross-section over the observed reaction angle spectrum which was compared to the zero degree value.

$$\frac{d\sigma}{d\Omega}(0^\circ) = \frac{F(0)}{\int_{\theta} A(\theta) F(\theta) d\theta} \left. \frac{d\sigma}{d\Omega} \right|_{\text{THRE}} \quad (\text{V-14})$$

$A(\theta)$  is the MRS acceptance as before, the subscript 'THRE' refers to the average cross-section for the entire available angular range, and  $F(\theta)$  is the Legendre fit. With Frascati's quoted values for the errors in their fitting coefficients, the zero degree cross-section is

$$\frac{d\sigma}{d\Omega}(0^\circ) = 4.35 \pm 0.34 \pm 0.05 \mu\text{b/sr}$$

The second error is the estimated systematic one introduced by the quoted errors in the Legendre coefficients for the Frascati fit.

### V.3.2 Results at 410 MeV

Figure 5.10 shows the final momentum spectra for the  $p(n,d)\gamma / p(n,d)\pi^0$  run and the  $p(n,d)\pi^0 / p(n,p)n$  normalising run at 410 MeV. For this energy, the neutron energy spectrum parameters were almost unchanged from 460 MeV. They were  $\Delta E = 10$  MeV,  $\Delta E_2 = 2$  MeV,  $H1/H2 = 30.04$ ,  $H2/B2 = 3.0$ ,  $H2/B1 = 15$ . The corresponding

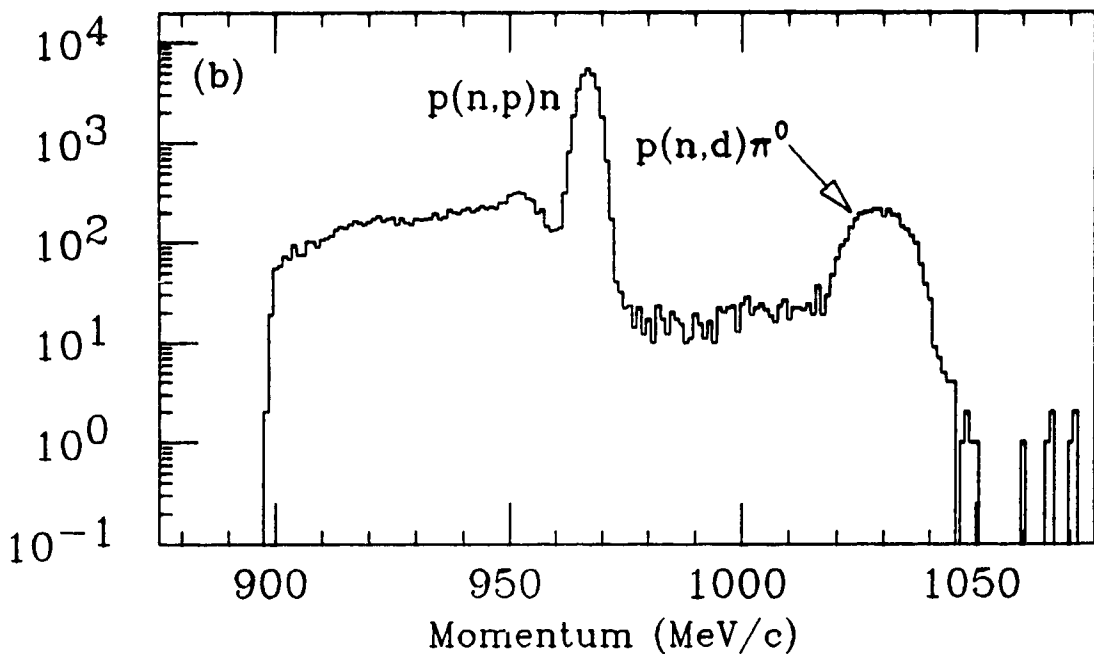
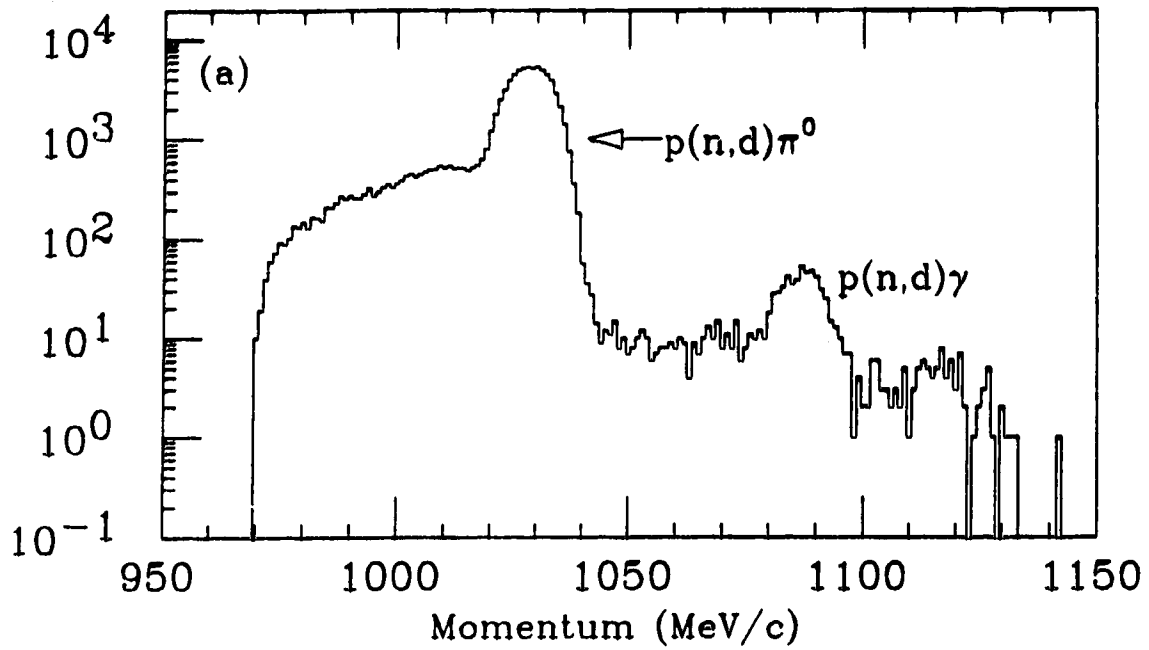


Figure 5.10 : Momentum Spectra at 410 MeV. Spectrum a) shows  $p(n,d)\gamma$  vs.  $p(n,d)\pi^0$ , while spectrum b) shows  $p(n,d)\pi^0$  vs.  $p(n,p)n$ .

MRS response functions were given by the parameters (refer to V-1):  $S = 1.5 \text{ MeV/c}$ ,  $\Delta C = 1.35 \text{ MeV/c}$  for protons and  $S = 2.88 \text{ MeV/c}$ ,  $\Delta C = 3.99 \text{ MeV/c}$  for deuterons. The results are given in table 5.2.

The irreducible background was  $1.19 \times 10^{-1} \text{ counts/(MeV/c)/mC}$ . This is somewhat lower than the 460 MeV case since the  $C(n,d)X$  reaction cross-section drops rapidly as the energy increases. At this energy the difference between the fit and the observed rates on the low energy side of the  $p(n,d)\gamma$  peak was  $21.8 \pm 14.14$  counts, a difference somewhat larger than one standard from zero but not inconsistent with it.

With the background correction, the  $p(n,d)\gamma$  to  $p(n,p)n$  ratio was

$$R_{410} = (7.737 \pm 0.4612) \times 10^{-4}.$$

The 410 MeV  $d\gamma$  Jacobian is 33.59, the  $np$  Jacobian is 4.87 and the average  $p(n,p)n$  cross-section, using the SAID approximation

$$\begin{aligned} \frac{d\sigma}{d\Omega} [p(n,p)n] = & 10.999 - 5.2388 \times 10^{-2} \theta^2 + 2.2742 \times 10^{-4} \theta^4 \\ & - 5.152 \times 10^{-7} \theta^6 + 4.589 \times 10^{-10} \theta^8, \end{aligned} \quad (\text{V-15})$$

where  $\theta$  is the lab scattering angle of the target proton in degrees, and the result is in mb/sr, was 10.20 mb/sr. The 410 MeV cross-section is then computed analogously to V-12 and yields  $1.15 \mu\text{b/sr} \pm 0.07 \mu\text{b/sr}$ . The detailed balance considerations then supply a factor of 3.64, so the equivalent photo-disintegration cross-section, at a lab photon energy of 207.5 MeV is

**Table 5.2: Reaction Sums at 410 MeV.** *Events in Tail* refers to the analytic continuation of the peak outside the summation limits, *Events due to L.E. Neutrons* is the projection of the neutron tail underneath the peak.

**FIRST RUN** (34.5 mC @ 95% livetime)

| <i>Reaction</i> | <i>Raw Data</i> | <i>Peak Tail</i> | <i>Events due to</i> |              |
|-----------------|-----------------|------------------|----------------------|--------------|
|                 |                 |                  | <i>L.E. Neutrons</i> | <i>Total</i> |
| p(n,d) $\gamma$ | 525             | 11.75            | 6.81                 | 530          |
| p(n,d) $\pi^0$  | 62400           | 2102.07          | 974.94               | 63527        |

**SECOND RUN** (1.11 mC @ 83% livetime)

| <i>Reaction</i> | <i>Raw Data</i> | <i>Peak Tail</i> | <i>Events due to</i> |              |
|-----------------|-----------------|------------------|----------------------|--------------|
|                 |                 |                  | <i>L.E. Neutrons</i> | <i>Total</i> |
| p(n,d) $\pi^0$  | 3073            | 12.94            | 74.55                | 3011         |
| p(n,p)n         | 26940           | 189.02           | 211.90               | 26917        |

$$\frac{d\sigma}{d\Omega} [d(\gamma,p)n] = 4.15 \pm 0.25 \mu\text{b/sr} .$$

We plot this point, using the average reaction angle, in figure 5.11 against the recent Frascati data at 200 MeV. The projection to zero degrees along the Frascati fit, using equation V-14, provided the zero degree cross-section

$$\frac{d\sigma}{d\Omega} (0^\circ) = 4.03 \pm 0.25 \pm 0.08 \mu\text{b/sr}$$

### V.3.3 Results at 360 MeV

The 360 MeV momentum spectra are shown in figure 5.12. The neutron energy spectra parameters used for this energy were:  $\Delta E = 11$  MeV  $\Delta E_2 = 5.5$  MeV,  $H1/H2 = 28.39$ ,  $H2/B2 = 3.2$ ,  $H2/B1=6.15$ . The MRS response function for protons had  $S=1.2629$  and  $\Delta C=1.8379$ , while the response function for deuterons had  $S=2.2508$  and  $\Delta C=4.7157$ . The data and fit results are tabulated in table 5.3. The background on the high energy side of the  $p(n,d)\gamma$  peak was  $5.33 \times 10^{-1}$  counts/(MeV/c)/mC. The fit predicted 65.88 counts in a 15 MeV/c region on the low energy side of the  $p(n,d)\gamma$  peak, as compared to an actual number of 71, clearly well within the statistical uncertainty. With this background subtracted, the ratio  $R_{360}$  was

$$R_{360} = (6.8172 \pm 0.6092) \times 10^{-4}$$

The  $p(n,d)\gamma$  to  $p(n,p)n$  ratio of Jacobians at this energy is 36.41/4.75, and the average of the elastic scattering cross-section, using a SAID prediction of



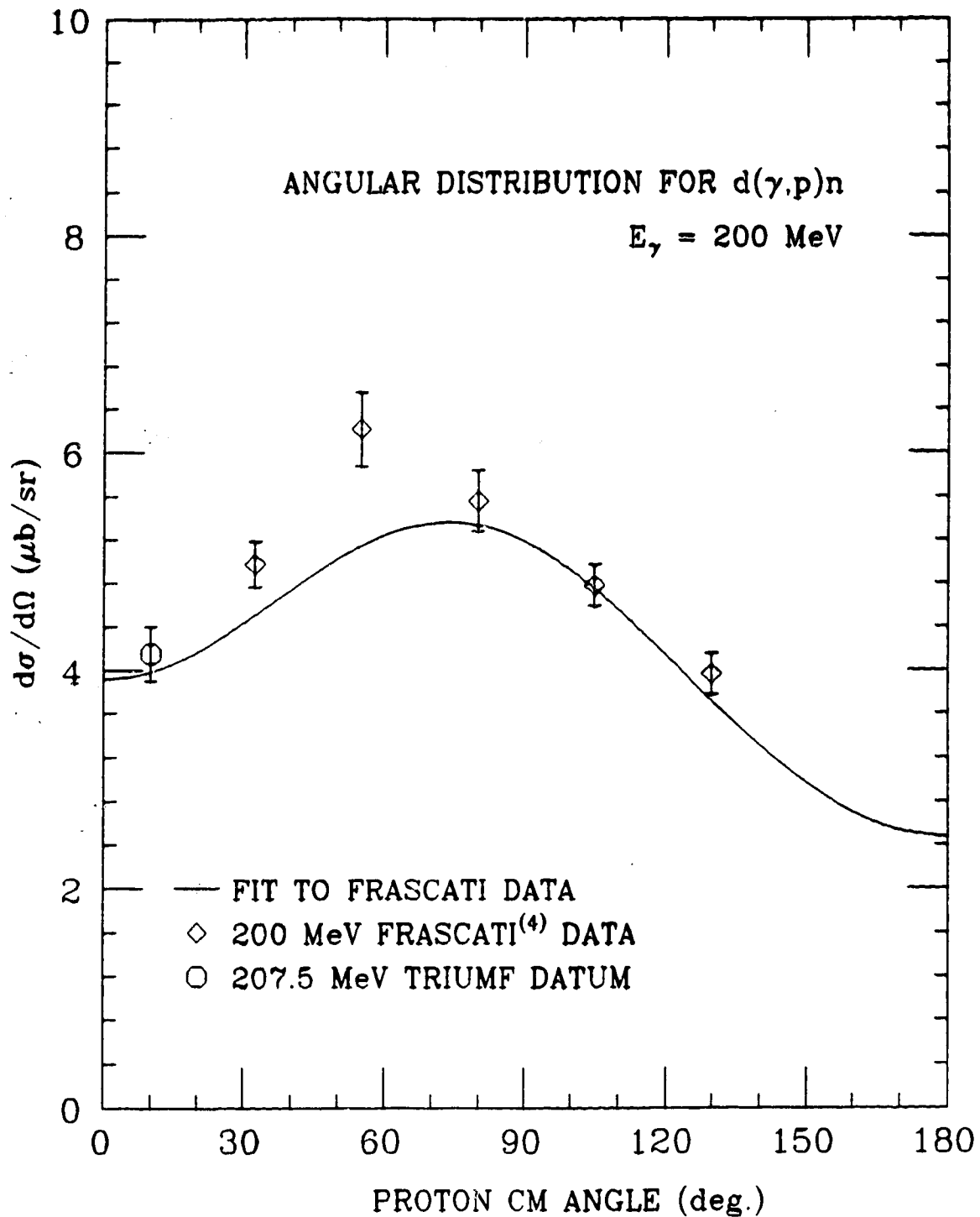


Figure 5.11: A zero degree cross-section prediction was obtained from this experiment's 207.5 MeV point by extrapolating along the Frascati 200 MeV fit.

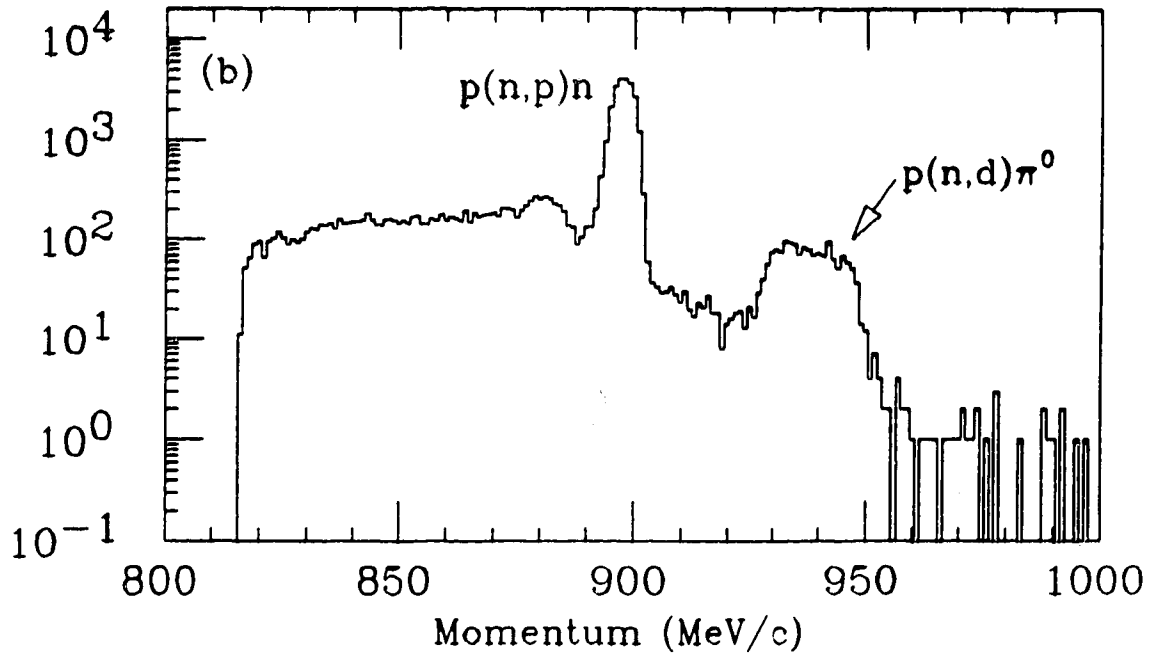
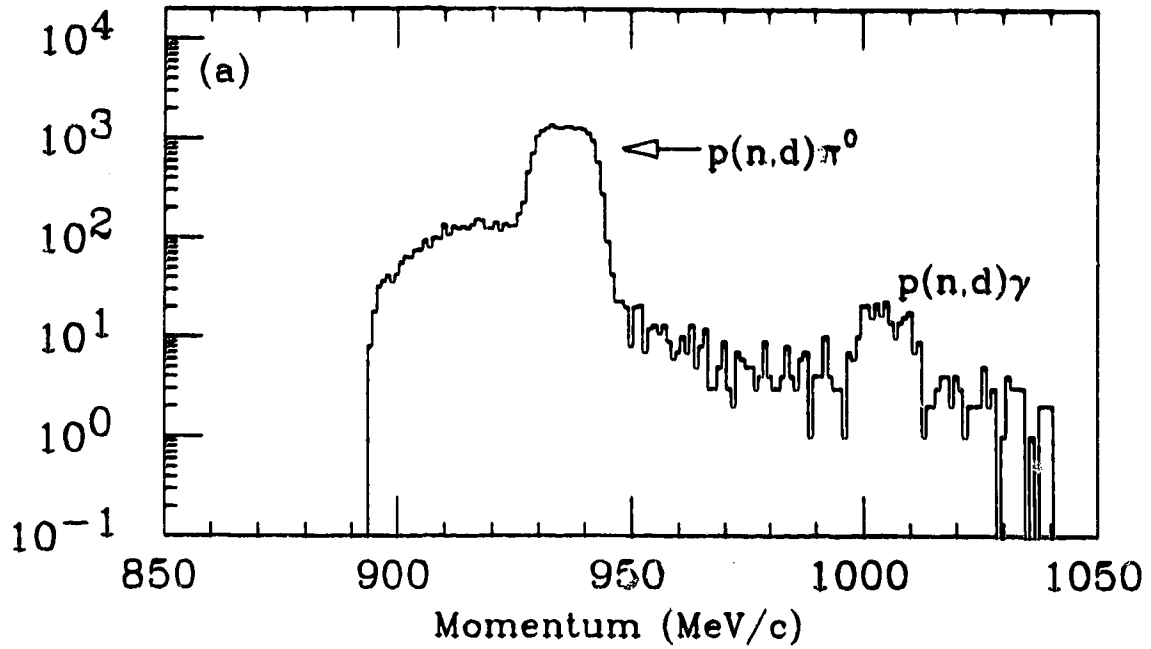


Figure 5.12 : Momentum Spectra at 360 MeV. Spectrum a) shows  $p(n,d)\gamma$  vs.  $p(n,d)\pi^0$ , while spectrum b) shows  $p(n,d)\pi^0$  vs.  $p(n,p)n$ .

**Table 5.3: Reaction Sums at 360 MeV.** *Events in Tail* refers to the analytic continuation of the peak outside the summation limits, *Events due to L.E. Neutrons* is the projection of the neutron tail underneath the peak

FIRST RUN (4.73 mC @ 87% livetime)

| <i>Reaction</i> | <i>Raw Data</i> | <i>Peak Tail</i> | <i>Events due to</i> |              |
|-----------------|-----------------|------------------|----------------------|--------------|
|                 |                 |                  | <i>L.E. Neutrons</i> | <i>Total</i> |
| p(n,d) $\gamma$ | 219             | 13.85            | 4.84                 | 228          |
| p(n,d) $\pi^0$  | 18312           | 392.00           | 408.99               | 18295        |

SECOND RUN (0.689 mC @ 79% livetime)

| <i>Reaction</i> | <i>Raw Data</i> | <i>Peak Tail</i> | <i>Events due to</i> |              |
|-----------------|-----------------|------------------|----------------------|--------------|
|                 |                 |                  | <i>L.E. Neutrons</i> | <i>Total</i> |
| p(n,d) $\pi^0$  | 1464            | 50.31            | 54.33                | 1460         |
| p(n,p)n         | 22488           | 278.8            | 316.44               | 22450        |

$$\frac{d\sigma}{d\Omega} [p(n,p)n] = 11.213 - 4.904 \times 10^{-2} \theta^2 + 2.358 \times 10^{-3} \theta^4 - 6.852 \times 10^{-7} \theta^6, \quad (V-16)$$

over the observed reaction angle spectrum was 11.07 mb/sr. Putting this together, we arrive at a radiative capture cross-section of  $0.99 \pm 0.09 \mu\text{b/sr}$ . Converting this to a photo-disintegration cross-section gives

$$\frac{d\sigma}{d\Omega} [d(\gamma,p)n] = 4.00 \pm 0.36 \mu\text{b/sr}$$

at an equivalent lab photon energy of 182.5 MeV. This value, along with the Frascati 200 MeV points and the fit used to extrapolate to zero degrees is shown in fig 5.13. The result of extrapolation was a value of

$$\frac{d\sigma}{d\Omega} (0^\circ) = 3.93 \pm 0.35 \pm 0.03 \mu\text{b/sr} .$$

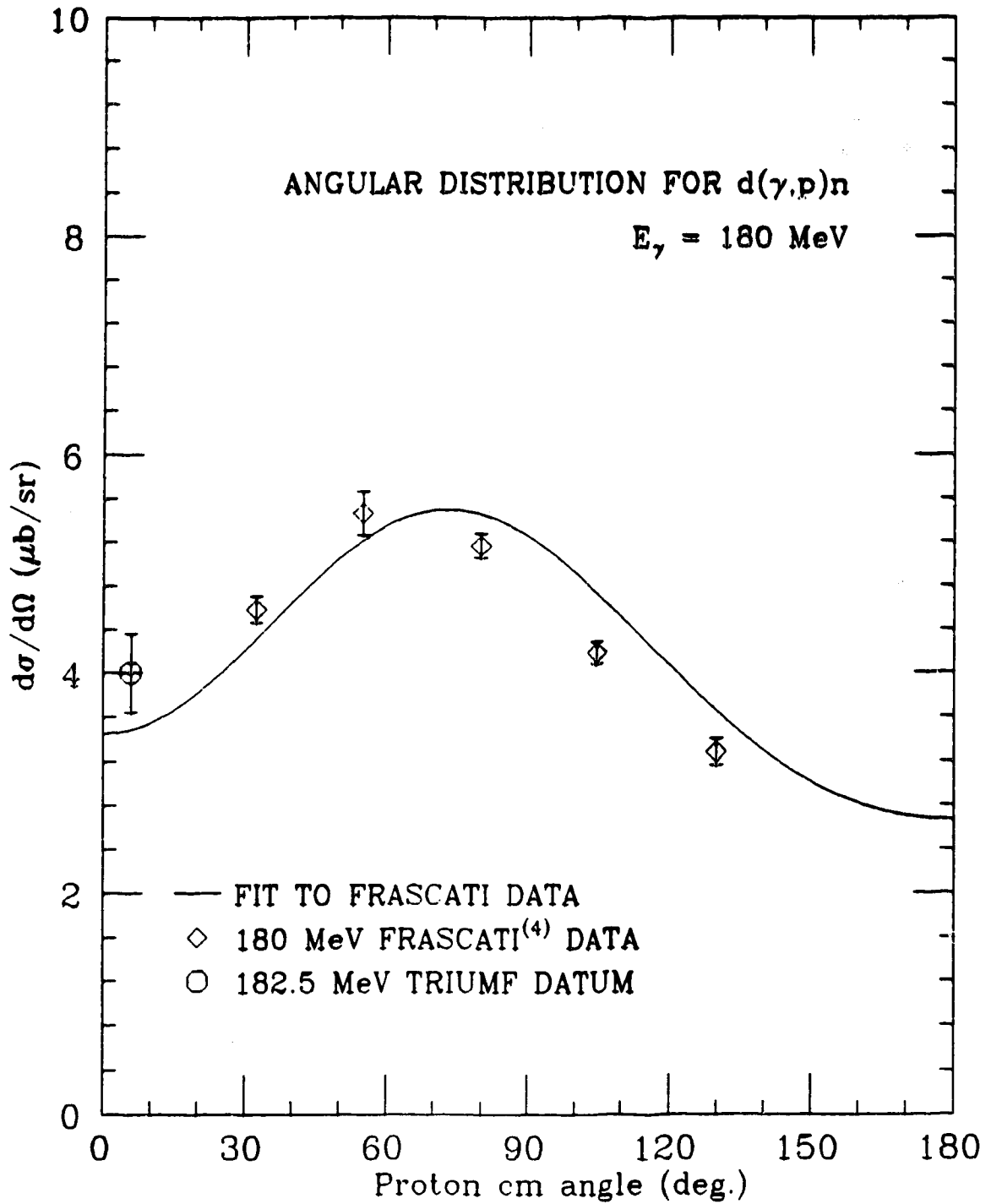


Figure 5.13: A zero degree cross-section prediction was obtained from this experiment's 182.5 MeV datum by extrapolating along the Frascati 180 MeV fit.

#### V.4 SUMMARY AND DISCUSSION OF SYSTEMATIC ERRORS

Figure 5.14 plots our data, extrapolated to zero degrees, along with all the other measurements of the zero degree photo-disintegration cross-section which are available at this time. Clearly our new data agrees passably well with the other data above pion production threshold, and does not appear to suffer any normalisation error with respect to the Mainz data set below the pion production threshold.

Because the normalisation of our results was the elastic scattering cross-section, further improvements to the experimental data for this reaction will lead automatically to a refinement of our data. At present a systematic error in our results of perhaps 3% is attributable to this source - that being the approximate difference between the average of the available  $p(n,p)n$  results, corrected for energy and angle, and the phase shift result at  $180^\circ$  which is the SAID prediction. Figure 5.15 shows the degree of scatter of experimental results in the neighborhood of 410 MeV. At the present time (January 1989) the analysis of TRIUMF experiment 433 (A. Miller et al.), an effort to directly measure the  $p(n,p)n$  elastic scattering cross-sections at  $180^\circ$  in the medium energies, is near completion. The data from this experiment should allow us to revise our  $d(\gamma,p)n$  results and hopefully reduce the quoted 3% systematic error.

The assumption that the  $(n,p)$  and  $(n,d)$  quasi-free cross-sections on carbon scaled with the free cross-sections worked well but gave slightly low estimations of the deuteron tail structure (as illustrated in figure 5.7, for example). Since this involved at most 10% of what was at most at 5% correction, this underestimation is not serious.

Other systematic errors already discussed are those involved in the extrapolation of the data to zero degrees, which depends on how well the shape of the

$p(n,d)\gamma$  cross-section is known close to  $0^\circ$ , the effect of the scintillator time and energy cuts and a possible uncertainty in the region of perfectly flat acceptance to the focal plane. None of these errors are likely to be as large than the statistical error at each energy.

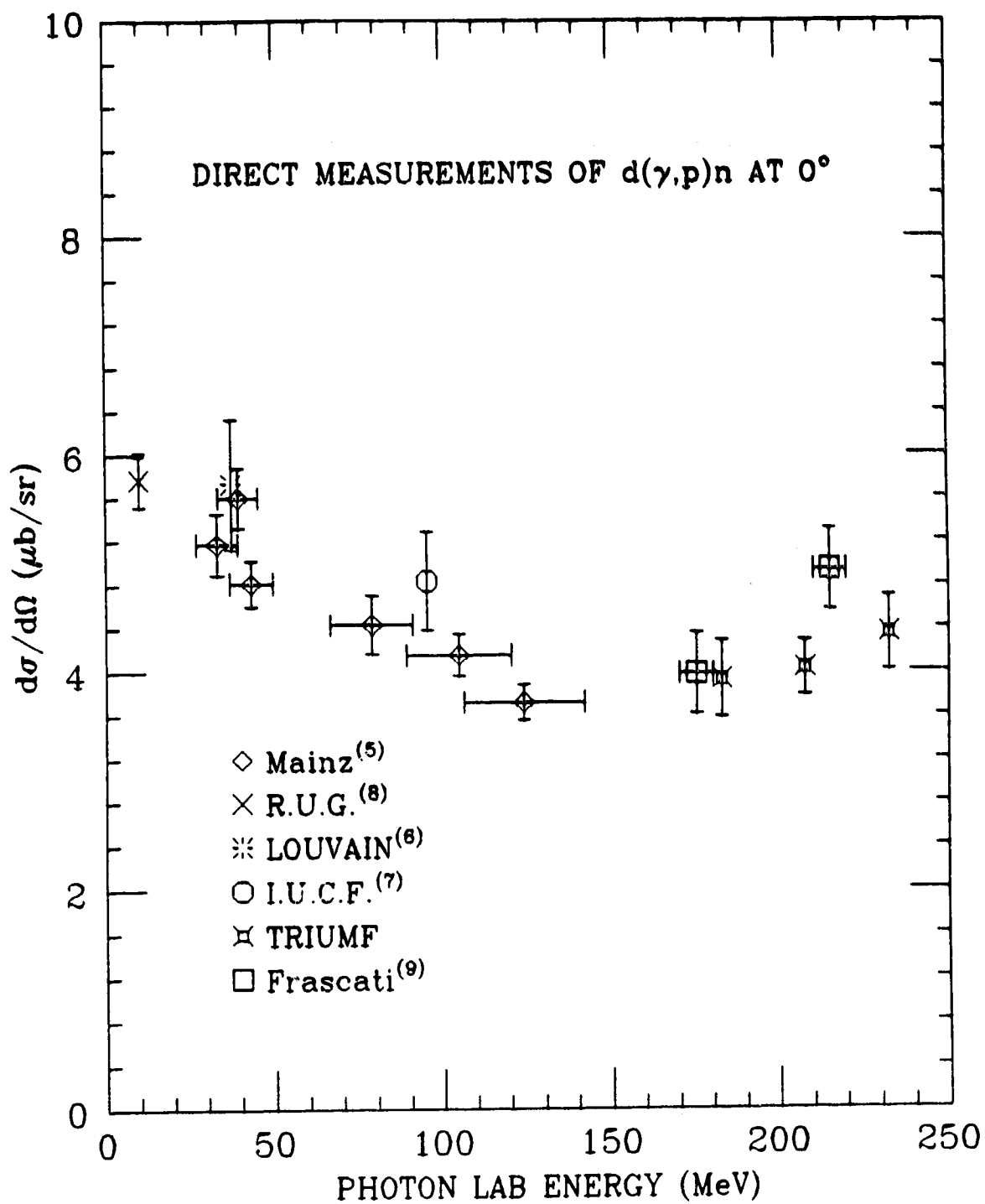


Figure 5.14: The world data set for  $d(\gamma,p)n$  at  $0^\circ$ . Both disintegration and capture measurements are included in the data. Our results are labelled as TRIUMF.



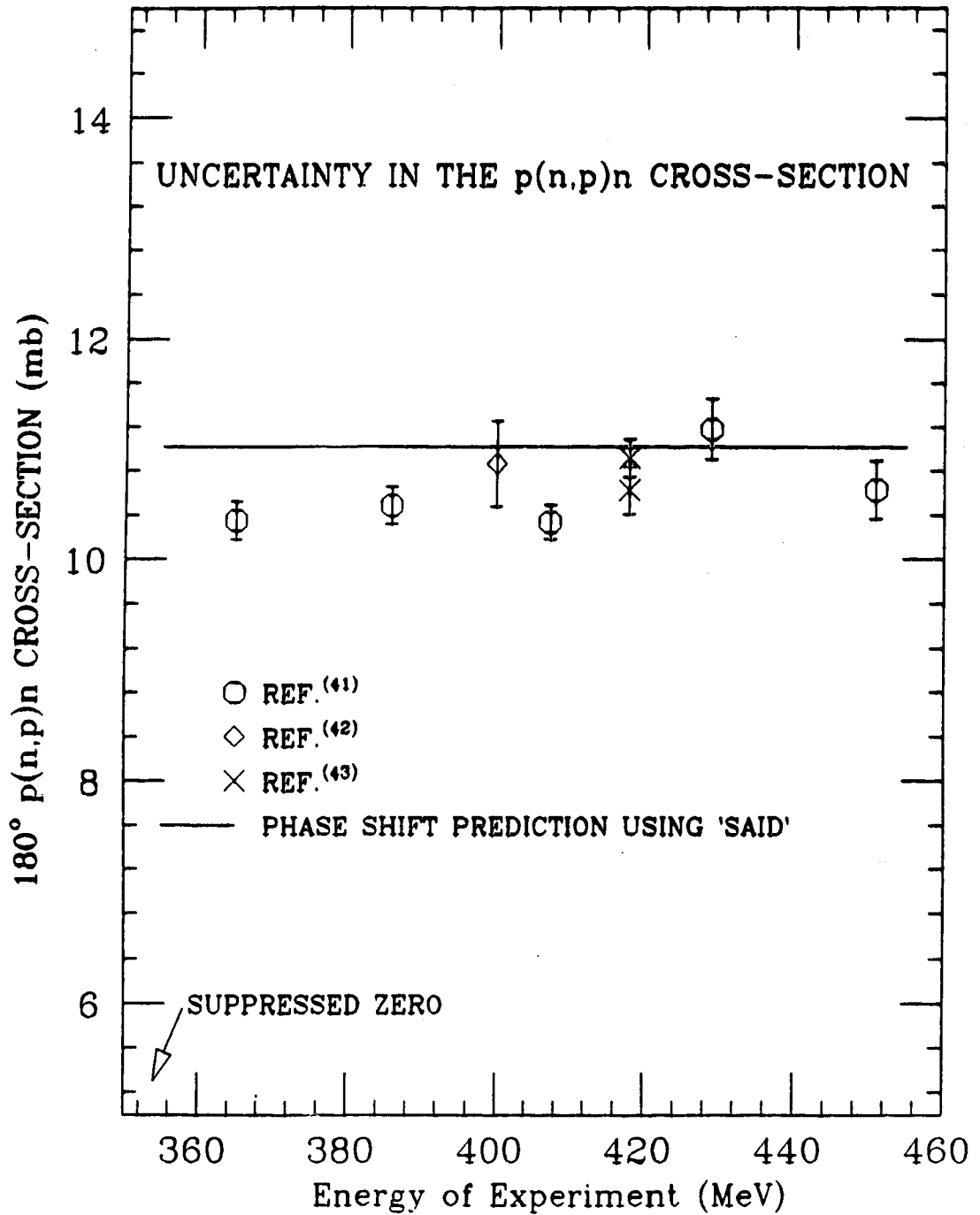


FIG 5.15 : The experimental data for p(n,p)n within 50 MeV of 410 MeV and 20° of 180° are used to give predictions for 410 MeV/180° using the SAID energy/angle dependences as extrapolating functions. The SAID 410 MeV, 180° value is shown by the horizontal line.

## CHAPTER VI SUMMARY AND CONCLUSIONS

### VI.1 MODELS OF $d(\gamma,p)n$ ABOVE THE $\pi^0$ PRODUCTION THRESHOLD

Theoretical work on the deuteron photo-disintegration amplitudes above the  $\pi^0$  production energy threshold has been sparse due to the increasing complexity of the calculation in this regime and by the lack of experimental data. Disregarding the classical calculation, shown in figure 2.3, which was never intended to be extended into the high energy regime, there currently exist three calculations by three prominent nuclear physics theory groups: Leidemann and Arenhövel<sup>(29)(44)</sup> (note that Wilhelm et al., Ref. 44, are part of this group), Hwang et al.<sup>(45)</sup>, and Laget<sup>(16)</sup>. In figure 6.1 the results of these three groups are superimposed over the  $d(\gamma,p)n$  data from Frascati<sup>(10)</sup> and the data which is the result of this work.

The calculation based on the theory of Leidemann and Arenhövel<sup>(29)</sup> is a coupled channels (CC) approach. The coupled equations

$$\left[ \frac{p^2}{2\mu_{NN}} + V_{NN} - E \right] \Psi_{NN} = -V_{NN,N\Delta} \Psi_{N\Delta}$$

$$\left[ \frac{p^2}{2\mu_{N\Delta}} + (M_{\Delta} - M_N) + V_{N\Delta} - E \right] \Psi_{N\Delta} = -V_{N\Delta,NN} \Psi_{NN} \quad (\text{VI-1})$$

linking the nucleon-delta and nucleon-nucleon components of the nuclear wavefunction may be solved in the impulse approximation (IA) by first formally inverting the second equation,

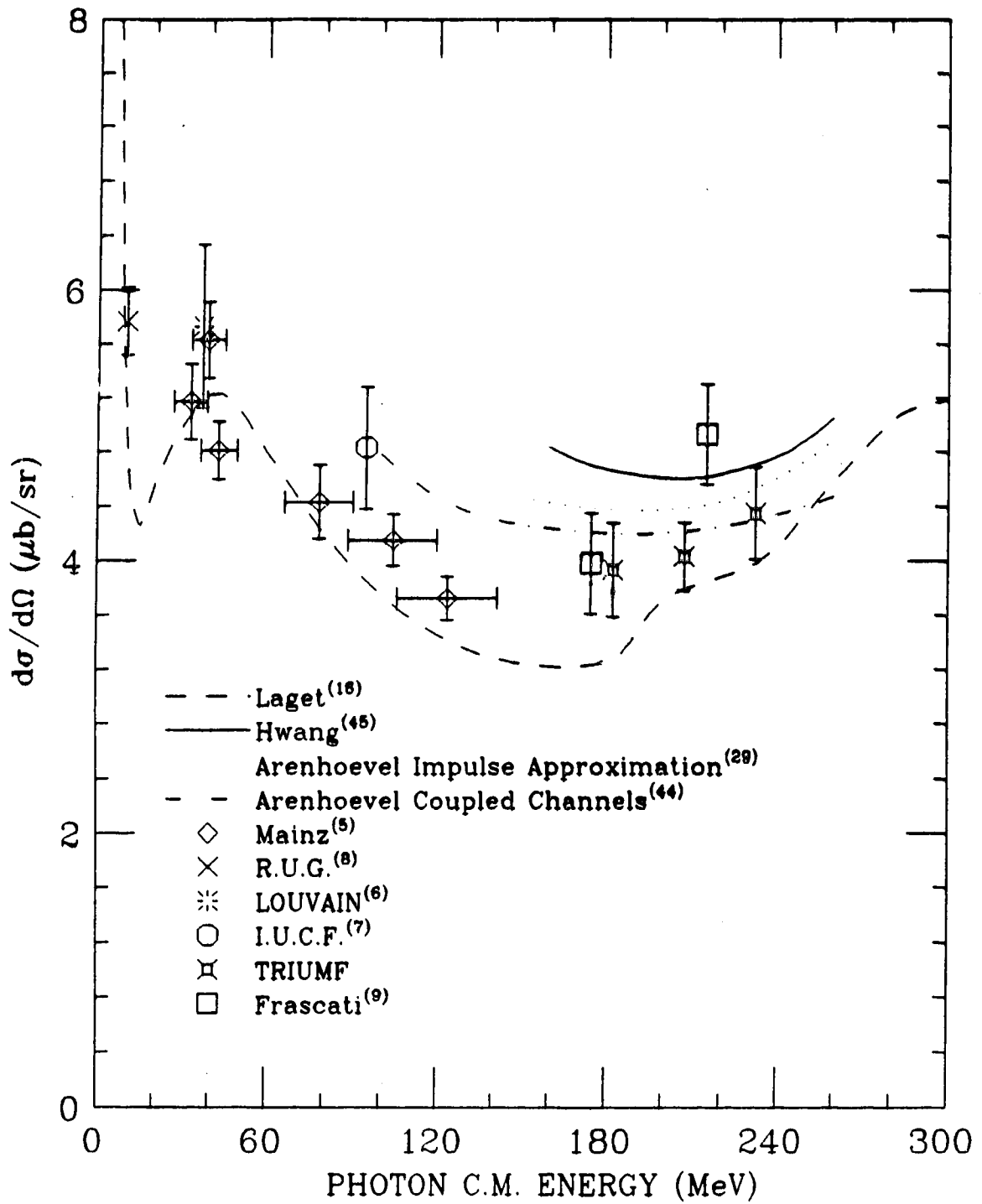


FIG 6.1 :  $d(\gamma,p)n$  Calculations Above the  $\pi^0$  Production Threshold by Various Authors.

$$\Psi_{N\Delta} = \frac{-1}{(H_{N\Delta} - E)} V_{N\Delta, NN} \Psi_{NN} \quad (\text{VI-2})$$

and then solving it by calculating an NN wavefunction based on a realistic potential (Leidemann and Arenhövel used the RSC potential) and also neglecting the  $V_{N\Delta}$  term in the Hamiltonian. At higher energies a full CC calculation is necessary since the  $N\Delta$  wavefunction may no longer be treated perturbatively.  $\Delta\Delta$  channels, transitions between  $N\Delta$  channels are included in the Ref. 29 calculation. In Ref. 44, the spin-orbit relativistic correction is added to this calculation.

Hwang et al.<sup>(45)</sup> made a thorough study of MEC contributions to the NN wavefunction. In particular they found that 'energy transfer terms', terms in the Lagrangian which included the energy of the exchanged meson (in addition to its mass-energy) and which are generally ignored at lower energies because of the dominance of the meson mass, gave significant contributions to the cross-section at all energies and angles. These effects were particularly important in the pion exchange (two body axial current) pieces of the Lagrangian. Hwang et al.<sup>(45)</sup> studied the importance of energy transfer terms in the denominators (propagator only) and numerators (propagator and vertex function) and found that the second class was primarily responsible for a significant increase in photo-disintegration amplitude above the pion production threshold (see figure 6.1). Although this type of investigation is exactly the type of theoretical reconsideration that the high energy  $d(\gamma, p)n$  experiments were meant to stimulate, a word of caution is necessary here. While the zero degree cross-section appears to be reasonably well described, this is attained by a theory which fits the  $90^\circ$  cross-section, as well as the rest of the angular distribution, very poorly. This may be the result of either poorly understood approximations in the MEC theory itself or kinematic considerations which have yet to be included.

The third serious calculation of the zero degree photo-disintegration is one by J.M. Laget<sup>(16)</sup>, who uses a purely diagrammatic approach. The theoretical curve in figure 6.1 illustrates his results in a calculation which goes up to second order in the number of exchanged mesons. This approach is very attractive because of the reduction of phenomenological considerations, but it is problematical whether the divergences which always result in this treatment of strong interaction physics can be dealt with correctly at this stage of our understanding. Nevertheless, this procedure is to be encouraged, if only because of the intuitive comprehension one can achieve from the explicit pairing of reaction amplitude and the physical process involved.

## VI.2 CONCLUSIONS

### VI.2.1 Theoretical considerations

At this point it is useful to comment on the agreement between our results and the theoretical treatments discussed in VI.1. Clearly, none of the four plotted theoretical curves may be eliminated on the basis of our results. However, the curve of ref.<sup>(45)</sup> appears to be systematically too high, while ref.<sup>(16)</sup> is probably too low. Ref.<sup>(44)</sup> appears to provide the best description of the available data. It appears that no theory which significantly overestimates the low energy data is likely to be consistent with the higher energy results of Frascati and this experiment, so in this respect the lower energy results are supported by the latest data. However, some points linking the lower energy results of Mainz with the higher energy results of Frascati and this experiment are desirable. Also, a measurement of both the deuteron photo-disintegration reaction and its inverse at some high energy (say 350 MeV c.m.) would be interesting to test whether the apparent small divergence between the Frascati results and the TRIUMF results is due to a possible failure of detailed balance, or, more likely, due to random variation in values or systematic errors in one or the other of the experiments.

### VI.2.2 Experimental considerations

One important consideration highlighted by the performance of this experiment was the high background created by (n,d) reactions on nuclei in experimental equipment (particularly carbon in scintillator material). Unfortunately the lack of differential cross-section measurements for such interactions was an impediment to the interpretation of our results. Recently many previously poorly known (n,p) cross-sections have been measured by groups working on (for instance) the CHARGEEX/MRS facility at TRIUMF. It is to be suggested that a systematic

measurements of (n,d) cross-sections, or at least of the C(n,d)X angular distribution would be a big asset to future experimenters.

We found that the placement of thin scintillators inside the cold gas region of the LH<sub>2</sub> target, and then viewing the light output by means of the air-periscope assembly described in detail in chapter II and appendix A, was quite useful in the reduction of the backgrounds discussed above. The drop in light output at liquid hydrogen temperatures was not as great as had been feared. although the light output for 360 - 460 MeV protons was too low to be useful. An improvement in the light collection technique should be possible, and might result in a very useful system for the performance of experiments where it is essential to have a minimum of material in the beamline.

**REFERENCES**

- 1) H. Urey, F. Brickwedde and G. Murphy, Phys. Rev. **40** (1932) 1
- 2) P. Marmier and Eric Sheldon, Physics of Nuclei and Particles vol. II,  
ACADEMIC PRESS, New York, 1970, p. 1073
- 3) F. Partovi, Ann. of Phys. **27** (1964) 79
- 4) E. De Sanctis, M. Anginolfi, G.P. Capitani, P. Corvisiero, P. Di Giacomo, C. Guaraldo, V. Lucherini, E. Polli, A.R. Redon, G. Ricco, M. Sanzone and A. Zucchiatti, Phys. Rev. **C34** (1986) 413
- 5) R.J.Hughes, A. Zieger, H. Wäffler and B. Ziegler, Nucl. Phys. **A267** (1976) 329.
- 6) J.F. Gilot, A.Bol, P. Leleux, P. Lipnik and P. Macq, Phys. Rev. Lett. **47** (1981) 304
- 7) H.O. Meyer, J.R. Hall, M. Hugi, H.J. Karwoski, R.E. Pollock and P. Schwandt, Phys. Rev. **C31** (1985) 309
- 8) A. De Graeve et al., Interim report of the Nuclear Physics Laboratory - RUG, Ghent, Belgium, Aug. (1986)
- 9) A. Zieger, P. Grewer and B. Ziegler, Few Body Systems **1** (1986) 135
- 10) P.L. Sandri E. De Sanctis, M. Anghinolfi, N. Bianchi, G.P. Capitani, P. Corvisiero, C. Guaraldo, V. Lucherini, V. Muccifora, E. Pollii, A.R. Reolon, G. Ricco, P. Rossi, M. Sanzone and M. Taiuti, Phys. Rev. Lett. **59** (1987) 2543
- 11) N.L. Rodning and L.D. Knudson, Phys. Rev. Lett. **57** (1986) 2248
- 12) J.L. Friar, B.F. Gibson and G.L. Payne, Phys. Rev. **C30** (1984) 669
- 13) N.L. Rodning, Private communication (1988)
- 14) A.J.F Siegert, Phys. Rev. **52** (1937) 787
- 15) E. Hadjimichael, Phys. Lett. **85B** (1979) 17
- 16) J.M. Laget, Can. Jour. Phys. **62** (1984) 1046, and private communication
- 17) F. Khanna and R. Dymarz, Private communication (1987)



- 18) W. Jaus and W.S. Woolcock, Nucl. Phys. **A431** (1984) 669
- 19) W. Jaus and W.S. Woolcock, Proceedings of the IX'th International Conference on Particles and Nuclei, Kyoto, 1987
- 20) J.M. Greben and R.M. Woloshyn, Jour. of Phys. **G9** (1983) 643
- 21) M. Hugi, J.M. Cameron, M. Ahmad, J. Collot, G. Gaillard, J.S. Wesick, G.W.R. Edwards, H. Fielding, N.E. Davison, D.A. Hutcheon, R. Abegg, C.A. Miller, P. Kitching, I.J. Van Heerden, Nucl. Phys. **A472** (1987) 701
- 22) J.M. Cameron, C.A. Davis, H. Fielding, P. Kitching, J. Pasos, J. Soukup, J. Uegaki, J. Wesick, H.S. Wilson, R. Abegg, D.A. Hutcheon, C.A. Miller, A.W. Stetz, I.J. Van Heerden, Nucl. Phys. **A458** (1986) 637
- 23) J.M. Laget, Nucl. Phys. **A312** (1978) 265
- 24) A. Cambi, B. Mosconi and P. Ricci, Phys. Rev. Lett. **48** (1982) 462
- 25) J.D. Bjorken and S.D. Drell, Relativistic Quantum Mechanics, McGraw-Hill (1964) 51
- 26) A. Cambi, B. Mosconi and P. Ricci, Jour. Phys. **G10** (1984) L11
- 27) W-Y. Hwang, J.T. Londergan and G.E. Walker, Ann. of Phys. **149** (1983) 335
- 28) M. Rustgi, R. Nunemaker and R. Sharma, Nuovo Cim. **A77** (1983) 317
- 29) W. Leidemann and H. Arenhövel, Phys. Lett. **139B** (1984) 22
- 30) H.T. Williams, Phys. Rev. **C31** (1985) 2297
- 31) H. Behrends and C. Fronsdal, Phys. Rev. **109** (1957) 345
- 32) C.A. Miller et al., The TRIUMF Medium Resolution Spectrometer, submitted to Nucl. Instr. and Meth. (1988)
- 33) R. Helmer, TRIUMF Charge Exchange Facility, Can. Jour. Phys. **65** (1987) 588
- 34) J. Tinsley and J. Rogers, Introduction to DACS, TRIUMF internal report TRI-DN-84-28
- 35) D. Frekers, The LISA Data Analysis Program, TRIUMF (unpublished)
- 36) TRIUMF Kinematics Handbook, equation VII-1

- 37) C. Kost, P. Bennet, A. Haynes and the TRIUMF programming group, OPDATA, TRIUMF (unpublished)
- 38) G. Jones, AIP Conference Proc. (Ed. R.D. Bent) **79** (1982), 15-36
- 39) J. Arends, H.J. Gasson, A. Hegerath, B. Mecking, G. Noldeke, P. Pienzel, T. Reichelt, A. Voswinkel and W.W. Sapp, Nucl. Phys. **A412** (1981) 509
- 40) K. Baba, I. Endo, H. Fukuma, K. Inoue, T. Kawamoto, T. Ohsugi, Y. Sumi, T. Takeshita, S. Uehara, Y. Yano and T. Maki, Phys. Rev. Lett. **48** (1982) 729 and Phys. Rev. **C28** (1983) 286
- 41) B.E. Bonner, J.E. Simmons, C.L. Hollas, C.R. Newsom, P.J. Riley, C. Glass and M. Jain, Phys. Rev. Lett. **41** (1978) 1200
- 42) A.J. Hartzler, R.T. Siegel and W. Opitz, Phys. Rev. **95** (1954) 591
- 43) R. Keeler, R. Dubois, E. Auld, D.A. Axen, M. Comyn, G. Ludgate, L. Robertson, D. Bugg, J. Edgington, W. Gibson, A. Clough, N. Stewart and B. Dieterle, Nucl. Phys. **A377** (1982) 529
- 44) P. Wilhelm et al., Few Body Systems **4** (1988) 55, and private communication
- 45) W-Y.P. Hwang and G.E. Walker, Ann. of Phys. **159** (1985) 118
- 46) G.F. Knoll, Radiation Detection and Measurement, WILEY, New York, 1979

## APPENDIX A IN SITU TESTING OF THE LH<sub>2</sub> SCINTILLATORS

This appendix contains a short description of the design and testing of the system consisting of two thin scintillators placed inside the cold gas region of the LH<sub>2</sub> target, and the open light 'periscopes' which were used to collect the light emanating from these scintillators and direct it into a phototube.

The scintillators and reflective mylar periscopes were installed inside the LH<sub>2</sub> target while it was 'warm' (not containing H<sub>2</sub>) and the target cell was then irradiated with a Strontium-90 beta source. Signals from the scintillators were examined in coincidence with signals from a 1/16" scintillator placed on the opposite side of the LH<sub>2</sub> target (see fig. A.1). The electrons from the source, emitted in a distribution with a high energy end-point of 0.54 MeV, lose energy at a rate of approximately 2 MeV per gm/cm<sup>2</sup> in the scintillators, corresponding to ~ 0.05 MeV of deposited energy in the 0.01" scintillators. For plastic scintillation materials (i.e. polystyrene) 50 keV of deposited energy should yield, on the average, 500 photons. A photon/photo-electron ratio of 23% is typical, so we would expect a yield of approximately 125 photo-electrons if we had 100% collection efficiency. However, in the experimental set-up, the scintillators are cooled to close to liquid hydrogen temperatures. This inhibits energy transfer between molecules with a subsequent degradation of the scintillation mechanism<sup>(46)</sup>. Actual photon yield at low temperatures will therefore be somewhat less than optimum.

For the actual yield we first observed the scintillator with the source absent and interpreted the observed energy peak as being due to noise corresponding to the random ejection of a single electron from the tube's photo-cathode. We then observed the energy spectrum with the source present and calculated the average number of

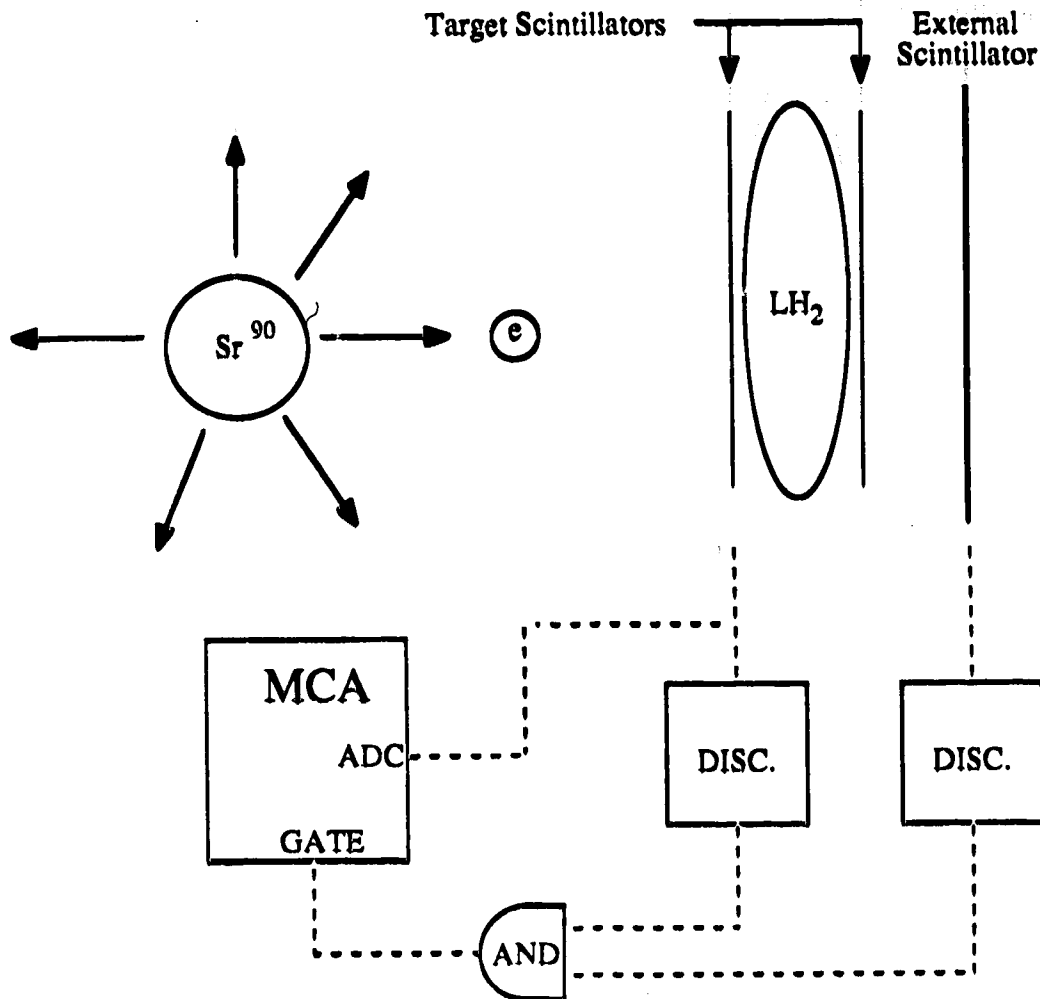


Figure A.1 : Set-up for Testing of the Scintillators Inside the  $\text{LH}_2$  Target. The component labelled MCA is a multi-channel analyser.

photons reaching the photo-cathode by peak shift in the MCA spectrum. Table A.1 contains the relevant data. For comparison, this test was done both with and without the sanding of the scintillator side facing the target cell.

Examining Table A.1 we write, for the sanded scintillator case,

$$C_0 + 750 \cdot P_1 = 210$$

**Table A.1 - Results of In Situ Testing of the Scintillators  
Inside the Liquid Hydrogen Target**

**WITHOUT SANDING OF ONE SCINTILLATOR SIDE**

|                        | <u>MCR Scale</u> | <u>Peak Position</u> |
|------------------------|------------------|----------------------|
| Single Photo-electrons | 500x1.5          | Ch. 210              |
| Source Present         | 50x1.5           | Ch. 270              |

**AFTER SANDING OF ONE SCINTILLATOR SIDE**

|                        | <u>MCR Scale</u> | <u>Peak Position</u> |
|------------------------|------------------|----------------------|
| Single Photo-electrons | 500x1.5          | Ch. 210              |
| Source Present         | 50x1.5           | Ch. 434              |
| Source Present         | 20x1.5           | Ch. 178              |

$$C_0 + 75 \cdot P_S = 434$$

$$C_0 + 30 \cdot P_S = 178$$

$C_0$  is the unknown MCR offset channel and  $P_1$  and  $P_S$  are the peaks for single photo-electron events and the average number of photo-electrons produced when the source was present, respectively. These three equations may be solved to find the number of photo-electrons produced when the source was present,

$$\frac{P_S}{P_1} = 21.12.$$

This indicates an average of 21.12 photo-electrons created per electron from the  $^{90}\text{Sr}$  source. For the unsanded scintillator case, with the same MCR offset channel, the results were

$$C_0 + 750 \cdot P_1 = 210$$

$$C_0 + 75 \cdot P_S = 270$$

$$\frac{P_S}{P_1} = 12.97.$$

The sanding can therefore be seen to have increased the light yield by more than 50%.

The efficiency of our collection system may be estimated by dividing 21.12 in to  $500 \cdot 0.23$  to get approximately 20%. Although this collection efficiency is somewhat lower than the theoretical maximum of 50%, it is not unreasonable for a practical situation. For instance, we estimated an efficiency of 35% would be obtained

by connecting the target cell window with the top of the lightpipe with a truncated elliptical cone. This estimate was made by computer raytracing using the expected light angle distribution from the side of the scintillator

$$I(\theta) = \alpha \frac{\sin(\theta)\cos(\theta)}{\sqrt{n^2 - \sin^2(\theta)}} \quad (\text{A-1})$$

$\alpha$  is the normalisation, equal to  $2.85*(1-R_s/2)$  if  $R_s$  is the reflectivity of the specular surface facing the LH<sub>2</sub> target.  $\theta$  is the angle from the normal to the scintillator side, and  $n$  is the scintillator index of refraction (approximately 1.6).

## APPENDIX B DETERMINATION OF THE MRS ACCEPTANCE

Using the position information from the two wire chambers at the entrance to the MRS, the paths of particles entering the MRS were projected back to a plane perpendicular to the beamline axis at the center of the LH<sub>2</sub> target - yielding co-ordinates XI (displacement in the bend plane of the spectrometer) and YI (displacement perpendicular to the spectrometer bend plane). The MRS entrance angle could also be computed from the FEC information, giving TFEC (angle in the bend plane), and PFEC (the angle perpendicular to the bend plane). These four co-ordinates, along with the particle momentum, define the 5-dimensional phase space of the MRS spectrometer, and the volume of uniform population density of events defines the MRS 'good' acceptance. Naturally it was important, for simultaneous comparison between reactions of different momenta, to restrict ourselves to a sub-volume of the MRS good acceptance region which had a uniform 4-D volume size at each momentum value.

A special experimental run was done, looking at protons from the  $p(n,p)n$  reaction in which the MRS dipole/quadrupole fields were successively adjusted to move the proton peak across the focal plane. This procedure exactly imitated looking at particles of different momenta. The elimination of some of the complications present in the actual experiment, such as differing Jacobians and cross-sections, allowed us to directly compare the probabilities for particle transmission through the MRS to different points on the focal plane for a given set of initial angles and positions at the entrance.

We assumed that there would be no correlation in the MRS acceptance between variables in the bend plane (XI,TFEC) and variables perpendicular to the bend plane (YI,PFEC). The data from the acceptance run was therefore analysed by first



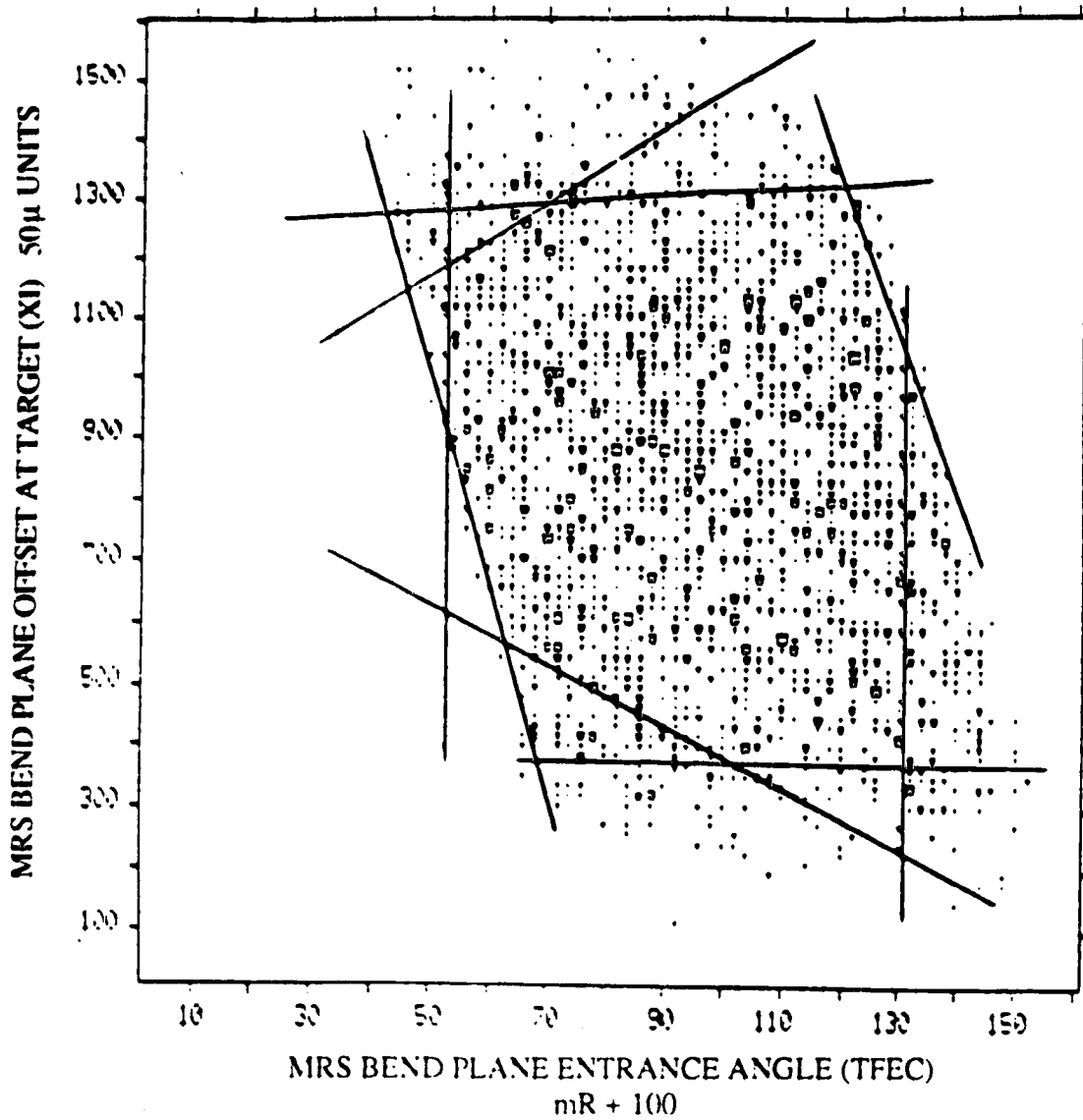


Figure B.1: MRS Bend Plane Acceptance for the RHS of the Focal Plane. The lines indicate the cuts that were made on entrance angle and position.

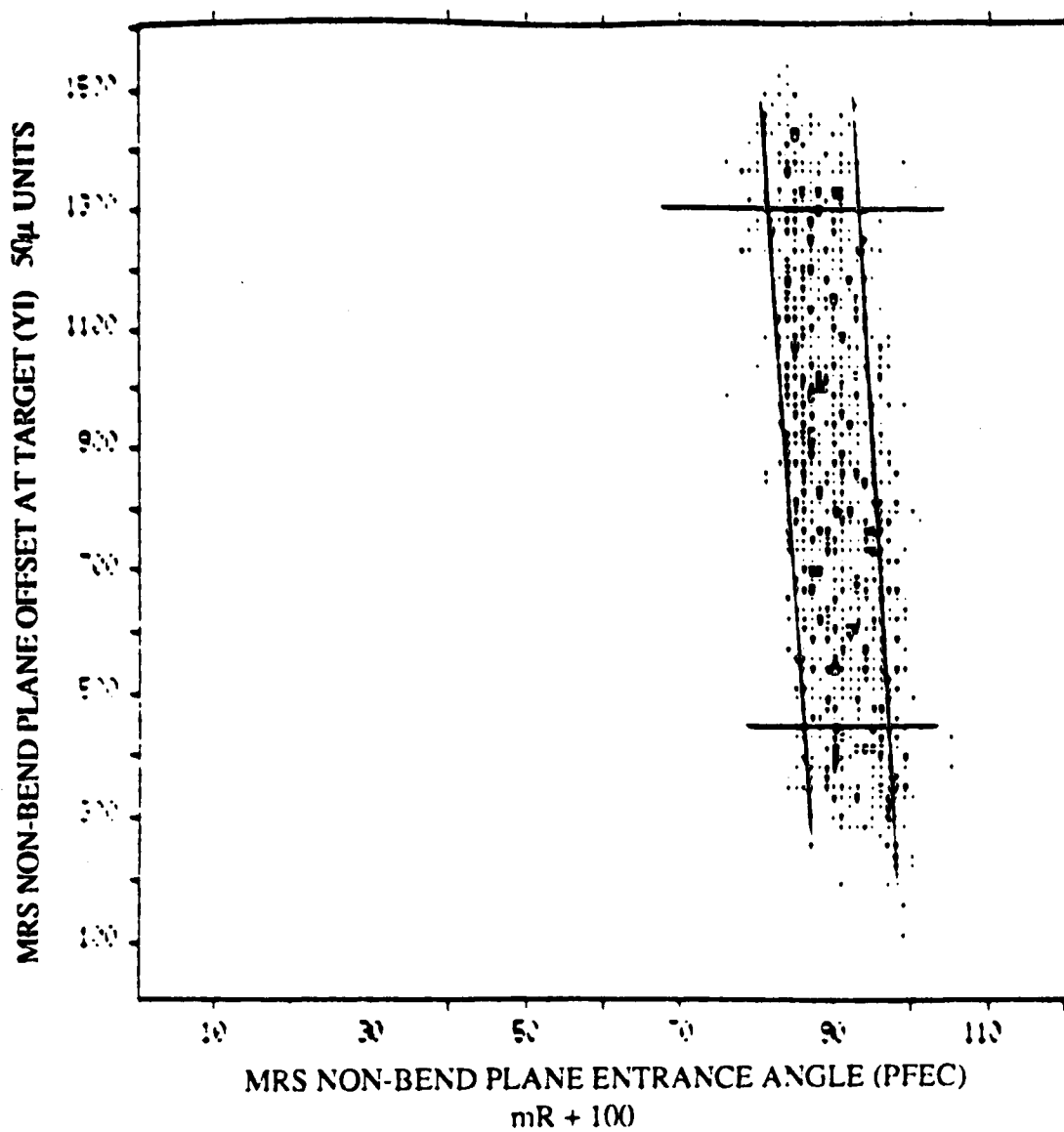


Figure B.2: MRS Non-Bend Plane Acceptance for the RHS of the Focal Plane. The lines indicate the cuts that were made on entrance angle and position.

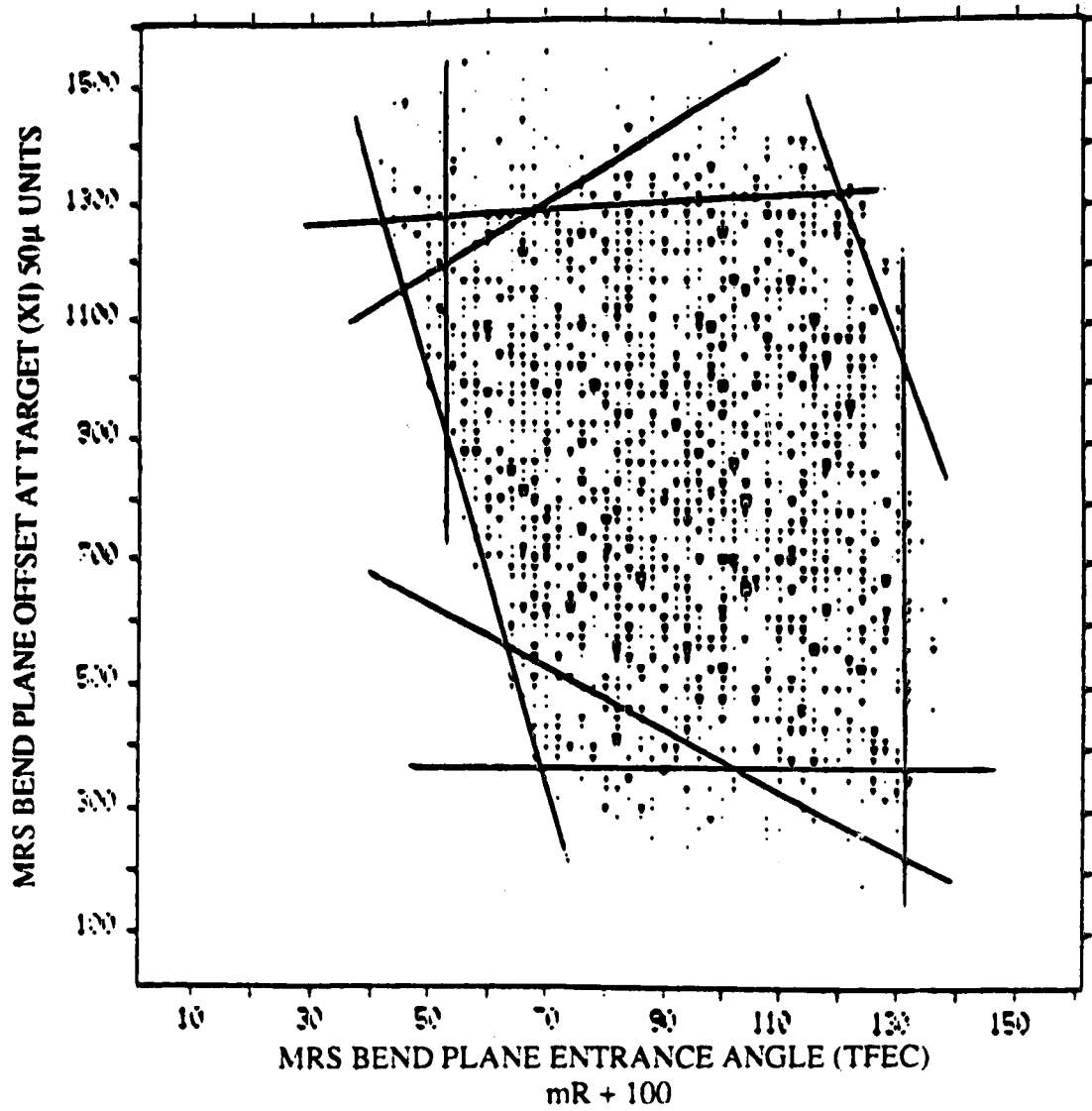


Figure B.3: MRS Bend Plane Acceptance for the LHS of the Focal Plane. The lines indicate the cuts that were made on entrance angle and position.

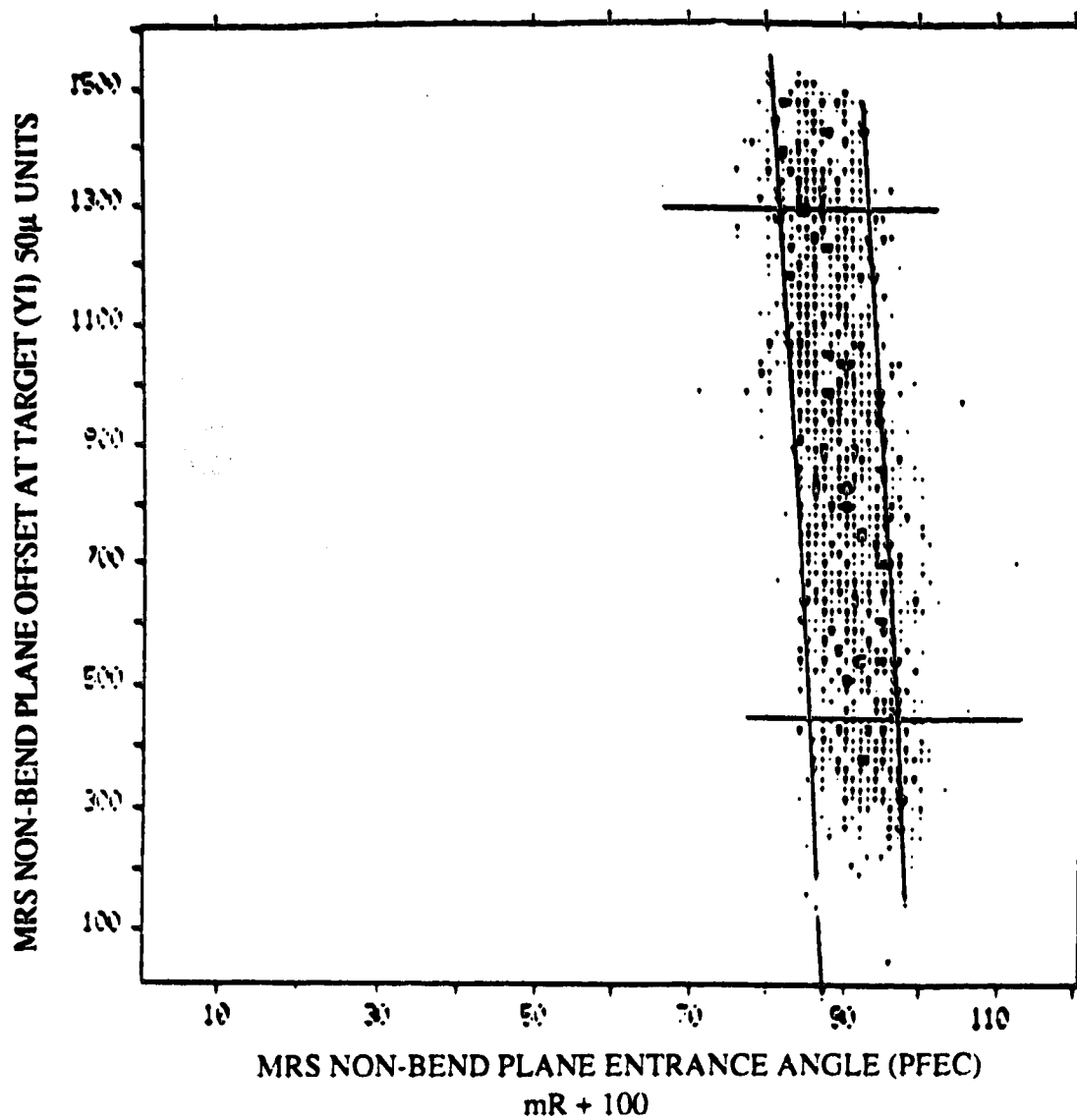


Figure B.4: MRS Non-Bend Plane Acceptance for the LHS of the Focal Plane. The lines indicate the cuts that were made on entrance angle and position.

plotting two 2D histograms, XI vs. TFEC and YI vs. PFEC, for each position on the focal plane. The region of even population was estimated for each one, and the region of uniform acceptance which was common to all the plots was used as our initial estimate of the MRS good acceptance region. Because the acceptance fell off sharply at either end of the focal plane, particularly the high momentum end, we considered only the region of the focal plane relevant to the experiment. Using our estimate of the MRS good acceptance region as a requirement for the particle's initial co-ordinates, the acceptance probability  $A(XF;XI,YI,TFEC,PFEC)$  was computed for each focal plane position as follows

$$A(XF;XI,YI,TFEC,PFEC) = \frac{\text{Events in Peak}}{\text{Integrated Beam Charge}} \times \frac{1}{\lambda}. \quad (\text{B-1})$$

$\lambda$  is the computer livetime for the run under consideration, and was defined as the number of processed events divided by the number of events satisfying the MRS trigger conditions. The beam charge was calculated from the beamline polarimeter scalers as described in chapter III. The plot of  $A$  vs. XFK was then tested for flatness, and this process was repeated by varying the MRS acceptance volume perpendicular to the 3-planes defining its edges until  $A$  was constant with variation in XFK within statistical bounds. The MRS acceptance thus obtained was subsequently used for protons and deuterons in the analysis of the experiment proper. Figures B.1 and B.2 show the final XI/TFEC and YI/PFEC selections superimposed on  $p(n,p)n$  data at the low momentum side of the focal plane. Figure B.3 and B.4 show the same cuts on the high momentum end of the focal plane. The final result of this analysis is the acceptance vs. focal plane position plot of figure B.5.

For the runs at 410 MeV and 460 MeV, the MRS quadrupole was on. This

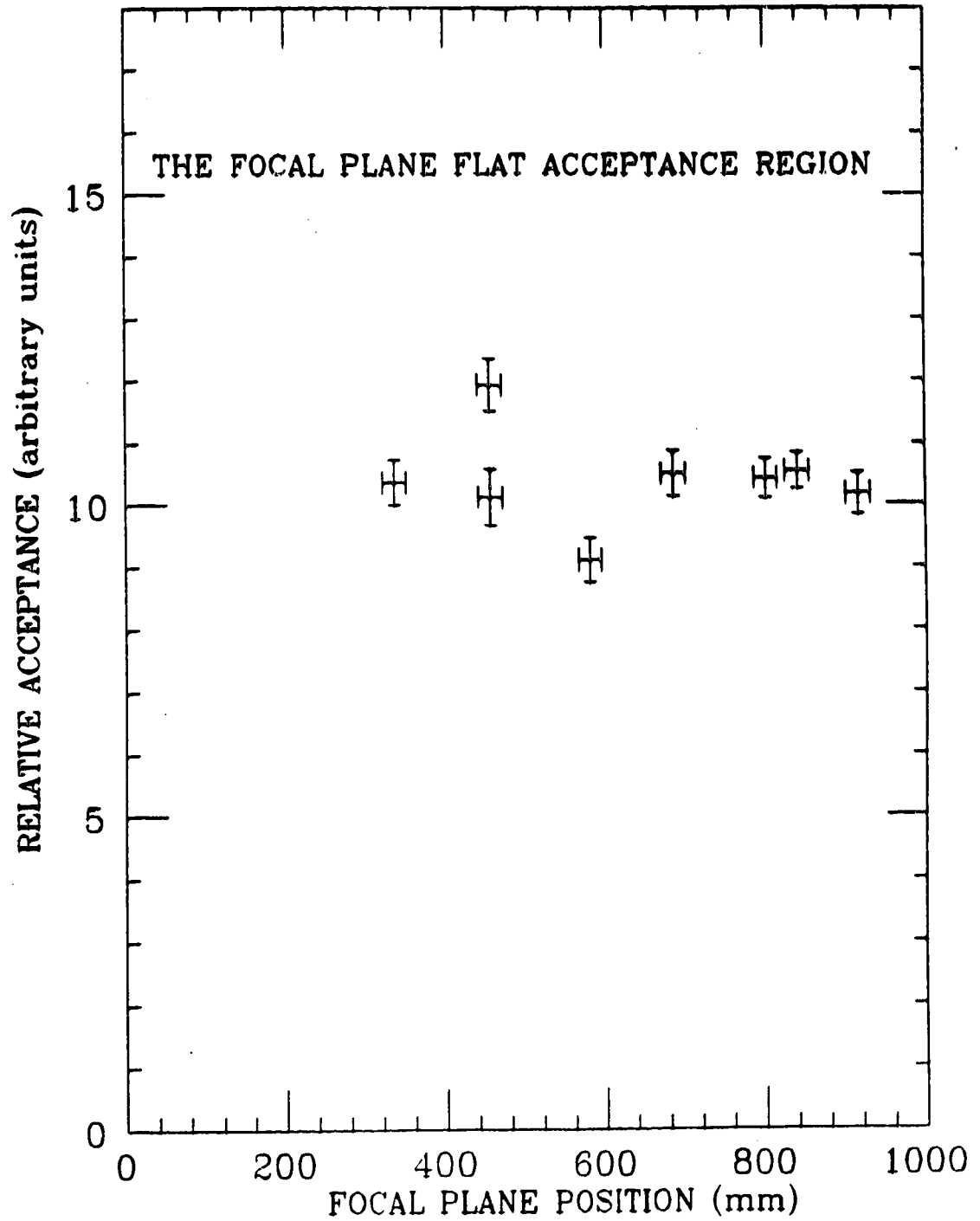


FIG B.5 : The relative transmission to the focal plane for a restricted angle/position acceptance at the MRS entrance for the quadrupole off configuration is shown in this figure.

produced an MRS acceptance different from the 360 MeV case. A separate acceptance run (at a later date) was done with this MRS configuration. It indicated that, for a smaller MRS acceptance than was used for the ZERCON final analysis, the acceptance was quite flat over the relevant region of the focal plane. We extended this result to apply to our larger acceptance by calculating the ratio of numbers of events in the two  $p(n,d)\pi^0$  peaks, one at each side of the focal plane, for successively smaller MRS acceptances. The results of this analysis are shown in figure B.6 and confirm that our selected acceptance region for this configuration was appropriate for the entire relevant region of the focal plane.

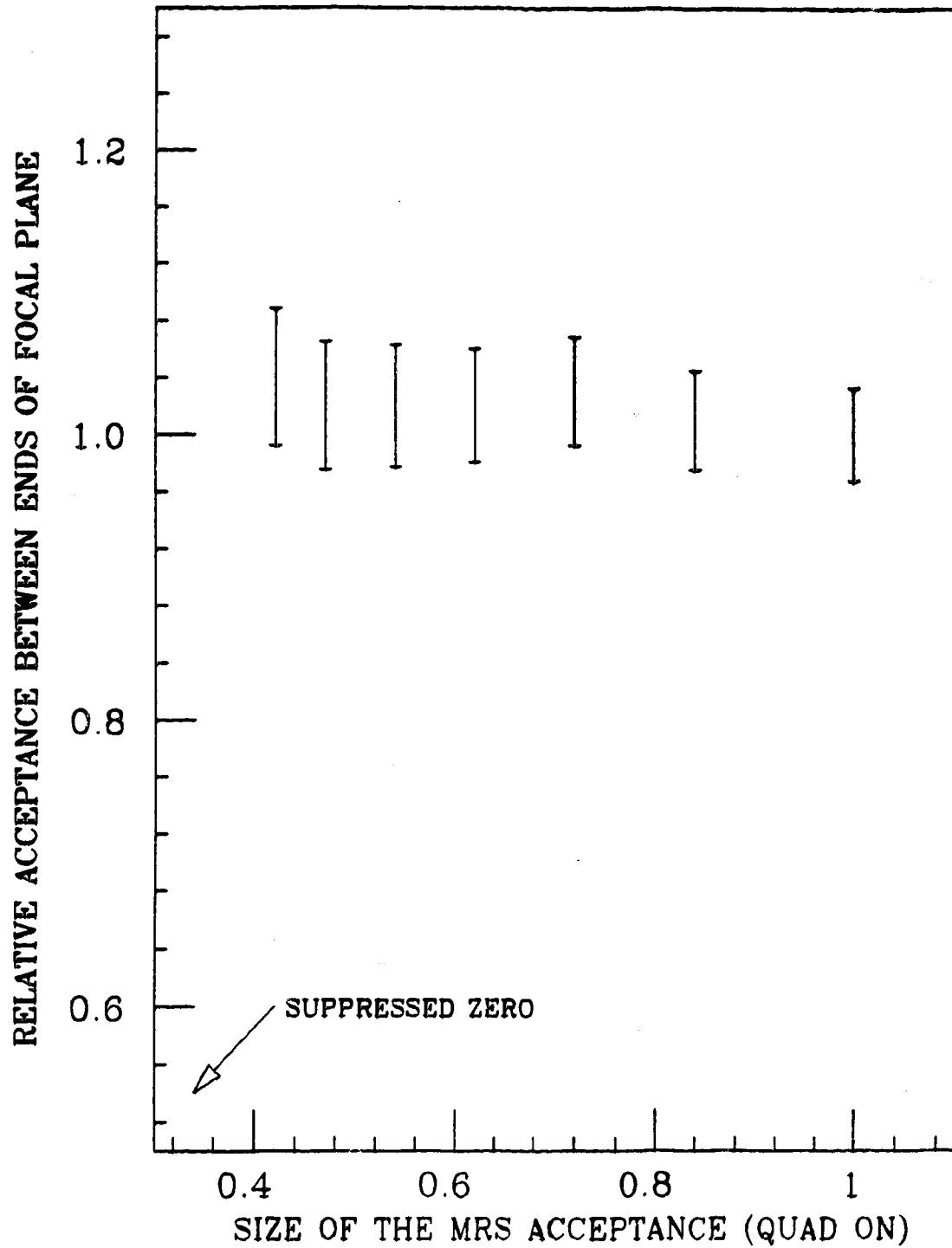


FIG B.6 : The Effect of Variations in Front End Acceptance on Transmission to the Focal Plane. Smaller acceptances than the one we used (size = 1) had the same transmission.



## APPENDIX C RELATIVISTIC KINEMATICS PROGRAMS

```

SUBROUTINE NPDG(RKN,RTHD,PEERO,PRACT)
KINEMATICS PROGRAM FOR N + P -> D + GAMMA
WRITTEN BY G.W.R. EDWARDS, JUNE 1984
C
C RKN - NEUTRON KINETIC ENERGY IN MEV
C RTHD - SCATTERING ANGLE (LAB) IN DEGREES
C PEERO - DIFFERENCE BETWEEN THE DEUTERON MOMENTUM AND THE MOMENTUM OF A
C DEUTERON WHICH WAS PRODUCED AT AN ANGLE RTHD (IN MEV/C)
C PRACT - MOMENTUM OF THE CREATED DEUTERON
C
REAL RKN,RTHD,PEERO,PRACT
REAL KN,MNEUT,MDEUT,GN,BN
REAL KD2,GD2,BD2,KD1,GD1,BD1,BDX,BDY,THD,EG1,EG2,THG1,THG2
REAL THDCM1,THDCM2,THGCM1,THGCM2,PD1,PD2,PG1,PG2,PN
REAL BCM,GCM,BPCM,BNCM,GNCM,GPCM,ECM
REAL KDCM,BDCM,ODCM,EGCM
REAL R,ERAT,T,A,B,C,PI,PD
INTEGER ILOOP
DATA MPROT,MNEUT,PI/938.2796,939.5731,3.14159265358979/
C
KN = RKN
THD = RTHD*PI/180.0
C
ILOOP = 0
MDEUT = MNEUT + MPROT - 2.2247
C
FIRST WE SOLVE THE PROBLEM IN THE CENTER-OF-MASS REFERENCE FRAME
C
GN = 1 + KN/MNEUT
BN = (1-1/GN**2)**.5
C
BCM = GN*BN/(MPROT/MNEUT + GN)
GCM = 1/(1-BCM**2)**.5
C
WORK OUT THE ENERGY AVAILABLE IN THE CM FRAME
C
BPCM = BCM
GPCM = GCM
BNCM = (BN - BCM)/(1-BN*BCM)
GNCM = 1/(1-BNCM**2)**.5
ECM = MPROT*(GPCM - 1) + MNEUT*(GNCM - 1) + 2.2247
C
WORK OUT THE TWO POSSIBLE RECOIL VELOCITIES OF THE DEUTERON IN THE CM
C
ERAT = ECM/MDEUT
R = (1+ERAT**2)
BDCM = (R-1)/(R+1)
GDCM = 1/(1-BDCM**2)**.5
KDCM = (GDCM-1)*MDEUT
EGCM = ECM - KDCM
C
WORK OUT THE CM SCATTERING ANGLES FOR THE DEUTERON
C
T = TAN(THD)
A = (GCM*BDCM)**2 + BDCM**2
B = 2*(GCM*T)**2*BDCM*BCM
C = (GCM*BCM*T)**2 - BDCM**2
C
ARG=B*B-4*A*C
IF(ARG.LT.0) ARG = 0.0
ARG2 = (-B + ARG**.5)/2/A
IF(ARG2.GT.(1.0).OR.ARG2.LT.(-1.0)) ARG2 = .999999
THDCM1 = ACOS(ARG2)
THDCM2 = THDCM1
THGCM1 = THDCM1 - PI
THGCM2 = THDCM2 - PI
C
TRANSFORM THE CM ENERGY TO A LAB ENERGY
C
BDX = (BDCM*COS(THDCM1) + BCM)/(1 + BDCM*BCM*COS(THDCM1))
BDY = BDCM*SIN(THDCM1)/GCM/(1 + BDCM*BCM*COS(THDCM1))
BD1 = (BDX*BDX + BDY*BDY)**.5
GD1 = 1/(1 - BD1**2)**.5
KD1 = (GD1 - 1)*MDEUT
C
BDX = (BDCM*COS(THDCM2) + BCM)/(1 + BDCM*BCM*COS(THDCM2))
BDY = BDCM*SIN(THDCM2)/GCM/(1 + BDCM*BCM*COS(THDCM2))
BD2 = (BDX*BDX + BDY*BDY)**.5
GD2 = 1/(1 - BD2**2)**.5
KD2 = (GD2 - 1)*MDEUT
C
EG1 = EGCM*GCM*(1+BCM*COS(THGCM1))
EG2 = EGCM*GCM*(1+BCM*COS(THGCM2))
C
PN = (KN + MNEUT)*BN
PD1 = (KD1 + MDEUT)*BD1
PG1 = EG1
ARG = (PN - PD1*COS(THD))/PG1
IF(ARG.GT.1.0) ARG = 1.0
IF(ARG.LT.-1.0) ARG = -1.0
THG1 = ACOS(ARG)
C
PD2 = (KD2 + MDEUT)*BD2
PG2 = EG2
ARG = (PN - PD2*COS(THD))/PG2
IF(ARG.GT.1.0) ARG = 1.0
IF(ARG.LT.-1.0) ARG = -1.0
THG2 = ACOS(ARG)
C
CIRCLE BACK TO COMPUTE THE SECOND MOMENTUM
IF(ILOOP.EQ.1) THEN

```

```

      PD = PD1
      IF (PD2.GT.PD) PD=PD2
      PEERO = PD-PDST
ELSE
      PDST = PD1
      IF (PD2.GT.PDST) PDST=PD2
      THD = 0.0
      PREACT = PDST
      LOOP = 1
      GOTO 10
ENDIF
RETURN
END
SUBROUTINE NPDPI(RKN,RTHD,PEERO,PREACT)
C
C KINEMATICS PROGRAM FOR N + P -> D + PION
C WRITTEN BY G.W.R. EDWARDS, JUNE 1984
C
C RKN - NEUTRON KINETIC ENERGY IN MeV
C RTHD - SCATTERING ANGLE (LAB) IN DEGREES
C PEERO - DIFFERENCE BETWEEN THE DEUTERON MOMENTUM AND THE MOMENTUM OF A
C DEUTERON WHICH WAS PRODUCED AT AN ANGLE RTHD (IN MeV/C)
C PREACT - MOMENTUM OF THE CREATED DEUTERON
C
      REAL RKN,RTHD,PEERO,PREACT
      REAL MNEUT,MDEUT,MPION,GN,BN
      REAL KD1,GD1,BD1,KD2,GD2,BD2,BD1,BD2,BD1,BD2,THD
      REAL KQ1,GQ1,BQ1,KQ2,GQ2,BQ2,BQ1,BQ2,THQ1,THQ2
      REAL THDCM1,THDCM2,THDCM1,THDCM2,PD1,PD2,PQ1,PQ2,PN
      REAL BDCM,GDCM,BDCM,GDCM,BDCM,GDCM,ECH
      REAL MPRAT,MRAT,MRAT,MRAT,MRAT,MRAT
      REAL ARG1,ARG2,ARG1,ARG2
      INTEGER I,OUTS
      DATA MPROT,MNEUT,MPION/938.2796,939.5731,134.963/
      DATA PI/3.14159265358979/
C
      KN = RKN
      THD = RTHD*PI/180.0
      LOOP = 0
C
      MDEUT = 1875.628
      MRAT = MPION/MDEUT
C
C FIRST WE SOLVE THE PROBLEM IN THE CENTER-OF-MASS REFERENCE FRAME
C
      GN = 1 + KN/MNEUT
      BN = (1-1/GN**2)**.5
C
      BCM = GN*BN/(MPROT/MNEUT + GN)
      GCM = 1/(1-BCM**2)**.5
C
C WORK OUT THE ENERGY AVAILABLE IN THE CM FRAME
C
      BDCM = BCM
      GDCM = GCM
      BDCM = (BN - BCM)/(1-BN*BCM)
      GDCM = 1/(1-BDCM**2)**.5
      ECH = MPROT*GDCM + MNEUT*GDCM - MDEUT
C
C WORK OUT THE TWO POSSIBLE RECOIL VELOCITIES OF THE DEUTERON IN THE CM
C
      ERAT = ECH/MDEUT
C
      GDCH = 1 + (ERAT**2 - MRAT**2)/2/(ERAT + 1)
      BDCH = (1 - 1/GDCH**2)**.5
      KDCH = (GDCH-1)*MDEUT
      GQCH = (ERAT + GDCH - 1)/MRAT
      BQCH = (1 - 1/GQCH**2)**.5
      KQCH = (GQCH-1)*MPION
C
C WORK OUT THE CM SCATTERING ANGLES FOR THE DEUTERON
C
      T = TAN(THD)
      A = (GCM*T + BDCM)**2 + BDCM**2
      B = 2*(GCM*T)**2 + BDCM*BCH
      C = (GCM*BCH*T)**2 - BDCM**2
C
      ARG = B*B-4*A*C
      IF (ARG.LE.0) ARG = 0.00001
      ARG2 = (-B + ARG**.5)/2/A
      IF (ARG2.GT.(1.0).OR.ARG2.LT.(-1.0)) ARG2 = .999999
      THDCM1 = ACOS(ARG2)
      THDCM2 = ACOS(ARG2)
C
C PREPARE VALUES FOR OUTPUT
C
      THQCH1 = THDCM1 - PI
      THQCH2 = THDCM2 - PI
C
C TRANSFORM THE CM ENERGY TO A LAB ENERGY
C
      BD1 = (BDCM*COS(THDCM1) + BCM)/(1 + BDCM*BCH*COS(THDCM1))
      BD2 = (BDCM*SIN(THDCM1)/GCM)/(1 + BDCM*BCH*COS(THDCM1))
      BD1 = (BD1*BD1 + BD2*BD2)**.5
      GD1 = 1/(1 - BD1**2)**.5
      KD1 = (GD1 - 1)*MDEUT
C
      BD2 = (BDCM*COS(THDCM2) + BCM)/(1 + BDCM*BCH*COS(THDCM2))
      BD1 = (BDCM*SIN(THDCM2)/GCM)/(1 + BDCM*BCH*COS(THDCM2))
      BD2 = (BD2*BD2 + BD1*BD1)**.5
      GD2 = 1/(1 - BD2**2)**.5
      KD2 = (GD2 - 1)*MDEUT
C
      KQ1 = GN*MNEUT + MPROT - GD1*MDEUT - MPION
      GQ1 = 1 + KQ1/MPION
      BQ1 = (1 - 1/GQ1**2)**.5

```

```

C      KO2 = GN*MNEUT + MPROT - GD2*MDEUT - MPION
C      GO2 = 1 + KO2/MPION
C      HQ2 = (1 - 1/GO2**2)**.5
C
C      PN = (KN + MNEUT)*BN
C      PD1 = (KD1 + MDEUT)*BD1
C      PQ1 = (KQ1 + MPION)*BQ1
C      ARG = (PN - PD1*COS(RTHD))/PQ1
C      IF(ARG.GT.1.0) ARG = 1.0
C      IF(ARG.LT.-1.0) ARG = -1.0
C      THQ1 = ACOS(ARG)
C
C      PD2 = (KD2 + MDEUT)*BD2
C      PQ2 = (KQ2 + MPION)*BQ2
C      ARG = (PN - PD2*COS(RTHD))/PQ2
C      IF(ARG.GT.1.0) ARG = 1.0
C      IF(ARG.LT.-1.0) ARG = -1.0
C      THQ2 = ACOS(ARG)
C
C      LOOP BACK FOR THE SECOND MOMENTUM
C
C      IF(ILOOP.EQ.1) THEN
C          PD = PD1
C          IF(PD2.GT.PD) PD = PD2
C          PZERO = PD - PDST
C      ELSE
C          PDST = PD1
C          IF(PD2.GT.PDST) PDST = PD2
C          THD = 0.0
C          PPREACT = PDST
C          ILOOP = 1.0
C          GOTO 10
C      ENDIF
C      RETURN
C      END
C      SUBROUTINE NPMP(RKN,RTHD,PZERO,PPREACT)
C
C      PROGRAM TO CALCULATE THE KINEMATICS FOR ELASTIC NP SCATTERING
C      WRITTEN BY G.W.R. EDWARDS, JUNE 1984
C
C      RKN - NEUTRON KINETIC ENERGY IN MeV
C      RTHD - SCATTERING ANGLE (LAB) IN DEGREES
C      PZERO - DIFFERENCE BETWEEN THE DEUTERON MOMENTUM AND THE MOMENTUM OF A
C      DEUTERON WHICH WAS PRODUCED AT AN ANGLE RTHD (IN MEV/C)
C      PPREACT - MOMENTUM OF THE CREATED DEUTERON
C
C      INTEGER IOUES
C      REAL*4 MPROT,MNEUT,MPROJ,MTARG,PI
C      REAL*4 T,A,B,C,ARG
C      REAL*4 BTX,BTY,BTF,GTFF,KTF,BPF,GPF,KPF,GP,BP,KP
C      REAL*4 PPROJ,PTARG,PINIT
C      REAL*4 THETA,ANGLP,ANGL
C      REAL*4 BCM,GCM,BPCM,GPCM,KPCM,BTCM,GTCH,KTCM
C      DATA MPROT,MNEUT,PI/938.2796,939.5731,3.14159265358979323/
C
C      MTARG = MPROT
C      MPROJ = MNEUT
C
C      KP = RKN
C      ANGLT = RTH*3.1416/180.0
C
C      GP = 1 + KP/MPROJ
C      BP = (1 - 1/GP**2)**.5
C      KP = (GP - 1)*MPROJ
C      PP = GP*BP*MPROJ
C
C      SOLVE IN THE CENTER OF MASS FRAME
C
C      BCM = GP*BP/(MTARG/MPROJ + GP)
C      GCM = 1/(1 - BCM**2)**.5
C      BPCM = (BP - BCM)/(1 - BP*BCM)
C      GPCM = 1/(1 - BPCM**2)**.5
C      KPCM = (GPCM - 1)*MPROJ
C      BTCM = BCM
C      GTCH = 1/(1 - BTCM**2)**.5
C      KTCM = (GTCM - 1)*MTARG
C
C      WORK OUT THE CM ANGLE CORRESPONDING TO THE LAB ANGLE
C
C      T = TAN(ANGLT)
C      THETA = ACOS((1 - (GCM*T)**2)/((GCM*T)**2 + 1))
C
C      TRANSFORM TARGET ENERGY INTO THE LAB
C
C      BTX = (BTCM*COS(THETA) + BCM)/(1 + BTCM*BCM*COS(THETA))
C      BTY = BTCM*SIN(THETA)/GCM/(1 + BTCM*BCM*COS(THETA))
C      BTF = (BTX**2 + BTY**2)**.5
C      GTFF = 1/(1 - BTF**2)**.5
C      KTF = (GTFF - 1)*MTARG
C      KPF = KP - KTF
C      GPF = 1 + KPF/MPROJ
C      BPF = (1 - 1/GPF**2)**.5
C
C      CALCULATE THE NECESSARY PROJECTILE ANGLE
C
C      PINIT = (MPROJ + KP)*BP
C      PTARG = (MTARG + KTF)*BTF
C      PPROJ = (MPROJ + KPF)*BPF
C      ARG = (PINIT - PTARG*COS(ANGLT))/PPROJ
C      IF(ARG.GT.1.0) ARG = 1.0
C      IF(ARG.LT.-1.0) ARG = -1.0
C
C      ANGLP = ACOS(ARG)
C      IF(ANGLT.GT.0.0) ANGLP = -ANGLP
C
C      PZERO = PP - PTARG

```

PRFCT = PTARG  
RFLUW  
END

## APPENDIX D GLOSSARY OF TECHNICAL TERMS

|                           |   |
|---------------------------|---|
| ADC                       | Analog to Digital Converter   |
| bpi                       | bytes per inch  |
| C                         | A constant of proportionality between the change in momentum and the change in focal plane position                                     |
| CHARGEEX                  | <u>Charge Exchange</u>  |
| cm                        | centimetre  |
| $\Delta$                  | The Delta resonance (a nucleon resonance at 1232 MeV)   |
| $\Delta\Delta$            | Delta-Delta. (a state with two deltas)  |
| $\Delta E$                | Energy loss   |
| $\delta$                  | Tilt of the focal plane with respect to the VDCs  |
| $\Delta P$                | A correction to the particle momentum arising from kinematics   |
| $\Delta P_{\text{REACT}}$ | The correction of a particle momentum arising from the recoil particle  |
| $\Delta YF$               | A quantity measuring the predicted non-bend plane position of an event track crossing through the focal plane minus the actual position |
| $d(\gamma,p)n$            | An incoming gamma ray disintegrates a deuteron  |
| D                         | Angular momentum state with 2 units of angular momentum   |
| DACS                      | Data acquisition computer program   |
| DIP                       | Dipole scintillator inside the MRS dipole magnet  |
| E1                        | Electric dipole radiation   |
| E                         | Energy  |
| F                         | Focal plane offset from the first VDC   |
| FES                       | Front End Scintillator  |
| FEC                       | Front End Chamber   |

|                   |   |
|-------------------|---|
| fm                | femto metre (or fermi)  |
| FORTRAN           | FORmula TRANslation, a computer language  |
| G                 | VDC separation  |
| GeV               | Giga electron Volts   |
| $\eta$            | The asymptotic D to S state ratio of the deuteron   |
| H                 | VDC horizontal offset   |
| IA                | Impulse Approximation   |
| $\Lambda$         | Cut-off mass at the pion-nucleon vertex   |
| LD <sub>2</sub>   | Liquid D <sub>2</sub>   |
| LH <sub>2</sub>   | Liquid H <sub>2</sub>   |
| LISA              | Offline data analysis program   |
| M1                | Magnetic dipole radiation   |
| m                 | metre   |
| $\mu$ A           | micro Ampere  |
| mA                | milli Ampere  |
| mb                | milli barn  |
| mg                | milli gram  |
| $\mu$ m           | micro metre   |
| mm                | millimetre  |
| MCA               | Multi-Channel Analyser  |
| MEC               | Meson Exchange Currents   |
| MeV               | Mega electron Volts   |
| MHz               | Mega Hertz  |
| MRS               | Medium Resolution Spectrometer  |
| MRS( $\Delta p$ ) | The probability that a particle of true momentum $p$ will be measured to have a momentum $p+\Delta p$ by the MRS. |
| nA                | nano Ampere   |
| N $\Delta$        | Nucleon-Delta (a state with one nucleon and one delta)  |

|                                  |   |
|----------------------------------|---|
| <b>NFF</b>                       | <b>Nucleon Form Factor</b>  |
| <b>NN</b>                        | <b>Nucleon-Nucleon (a two nucleon state)</b>  |
| <b>NR</b>                        | <b>Non-Relativistic</b>   |
| <b>p(n,p)n</b>                   | <b>An incoming neutron elastically scatters from a proton</b>   |
| <b>p(n,d)<math>\pi^0</math></b>  | <b>An incoming neutron interacts with a proton to produce a deuteron and a neutral pion</b>                         |
| <b>p(n,d)<math>\gamma</math></b> | <b>An incoming neutron interacts with a proton to produce a deuteron and a gamma ray</b>                            |
| <b>C(n,d)X</b>                   | <b>An incoming neutron interacts with carbon to produce a deuteron (X indicates that the reaction is inclusive)</b> |
| <b>P</b>                         | <b>True momentum of a particle</b>  |
| <b>PD0-9</b>                     | <b>The 10 large scintillators at the exit of the MRS</b>  |
| <b>PFEC</b>                      | <b>MRS entrance angle projected into the non-bend plane</b>   |
| <b>PS</b>                        | <b>Pseudo-scalar</b>  |
| <b>PV</b>                        | <b>Pseudo-vector</b>  |
| <b><math>\theta_{pc}</math></b>  | <b>MRS exit angle</b>   |
| <b>QCD</b>                       | <b>Quantum Chromodynamics</b>   |
| <b>R</b>                         | <b>Reaction rate in events per unit time per unit charge</b>  |
| <b>RF</b>                        | <b>Radio-Frequency</b>  |
| <b>S</b>                         | <b>Angular momentum state with 0 units of angular momentum</b>  |
| <b>S1</b>                        | <b>A scintillator at the exit of the MRS</b>  |
| <b>S2</b>                        | <b>A scintillator at the exit of the MRS which is behind S1</b>   |
| <b>SAID</b>                      | <b>Scattering Analysis Interactive Dial-in</b>  |
| <b>SLT</b>                       | <b>Slit scintillators at the entrance of the MRS</b>  |
| <b>SPID</b>                      | <b>Spectrum for Particle Identification</b>   |
| <b>TFEC</b>                      | <b>MRS entrance angle projected into the bend plane</b>   |
| <b>TDC</b>                       | <b>Time to Digital Converter</b>  |

|               |  |
|---------------|--|
| <b>TOF</b>    | <b>Time of Flight</b>  |
| <b>TRIUMF</b> | <b>TRI-University Meson Facility</b>   |
| <b>VDC</b>    | <b>Vertical Drift Chamber</b>  |
| <b>VET</b>    | <b>The charged particle veto scintillator in front of the LH<sub>2</sub> target</b>  |
| <b>X1</b>     | <b>Position in the first VDC</b>   |
| <b>X2</b>     | <b>Position in the second VDC</b>  |
| <b>XF</b>     | <b>Raw focal plane position</b>  |
| <b>XFK</b>    | <b>Corrected focal plane position</b>  |
| <b>XI</b>     | <b>Bend plane offset of an event track at the LH<sub>2</sub> target position</b>     |
| <b>Y1</b>     | <b>Non-bend plane offset at the first VDC</b>  |
| <b>YI</b>     | <b>Non-bend plane offset of an event track at the LH<sub>2</sub> target position</b> |
| <b>YF</b>     | <b>Non-bend plane offset at the focal plane</b>                                      |
| <b>ZDPD</b>   | <b>Zero Degree Photo-Disintegration</b>  |